Alma Mater Studiorum · Università di Bologna

Scuola di Scienze

Corso di Laurea Magistrale in Fisica del Sistema Terra

A study of Air-Sea Interaction processes on Water Mass Formation and Upwelling in the Mediterranean Sea

Relatore:

Prof. Nadia Pinardi

Presentata da:

Giorgio Graffino

Sessione III

Anno Accademico 2013/2014

Abstract

Air-sea interactions are a key process in the forcing of the ocean circulation and the climate. Water Mass Formation is a phenomenon related to extreme air-sea exchanges and heavy heat losses by the water column, being capable to transfer water properties from the surface to great depth and constituting a fundamental component of the thermohaline circulation of the ocean. Wind-driven Coastal Upwelling, on the other hand, is capable to induce intense heat gain in the water column, making this phenomenon important for climate change; further, it can have a noticeable influence on many biological pelagic ecosystems mechanisms.

To study some of the fundamental characteristics of Water Mass Formation and Coastal Upwelling phenomena in the Mediterranean Sea, physical reanalysis obtained from the Mediterranean Forecating System model have been used for the period ranging from 1987 to 2012. The first chapter of this dissertation gives the basic description of the Mediterranean Sea circulation, the MFS model implementation, and the air-sea interaction physics. In the second chapter, the problem of Water Mass Formation in the Mediterranean Sea is approached, also performing *ad hoc* numerical simulations to study heat balance components. The third chapter considers the study of Mediterranean Coastal Upwelling in some particular areas (Sicily, Gulf of Lion, Aegean Sea) of the Mediterranean Basin, together with the introduction of a new Upwelling Index to characterize and predict upwelling features using only surface estimates of air-sea fluxes.

Our conclusions are that latent heat flux is the driving air-sea heat balance component in the Water Mass Formation phenomenon, while sensible heat exchanges are fundamental in Coastal Upwelling process. It is shown that our upwelling index is capable to reproduce the vertical velocity patterns in Coastal Upwelling areas. Nondimensional Marshall numbers evaluations for the open-ocean convection process in the Gulf of Lion show that it is a fully turbulent, three-dimensional phenomenon.

Sommario

Le interazioni aria-mare sono un processo chiave nella forzante della circolazione oceanica e del clima. La formazione di acqua profonda è un fenomeno legato a scambi aria-mare estremamente intensi e ad importanti perdite di calore da parte della colonna d'acqua, in grado di trasferire proprietà delle masse d'acqua dalla superficie fino a grande profondità, costituendo un fondamentale ingranaggio della circolazione termoalina degli oceani. D'altra parte, l'upwelling costiero può indurre intensi flussi di calore nell'oceano, rendendo questo fenomeno importante in relazione ai cambiamenti climatici; inoltre, esso può avere una notevole influenza su molti processi biologici degli ecosistemi costieri.

Per lo studio delle caratteristiche fondamentali della formazione di acqua profonda e dell'upwelling costiero nel Mar Mediterraneo, si sono usate le reanalisi del modello Mediterranean Forecasting System nel periodo 1987/2012. Il primo capitolo della dissertazione fornisce i concetti basilari riguardo alla circolazione del Mar Mediterraneo, all'implementazione del modello MFS, e alla fisica delle interazioni aria-mare. Nel secondo capitolo, è affrontato il problema della formazione di acqua profonda, realizzando anche simulazioni numeriche per studiare i singoli componenti del bilancio di calore. Il terzo capitolo riguarda lo studio dell'upwelling costiero in alcune aree particolari del Mar Mediterraneo (Sicilia, Golfo del Leone, Mar Egeo), insieme all'introduzione di un nuovo indice per caratterizzare e prevedere l'upwelling usando unicamente stime del flusso di calore alla superficie.

Il flusso di calore latente è il componente principale del bilancio di calore nella formazione di acqua profonda, mentre gli scambi di calore sensibile sono fondamentali nel processo di upwelling costiero. Si mostra che l'indice introdotto è in grado di riprodurre l'andamento della velocità verticale nelle aree soggette ad upwelling costiero. Le stime dei parametri adimensionali di Marshall per il processo di convezione profonda nel Golfo del Leone mostrano che il fenomeno ha una struttura tridimensionale, in cui il flusso è essenzialmente turbolento.

Acknowledgements

Recalling the time I spent to work on this dissertation, and more generally the period passed here in Bologna, a lot of people come to my mind. I am going to try, here, to remember them all.

In primis, I would like to gratefully thanks my mentor, Prof. Nadia Pinardi, for her guidance during these months, and for her encouraging enthusiasm shown to me during our meetings. Together, I sincerely thanks all the people of INGV Bologna section people for their support, both material and moral; on all, I remember Damiano, Slava, Alessandro, and Valentina.

I'd like to reserve a memory for all the people I met during these years in Bologna, including classmates, flatmates, and **Piove sul Bagnato** team, for their patience and the assistance, perhaps unconsiously, they gave me. Together these "new" friends, I remember all my oldest companions, with whom I grew up and spent most of the best times of my life, on all Giulio, Nadine, Giulia, and Vittorio.

Dulcis in fundo, I thank those without whom none of this would have been possible, that is to say my parents Giovanna and Claudio, my sister Donata, and all my relatives. This work is dedicated to them.

Contents

List of Figures

List of Tables

Chapter 1

Introduction

Upwelling processes can manifest themselves in three different expressions:

1. cyclonic eddies, where the vorticity induced by circular motion causes an uplift of isopycnals (lines of constant density) and brings interior water near the surface;

2. open-ocean Water Mass Formation events, when during the early (also called *preconditioning*) phase the combined action of a cyclonic eddy which encloses the formation area and uplifts weakly stratified water, and the atmospheric forcing which induces strong buoyancy losses, can lead to a noticeable density increase at the surface;

3. coastal upwelling, in which interior waters are "pulled" to the surface by the offshore Ekman transport induced by wind stress on the open sea.

These processes are of paramount importance, because are related to very intense exchanges between atmosphere and ocean and may affect seriously both systems dynamics. Lingering only on oceanic aspects, we can say that Water Mass Formation is an essential component of the deep oceanic flow, feeding thermohaline circulation responsible for roughly half of the poleward heat transport in the ocean (Macdonald and Wunsch 1996). Coastal Upwelling sustains uplift of nutrient-enriched subsurface waters, making upwelling ecosystems account for more then 20% of the world marine fish catch (Rykaczewski and Checkley 2008). Meanwhile, it causes a noticeable heat gain by the ocean system: for example, Wyrtki (1981) estimates an annual uptake of the order of 10^{14} W for the equatorial Pacific Ocean.
In the present work, the MFS (Mediterranean Forecasting System) Reanalysis database has been used to characterize winter Water Mass Formation and summer Coastal Upwelling in some particular areas of the Mediterranean Basin.

In general, a reanalysis database is obtained as the best estimates of ocean (or atmosphere) variables using both observation and models; this is achieved by means of a data assimilation scheme, yielding to a temporally homogeneous gridded dataset for the period of interest (Adani et al. 2011). The MFS Reanalysis period ranges from January 1st, 1987, to December 31st, 2012.
The structure of the thesis can be summarized as follows:

- Chapter 1 overviews the basic concepts about the Mediterranean Sea circulation, the physical mechanism of air-sea interactions, and the climatology of such interactions in the Mediterranean Sea; further, the main characteristics of the MFS model are given, focusing on air-sea exchange parametrizations;
- Chapter 2 focuses on Water Mass Formation processes in the Mediterranean Sea, specifically on 2004/2005 and 2005/2006 events occurring in the Gulf of Lion;
- Chapter 3 regards the Coastal Upwelling phenomenon in the Mediterranean Sea, starting from the characterization of seasonal patterns and main upwelling systems, to the definition of a new Upwelling Index;
- Chapter 4 provides the conclusions about the work, with some possible future outlooks.

The thesis objectives are:

1. understanding the air-sea fluxes in deep Water Mass Formation events,
2. understanding air-sea interaction processes for Coastal Upwelling,
3. development of a new Coastal Upwelling Index.

1.1 General Properties of the Mediterranean Sea Circulation

The Mediterranean Sea is a semi-enclosed, concentration basin, being connected to the World Ocean solely through the Gibraltar Strait, and forced by intense air-sea fluxes of momentum, heat and water typical of the open ocean. Further, it is an *anti-estuarine* basin, due to the negative heat budget (about 7 W/m^2; Castellari et al. (1998)) on an annual basis and the positive evaporation-minus-precipitation balance in the basin. The river runoff from

the basin catchment is only about 10% of the net water flux into the sea.
From long time, several particular processes are known happening in the basin, such as deep Water Mass Formation (especially in the Gulf of Lion area, and in the Adriatic and Aegean Seas) and wind-induced Coastal Upwelling (primarly on the eastern boundary coastal areas). Indeed, thanks to its properties, the Mediterranean Sea is one of the most extensively studied basin in the world.

1.1.1 General Circulation

The Mediterranean Basin is essentially formed by two large subbasin: the Western Mediterranean (WM) and the Eastern Mediterranean (EM), separated by the shallow (300 m deep) sill of Strait of Sicily. The Mediterranean circulation is governed by large-scale dynamics, despite its relatively small size (POEM Group 1992), and it is driven by three major forcings (Pinardi and Navarra 1993):

- the inflow-outflow transport at Gibraltar, that is the controlling mechanism for the water budget of the overall Mediterranean basin on decadal timescale;
- the thermal and evaporative fluxes at the air-sea interface, driving the Water Mass Formation processes and the thermohaline circulation in the basin, important from seasonal to decadal timescales;
- the wind stress, that forces the surface circulation at seasonal timescales and at spatial scales comparable with the major subbasin of the Mediterranean Sea.

The forced Mediterranean circulation results in a double gyre structure: due to the wind stress curl sign, the northern areas are characterized by cyclonic circulation, while the southern areas by anticyclonic motion. The cyclonic northern gyres are also forced by deep and intermediate water formation processes, while the southern gyres store intermediate-mode waters which compose the permanent thermocline of the basin (Pinardi et al. 2013).
The thermal and wind forcing might act on the same spatial scales, the former inducing water transformation processes and the latter causing the spreading of the newly-formed water mass (Pinardi and Navarra 1993). Using the so-called *core method*, yet Wust (1961) was able to follow the vertical spreading and mixing processes of the main water masses, thanks to intermediate maxima or minima of salinity, oxygen and temperature; he identifies four different water masses:

1. the near-surface water of Atlantic origin, between 0 and 75 m depth,

2. the intermediate water, between 200 and 600 m,

3. the deep water, between 1500 and 3000 m, and

4. the bottom water, at depths up to 4200 m.

More recently, Pinardi and Masetti (2000) paper shows that the three-dimensional circulation of the basin is mainly composed by three major meridional and zonal vertical circulation belts:

- the zonal circulation belt is shallow (0-500 m) and associated with the inflow of Atlantic Water (AW) at Gibraltar, which is transformed into Levantine Intermediate Water (LIW) in the EM; this process is thought to have a decadal timescale;

- the other cells are meridional, driven by deep Water Mass Formation processes occuring in the Northern Mediterranean areas (Gulf of Lion and Adriatic Sea, basically), with a multidecadal timescale.

There exists an interconnection among such belts; indeed, the LIW zonal overturning cell sustains the meridional cells contributing to the salt budget of the newly formed deep water in the Adriatic and Gulf of Lion areas. Further, it has been observed by Roether et al. (1996) that also the Aegean Sea provides deep waters for the EM, giving way to the Eastern Mediterranean Transient (EMT) phenomenon.
An interesting aspect underlined by Millot (1999) is that, considering the transport through the Strait of Sicily to the Western Mediterranean Basin, there is a flow partly composed by deep water formed in the Adriatic or the Aegean Sea, in addition to LIW flux (Schlitzer et al. 1991). This shows that the various water masses formed in the Mediterranean Basin do not mix completely and flow out separately. Net inflow and outflow transports through the Sicily Strait are estimated between 1-1.5 Sv (POEM Group 1992).

Surface and Intermediate-Depth Circulation

For an exhaustive description upon the Mediterranean Sea circulation, we primarly rely on Pinardi et al. (2013) paper, from which Figure 1.1 and Table 1.1 are taken.

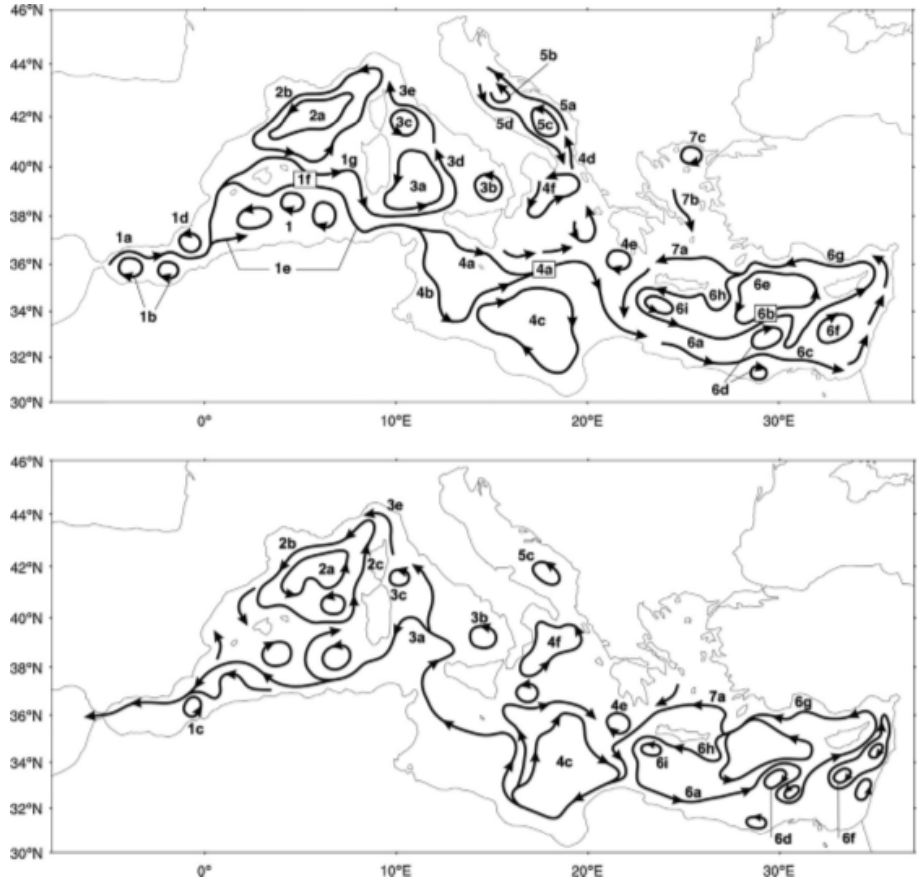

Figure 1.1: Schematic of the mean surface circulation structures (Table 1.1). Upper panel: surface circulation. Lower panel: 200-300 m circulation. Taken from Pinardi et al. (2013).

Atlantic Waters. The surface mean flow in the Mediterranean Sea is characterized by the Atlantic Water (AW) current entering from Gibraltar, interacting with mesoscale structures already present in the basin and being modified by air-sea interactions; after these processes, it has become Modified Atlantic Water (MAW). Usually, MAW forms a 100-200 m layer characterized by higher salinity respect to the inflow at Gibraltar, due to evaporation and mixing.
Mainly thanks to the Gibraltar Experiment (Kinder and Bryden 1987), it has been shown that:

- the Atlantic Water inflow in the Mediterranean Sea might be significantly smaller than previously estimated (Bryden et al. 1989),
- the exchange tends to be maximal early in the year and submaximal later (Garrett et al. 1990),
- the Mediterranean water can be uplifted from a few hundreds of meters up to the Gibraltar sill (Kinder and Bryden 1990),

Table 1.1: Nomenclature for the surface and intermediate depth circulation structures (Figure 1.1, taken from Pinardi et al. (2013).

Current Systems	Components
System 1	1a: Atlantic Water Current (AWC) 1b: Western and Eastern Alboran Gyres 1c: Almera-Oran Front 1d: Almera-Oran cyclonic eddy 1e: Algerian Current segments 1f: Western Mid-Mediterranean Current (WWMC) 1g: Southern Sardinia Current (SCC)
System 2	2a: Gulf of Lion Gyre (GLG) 2b: Liguro Provençal Current (LPCC) 2c: Western Corsica Current (WCC)
System 3	3a: South-Western Tyrrhenian Gyre (SWTG) 3b: South-Eestern Tyrrhenian Gyre (SETG) 3c: Northern Tyrrhenian Gyre (NTG) 3d: Eastern Corsica Current (ECC)
System 4	4a: Atlantic Ionian Stream (AIS) 4b: Sicily Strait Tunisian Current (SSTC) 4c: Sirte Gyre (SG) 4d: Eastern Ionian Current (EIC) 4e: Pelops Gyre (PG) 4f: Northern Ionian Cyclonic Gyre
System 5	5a: Eastern South-Adriatic Current (ESAC) 5b: Middle Adriatic Gyre 5c: South Adriatic Gyre 5d: Western Adriatic Coastal Current (WACC)
System 6	6a: Cretan Passage Southern Current (CPSC) 6b: Mid-Mediterranean Jet (MMJ) 6c: Southern Levantine Current (SLC) 6d: Mersa-Matruh Gyre System (MMSG) 6e: Rhodes Gyre (RG) 6f: Shikmona Gyre System (SGS) 6g: Asia Minor Current 6h: Ierapetra Gyre (IPG) 6i: Western Cretan Cyclonic Gyre
System 7	7a: Cretan Sea Westward Current (CSWC) 7b: Southward Cyclades Current (SWCC) 7c: North Aegean Anticyclone

- the barotropic transport is induced most by the atmospheric pressure forcing (Candela 1991).

Subsequent numerical model studies (Speich et al. 1996) and laboratory experimental works (Gleizon et al. 1996) demonstrate the coupling between the regime of the Gibraltar Strait, the general pattern of the Atlantic Flow in the Alboran Sea (Western Mediterranean), and the circulation of the underlying Mediterranean water. More, Algerian Basin works as a reservoir of MAW, thus disconnecting, at relatively short timescales, the inflow from the outflow at Gibraltar (Millot 1999).

Variability Aspects

Pinardi et al. (2013) state the Mediterranean Sea circulation time variability peaks at the seasonal and interannual time scales, as also indicated by observa-

tions (Larnicol et al. (2002); Poulain et al. (2012)) and numerical sumulations (Demirov and Pinardi (2002); Molcard et al. (2002)).

Seasonal Variability. Pinardi and Masetti (2000) underline the most fundamental aspects of the general circulation seasonal variability, which involve:

1. the Water Mass Formation cycle (Hecht et al. 1988),
2. the seasonal reversal of currents in several portions of the Mediterranean Basin (Tziperman and Malanotte-Rizzoli 1991),
3. the strenght of the mesoscale flow field (Ayoub et al. 1998),
4. the positioning of winter deep and intermediate convection sites (Artegiani et al. (1997); Lascaratos et al. (1993); Leaman and Schott (1991)).

Large-scale circulation seasonal variability is strongly influenced by the amplitude of the seasonal cycle in the external forcing: Pinardi and Masetti (2000) find that the climatological seasonal structure of the circulation and water properties can be explained by the space-time features of the meteorological forcing. Nonetheless, the contributions of the wind stress curl, the topography and the viscous effects of the boundary layer have the same order of magnitude in potential vorticity balance (Pinardi and Navarra 1993).

Interannual Variability. The wind stress variance is found to be the main driving force of the general circulation variability on the interannual timescales, which is larger in the Eastern than in the Western Mediterranean (Korres et al. 2000a). Principal aspects of interannual variability, as observed by Pinardi and Masetti (2000) over the period 1979-1993, in the Mediterranean Sea are related to:

1. the intermediate and deep Water Mass Formation rates (Nittis and Lascaratos 1998),
2. the volume transport between basins (Astraldi et al. 1995),
3. the Eastern Mediterranean Transient phenomenon (Roether et al. 1996),
4. the abrupt changes in LIW characteristics (Hecht 1992).

Various studies about the air-sea fluxes interannual variability (e.g. Castellari et al. (1998)) show that climatic variations in atmospheric forcing may drive

substantially changes in the Mediterranean general circulation, as studied also by Pinardi et al. (1997), and Korres et al. (2000b). For what concerns specifically the Water Mass Formation interannual variability, it has been observed that the vertical mass structure in the upper thermocline varies in terms of volume of water renewed every year; however, the amount of water formed each year seems not be directly related to the net heat loss at the basin scale, but determined by the horizontal and vertical structure at the initial stage of the process (Pinardi and Masetti 2000).

Mesoscale Variability. The Rossby radius of deformation is found to vary from 5 to 12 km in the whole Mediterranean basin and for the different seasons (Grilli and Pinardi 1998). It determines the scales at which energy redistribution processes occur, and locks the synoptic variability scale to 25-60 km where nonlinear dynamics is still fundamental (Pinardi and Masetti 2000). This is an important aspect, because mesoscale eddies are a basic mechanism during both formation of deep and intermediate waters and their dispersal processes (Jones and Marshall (1993); Nittis and Lascaratos (1998)).
The relationship between nonlinear and linear dynamics is synthesized in the beta Rossby number

$$\beta = \frac{\beta_0 L^2}{U}, \tag{1.1}$$

wherein L is the eddy scale, U the velocity scale, and β_0 is the latitudinal gradient of the Coriolis parameter; this nondimensional number is the ratio between the planetary and relative vorticity advection, as introduced by Pedlosky (1979). The difference between the β parameter for the Mediterranean Sea (0.2) and for the North Atlantic (2) shows that stronger nonlinear dynamics balances may be expected in the Med, driving large inverse energy cascades and inhibiting planetary wave dynamics, thus enhancing the persistency of eddies in the basin (Pinardi et al. 2013).

1.1.2 Water Mass Formation Processes

The formation of intermediate and deep water masses in the Mediterranean Sea gives rise to four overall important water masses: starting from the east, we mention the Levantine Intermediate Water (LIW), the Cretan Deep Water (CDW), the Eastern Mediterranean Deep Water (EMDW), and the Western Mediterranean Deep Water (WMDW); formation areas are indicated by numbered boxes in Figure 1.2. Pinardi et al. (2013) analyze time series from 1987

to 2007, finding that maxima Water Mass Formation rates (Sv) are always reached during February and March. More, LIW and WMDW rates are more than double respect to CDW and EMDW rates. In that period, four large events appear:

1. in 1987, forming WMDW in the Gulf of Lion area (Leaman and Kevin 1991);

2. in 1992/1993, forming LIW and Levantine Deep Water (Gertman et al. 1994), together with the CDW large formation event related to Eastern Mediterranean Transient (Roether et al. 1996);

3. in 1999/2000, occurring in the Gulf of Lion and Adriatic Sea (Manca et al. 2006);

4. in 2005/2006, occurring in the Gulf of Lion (Smith et al. 2008), as well as in the Adriatic Sea and the Rhodes Gyre area, with anomalously large formation of WMDW in an anomalously large formation area, both related to an increase of salinity on the Western Mediterranean waters and large heat loss (Herrmann et al. 2010).

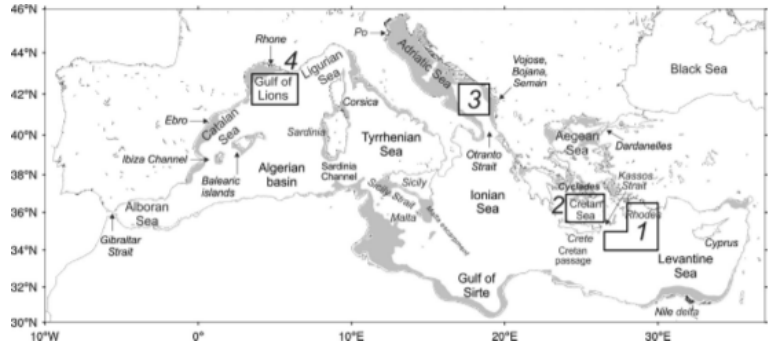

Figure 1.2: Mediterranean basin geometry and nomenclature for major seas and areas; shelf and coastal areas are shaded, less than 200-m depth; numbered boxes show deep WMF areas. Taken from Pinardi et al. (2013).

Large deep and intermediate water formation events in the Rhodes, southern Adriatic and Gulf of Lion areas occur with a frequency of three to six years, while CDW formation shows a decaying after 1996 (Pinardi et al. 2013).

Western Mediterranean Deep and Intermediate Water Formation

Both intermediate and and deep Water Mass Formation occur in the WM, depending on meteorological forcing and water column structure. Because of

the scarcity of observations in the Western Mediterranean Basin, early studies presented an oversimplified wind-driven circulation pattern (Ovchinnikov 1966). Later, WMCE (Western Mediterranean Circulation Experiment) program gave rise to a renewal interest on the area, with a field campaign started in 1985 and lasted until 1987 (La Violette 1990).

Western Intermadiate Water. Western Intermediate Water (WIW), formed on the continental shelves in both the Gulf of Lion and the Balearic Sea, is commonly found in this latter area below Modified Atlantic Water. Fuda et al. (2000) show that WIW form in early April under specific meteorological conditions. The process forming WIW seems to be similar to that occuring in the Eastern Mediterranean, where LIW forms. Further, the amount of WIW formed in the Liguro-Provençal Basin during mild winters is thought to be greater than WMDW volume (Millot 1999); anyway, either for WIW and LIW, waters of intermediate density mix easily with the sorrounding waters, so that the core may generally be identified but their limits cannot, making difficult to quantify the production rate.

Western Mediterranean Deep Water. Western Mediterranean Deep Water (WMDW) formation is observed during winter, mainly in the Gulf of Lion, and it is generally characterized by values of 12.75-12.8°C of temperature and 38.44-38.46 psu of salinity (Schott et al. 1994). The main characteristics of WMDW are continously changing at a decadal scale, but Lacombe et al. (1985) show an increase of both temperature and salinity of newly-formed deep water. A conceptual framework, emerged from the MEDOC Group (1970) study and resumed grafically in Figure 1.3, subdivides the WMDW formation process into three distinct phases:

1. a *preconditioning* phase, occurring on the large-scale (100 km), when the gyre-scale cyclonic circulation present in the Gulf of Lion area causes an evident isopycnals doming, and brings weakly stratified waters of the interior close to the surface; the transport associated with the vortex is maximum in winter and is largely driven by the wind stress curl;

2. *deep convection*, or *violent mixing* phase, triggered by the onset of Mistral and Tramontane (dry continental winds), and occurring in localized, intense plumes (small-scale cells of less than 1-km horizontal scale) during winter season, when repeated and vigorous buoyancy losses erode the near-surface stratification, thus exposing the weekly stratified water

mass beneath directly to the surface forcing (Swallow and Caston 1973), thus causing the overturning of a substantial part of the fluid column;

3. *lateral exchange*, or *sinking/spreading* phase, between the convection sites and the ambient fluid through advective processes (on a scale of a few tens of kilometers); this phase is not necessarily subsequential to the deep convection, but it is often seen to occur concurrently with the violent mixing phase (Schott and Leaman 1991).

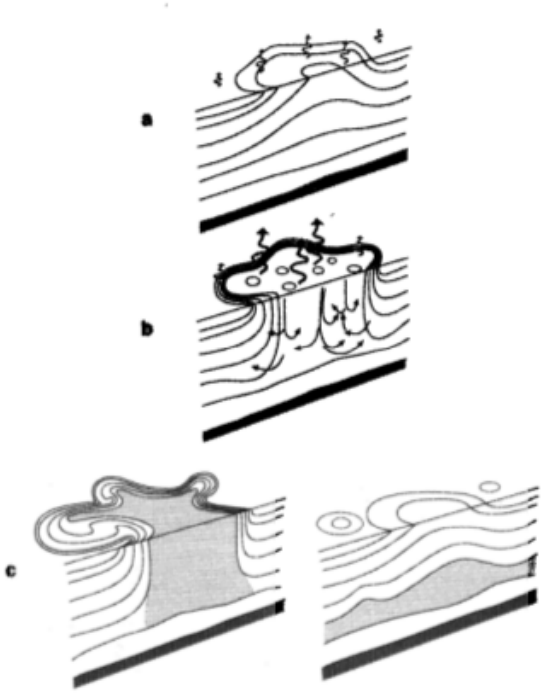

Figure 1.3: Schematic diagram of the three phases of open-ocean deep convection: (a) preconditioning, (b) deep convection, and (c) lateral spreading. Taken from Marshall and Schott (1999).

The cyclonic circulation of the region is indicated by Marshall and Schott (1999) with the $\sigma_\theta = 28.8$ kg/m^3 isopycnal doming, as also indicated by Krahmann (1997) and shown in Figure 2.6. An addictional factor that might help localize the preconditioning dome may be the generation of Taylor columns over the deep sea Rhone Fan (Hogg 1973), a topographic bulge centred at (42°N, 5°E) beginning at the 1500-m bathymetric contours and extending down to 2500-m depth (Figure 1.4).

Observational and Numerical Evidences. Convective vertical structures composing the WMF region appear to have a diameter of few hundred meters, associated with vertical speed of 10 cm/s (MEDOC Group 1970) that

develops in a convection region characterized by a mean downward motion of the order of 1 mm/s. Also Schott and Leaman (1991), from a first Acoustic Doppler Current Profiler (ADCP) experiment, find the existence of such small-scale "plumes", during an intense cooling phase in the Gulf of Lion convection area. In concert, the plumes rapidly mix properties over the preconditioning site, forming a deep mixed patch ranging in scale from several tens of kilometers to more than 100 km in diameter. During the Mediterranean Ocean Convection experiment (MEDOC Group 1970), rapid (in a day or so) mixing of the water column down to 2000 m was observed. Convection to shallower depths occasionally occurs in the elongated dome to the east of the Gulf of Lion (Figure 2.6), as reported by (Sparnocchia et al. 1995): reanalyzing the MEDOC Group (1970) data, they determine deep mixing down to 1200 m in the Ligurian Sea and, using moored observations, estimate convection depths between 500-800 m in the winter of 1991/1992. After the strong forcing typical of preconditioning phase ceases and deep convection begins, individual eddies tend to organize the convected water into vortices. The mixed fluid disperses under the influence of gravity and rotation; on a timescales of weeks and months, the disintegration of the mixed patch occurs, bringing to the reoccupation of the convection site by the advected stratified fluid from outside. In Castellari et al. (2000) study, different numerical experiments have been carried out using different atmospheric forcings (monthly (M) versus 12 hours (D)) in the period 1980-1988. As a criterion to assess WMDW formation, they use the outcropping of water layers with density range between 1029-1029.15 kg/m^3 during March: both M and D experiments are unable to simulate deep water convection in any time of winter, because the surface density is low compared to the density at deeper levels, and the convective adjustment is unable to mix down to great depth. For this reason, Castellari et al. (2000) introduce a salinity correction, in order to increase the sea surface salinity in the Gulf of Lion during preconditioning (usually in January) and violent mixing (usually in February and March) phases, accounting for the presence of LIW in the subsurface: the stratification of water columns is strongly reduced and deeper convection events occur in the area for either forcings. Using the D experiment with salinity correction, Castellari et al. (2000) estimate a WMDW average formation rate of 1.6 Sv, actually greater than other estimates (Tziperman and Speer 1994). Instead, Krahmann (1997) estimates for the NW Mediterranean Sea a deep water formation volume of $(1.8 \pm 0.6) \times 10^{13}$ m^3 yr^{-1}, corresponding to (0.6 ± 0.2) Sv; he valuates that the newly-formed deep water comprises 1.3×10^{13} m^3 of Levantine Intermediate Water and 0.5×10^{13} m^3 of Modified

Atlantic Water.

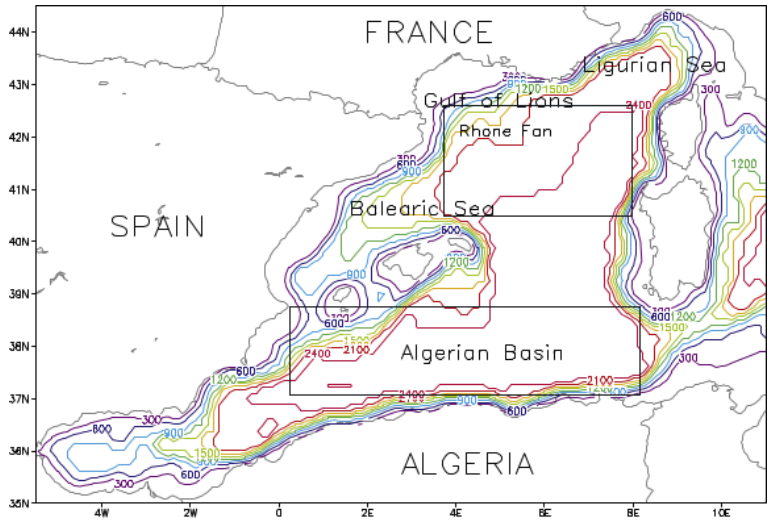

Figure 1.4: Bottom topography in the Western Mediterranean Basin. Taken from Demirov and Pinardi (2007).

Simulations from Demirov and Pinardi (2007) work, performed using a Modular Ocean Model (MOM) with horizontal resolution of $1/8° \times 1/8°$ and 31 vertical levels (Demirov and Pinardi 2002), suggest that in 1987 the violent mixing phase occurred in the Gulf of Lion already in late January, when a local intensification of the cyclonic flow is observed in the area over the Rhone Fan (Figure 1.4). The interior of the vortex is exposed to the surface cooling, producing a relatively strong uplift on the isopycnal surfaces in the upper 1000 m. Two other mesoscale eddies, which form by the instability of the cyclonic Ligurian-Provençal Current, are observed in 1987 and 1992 northeast and southeast of the Rhone Fan; contrary to the principal one, these vortex are well developed also at intermediate and deep layers. The position of the deep convection in the two cases is concomitant with the position of the main cyclonic vortex.

Eestern Mediterranean Deep and Intermediate Water Formation

The Eastern Mediterranean Sea is an open but isolated basin of interest as a laboratory basin for global ocean general circulation processes, including oceanic climate dynamical processes (POEM Group 1992). Air-sea fluxes are particularly crucial in driving the circulation of the Eastern Levantine Basin. Fresh water of Atlantic origin enters through the Strait of Sicily into the Eastern Mediterranean; as it circulates, AW becomes more saline and dense. The basin-wide deep thermohaline circulation has both an internal cell, confined to

the EM, and an external one connected with the Western Mediterranean.

Levantine Intermediate Water. During summer and autumn seasons, in the Levantine Basin a warm and salty surface layer of Levantine Surface Water (LSW) is present, which increases in density in winter due to atmospheric cooling. After that, Levantine Intermediate Water formation occurs, predominantly in March (POEM Group 1992), when this water mixes with the underlying AW and previously mixed LIW down to depth 200-400 m (Ozsoy et al. 1989). For what concerns the spatial location of LIW formation sites, there is disagreement in the literature: while Robinson et al. (1991) affirm that it should lie at the center of the Rhodes Gyre (Figure 1.1), involving a preconditioning process afforded by the domed pycnocline in the center of the vortex, Dewar (1986) indicates that WMF could occur over a much larger domain.

Eastern Mediterranean Deep Water. The Adriatic Sea is considered to be the major source of EMDW (Figure 1.2): dense water is formed in winter in the Northern Adriatic, then flowing to the Southern Adriatic where very cold and dry air storms cause deep convection, and where mixing with the incoming LIW takes place (Castellari et al. 2000); with a density of about 1029.2 kg/m^3, the newly-formed Adriatic Deep Water exits through the Strait of Otranto, reaches the bottom, and flows along the western boundary of the Ionian Basin (Artegiani et al. 1997). Roether and Schlitzer (1991) find that the water formed in the Adriatic Sea is a mixture of AW and LIW, which has been subject to surface fluxes. However, in the last decades a large climatic event known as Eastern Mediterranean Transient (EMT, Roether et al. (1996)) showed the contribution of the Aegean Sea to EMDW, with the large formation event occurred in 1992/1993 winter near the island of Crete. According to POEM Group (1992), Eastern Mediterranean Deep Water formation rate is (0.29±0.09) Sv.

1.2 Mediterranean Forecasting System

The Mediterranean Forecasting System is a hydrodynamic model supplied by the Nucleous for European Modelling of the Ocean (NEMO), with a variational data assimilation scheme (OceanVAR) for temperature and salinity vertical profiles and satellite sea level anomaly along-track data. The model uses primitive equations in spherical coordinates, and it is based on NEMO-OPA code version 3.2 (Madec and the NEMO Team 2008). The geographi-

cal coverage range from 30.187°N to 45.937°N in latitude, and from 6°W to 36.25°E in longitude; horizontal resolution is 1/16°× 1/16°, with 72 unevenly spaced vertical levels. In order to better resolve exchanges at the Gibraltar Strait, the model is nested in the Atlantic Ocean within the monthly mean climatological fields computed from 10-years daily output of the 1/4°× 1/4° MERCATOR global model (Drévillon et al. 2008). The model is forced by momentum, water and heat fluxes, computed by Bulk Formulas (Section 1.3.2) using the 6-h, 0.75° horizontal resolution ERA-Interim Reanalysis fields (Dee et al. 2011) from the European Center for Medium-Range Weather Forecast (ECMWF), using the model-predicted SST. Precipitation data are also taken from ERA-Interim database, and evaporation is derived from latent heat flux. Rivers runoff are provided by monthly mean datasets as the Climate Prediction Center Merged Analysis of Precipitation data (Xie and Arkin 1997), the Global Runoff Data Center dataset (Fekete et al. 1999), and Raicich (1996) dataset; further, the Dardanelles Strait inflow is parametrized as a river, with a climatological net inflow rates given by Kourafalou and Barbopoulos (2003). Background error correlation matrices used in the OceanVAR data assimilation scheme (Dobricic and Pinardi 2008) vary seasonally and differently for 13 regions of the Mediterranean Sea (Dobricic et al. 2006). The mean dynamic topography used in assimilation of sea level anomaly is given by Dobricic et al. (2005). Besides SLA and SST, data assimilation includes also in-situ temperature profiles from VOS-XBT (Voluntary Observing Ship - eXpendable BathyThermography), in-situ temperature and salinity profiles by ARGO floats, and in-situ temperature and salinity profiles from CTD (Conductivity-Temperature-Depth) instruments. Satellite OA-SST (Objective Analysis - Sea Surface Temperature) data are used for the correction of surface heat fluxes, with a relaxation constant of 60 W m^{-2} K^{-1}. MFS Reanalysis have been initialized with a gridded climatology for temperature and salinity, from in-situ data sampled before 1987 (SeaDataNet FP6 Project; Maillard et al. (2007)). However, model and data addimilation have been initialized at January 1st, 1985; two year of spin-up are considered, thus available data start from January 1st, 1987.

1.2.1 MFS Pilot Project

The Mediterranean Forecasting System Pilot Project (Pinardi and Flemming (1998); Pinardi et al. (2003)), started in 1998 and concluded in 2001, has brought to:

- the realization of an observation XBT system,
- NRT (Near Real Time) acquisition of physical and biological observations,
- NRT analysis and localization of SLA and SST from satellite-based observations,
- the implementation of a multivariate Reduced Order Optimal Interpolation scheme (ROOI) data assimilation system (Mey and Benkiran 2002),
- the devolopment of nested and regional models to simulate seasonal variability.

During the Pilot Project, the basin-scale forecasting model was based upon a modified version of the Modular Ocean Model (Pacanowski et al. 1990), with an horizontal grid resolution of $1/8° \times 1/8°$ and 31 vertical levels.

1.2.2 MFS Towards Environmental Prediction

The EU-MFSTEP (European Union - Mediterranean Forecasting System: Toward Environmental Prediction) project started in 2003 and lasted until 2006 (Pinardi et al. 2006). Its purpose was to further develop the operational forecasting system for the Mediterranean Sea, basing on three components: (1) an NRT observing system, (2) a numerical forecasting system at basin and regional scales, (3) a forecast product dissemination/exploitation system. The principal improvements achieved in the second stage of development of MFS operational forecast model during EU-MFSTEP are illustrated by Pinardi and Coppini (2010) and summarized in the following sections.

Free Surface Model

A new model implementation for the Mediterranean Sea, with an increased resolution of $1/16° \times 1/16°$ in the horizontal (about 6.5 km) and 72 unevenly spaced levels (from 3 m at the surface to 300 m at the sea bottom) in the vertical direction, has been developed by Tonani et al. (2008) in the framework of EU-MFSTEP, on Océan PArallélisé (OPA) code (Madec et al. 1998). The model could be defined as a "mesoscale-resolving" model for the Mediterranean Sea, since the first internal Rossby radius of deformation is around 10–15 km for most of the Mediterranean subbasin seas (with the exception of the Adriatic Sea).

The sea surface is prescribed to be an implicit free surface: this enhances the capability on simulating the sea surface height variability and the net transport at Gibraltar Strait. Moreover, this allows for using a water flux forcing in equilibrium with the salt flux; as a consequence, sea surface variability in the model shows a better resemblance with the climatological steric component than any rigid-lid models implemented until then. Horizontal viscosity is chosen to be laplacian in Gibraltar area (6.25°W - 5.125°W) and bi-laplacian elsewhere, in order to avoid unrealistic transport at the Strait; for the same reason, diffusivity in that area is 10 times larger than in the rest of the domain. The boundary conditions applied to the model at the free surface ($z = \eta$) are

$$w = \frac{D\eta}{Dt} - (E - P) \tag{1.2a}$$

$$A^{vm}\frac{\partial \mathbf{u}_h}{\partial z}\Big|_{z=\eta} = \frac{(\tau_u, \tau_v)}{\rho_0} \tag{1.2b}$$

$$A^{vT}\frac{\partial T}{\partial z}\Big|_{z=0} = \frac{Q}{\rho_0 c_p} \tag{1.2c}$$

$$\rho_0 A^{vS}\frac{\partial S}{\partial z}\Big|_{z=0} = (E - P)S\rho_0, \tag{1.2d}$$

where w is the vertical velocity, $\mathbf{u}_h$ is the horizontal surface current velocity, τ_u, τ_v are the zonal and meridional component of the wind stress (respectively), A^{vm} is the vertical eddy viscosity, A^{vT} and A^{vS} are the respective vertical diffusivity coefficients for temperature and salinity, as prescribed by Pacanowski and Philander (1981).

Nested Atlantic-Mediterranean Model

A numerical general circulation ocean model for the Mediterranean Sea, nested within an Atlantic general circulation model, has been implemented by Oddo et al. (2009). Two different configurations have been tested in a 4-year numerical experiment, in order to evaluate the effect of new lateral boundary conditions in the Atlantic Ocean on Mediterranean Sea circulation. Specifically, the first configuration uses a closed lateral boundary in a large Atlantic box; the second, instead, is nested in the same box in a general ocean circulation model (Drévillon et al. 2008). Actually, the second model configuration shows a better reproduction of the Modified Atlantic Water salinity properties, together with an improved interpretation of seasonal sea level variability. Effect on results was evinced comparing the two simulations with independent observations datasets (ARGO floats, tide gauges, satellite). Both configura-

tions have the same resolution of Tonani et al. (2008).
Two major differences in this implementation of MFS model regards water and salt fluxes: indeed, the vertical velocity is computed by a natural surface boundary condition at the surface elevation h, as

$$w\Big|_{z=h} - \left(\frac{\partial h}{\partial t} + \mathbf{u}\cdot\nabla h\right)\Big|_{z=h} = -\left(E - P - \frac{R}{A}\right), \tag{1.3}$$

wherein R indicates the rivers runoff (m s^{-1}) and A the river mouth discharge area (m^2); the complementary salt flux boundary condition is

$$A^{vS}\frac{\partial S}{\partial z}\Big|_{z=h} = S(h)\left(E - P - \frac{R}{A}\right). \tag{1.4}$$

One of the major findings deriving from the nesting approach concerns a large scale seasonal oscillation of the Mediterranean volume: the adopted lateral boundary condition allows the volume of the domain to vary according to the transport imposed by the nesting model. Furthermore, nested approach allows to accumulate energy in the model at higher frequencies.

1.3 Air-Sea Interactions

In the mid-latitude regions, mesoscale variability of the air-sea fluxes is primarly determined by the atmospheric synoptic-scale transients and their variations, as well as by inhomogeneities of SST (Taylor and WGASF Members 2000). For example, extremely high variable air-sea fluxes occur during cold or warm air outbreaks, associated with the propagation of an atmospheric cyclone over SST fronts. In turn, large-scale variability of air-sea fluxes can strongly affects development and propagation of atmospheric synoptic systems, modifying low-level static stability and contributing to local vorticity anomalies. As an example, early numerical simulations of tropical cyclones development already reveal the essential importance of latent (and perhaps sensible) heat flux from the sea surface (Ooyama 1969), as expected by Riehl (1954).

1.3.1 Air-Sea Interaction Physics

Unfortunately, continuous direct measurements of air-sea fluxes are difficult to obtain, apart from some specifical observation campaigns; thus, air-sea exchanges are determined from *Bulk Transfer Formulas*, giving the surface fluxes

between atmosphere and ocean in terms of easily measurable quantities. In general, these relations involves wind speed, air-sea moisture and temperature difference for what concerns turbulent exchanges (i.e. latent and sensible heat), or sea surface temperature and cloud cover for longwave and shortwave radiative fluxes determinations. There exists a wide range of uncertaintes upon these formulas, partially due to the inaccuracy of the input data and to faults in the parametrization of the empirical expressions (Weare 1989). Further, the use of incorrect bulk formulas can produce considerable mistakes in the output of climatic and dynamic models and can even lead to inverting the estimated direction of the net heat flux (Bignami et al. 1995).
The surface heat balance gives the net heat flux at the air-sea interface Q_T as the sum of four dominant terms

$$Q_T = Q_S + Q_B + Q_E + Q_H, \tag{1.5}$$

where Q_S is the solar radiation flux, Q_B is the longwave radiation flux, Q_E is the latent heat flux, and Q_H is the sensible heat flux. All fluxes are considered to be positive for water or ocean energy gain. In the following, we analyze separately the component of the balance, as parametrized in the MFS model.

Solar Radiation Flux

To date, physical oceanographers used various formulas, needing only inputs such as solar altitude and cloud cover, to estimate the insolation that reaches the sea surface, but the results from different formulas can vary greatly (Reed 1977). In the atmosphere, clouds and aerosols reflect and absorb some of the incoming solar radiation. In absence of clouds, Unsworth and Monteith (1972) affirm that the variability of the marine atmosphere turbidness generally lies over rather narrow limits as compared to air over land surface, which could implies that a single formula might properly computes insolation under clear skies over much of the World Ocean. Using an atmospheric transmission coefficient of 0.7, estimates of clear-sky insolation from various authors were compared by Reed (1975) with the *Smithsonian Formula* (Seckel and Beaudry 1973), where

$$Q_0 = A_0 + A_1 \cos\varphi + B_1 \sin\varphi + A_2 \cos 2\varphi + B_2 \sin 2\varphi \tag{1.6}$$

is the clear-sky mean daily insolation ($\mathrm{W/m^2}$), A_i and B_i are coefficients varying depending on latitude, and $\varphi = (t-21)(360/365)$, wherein t is the time of

year (days). Among all formulations compared in his work, only the formula from Lumb (1964) gives consistently good agreement with the Smithsonian Formula. Nonetheless, major variations in insolation are caused by clouds, which are not included in Lumb's formula. A cloud factor must be used to adjust the clear-sky insolation, as in Reed (1976) empirical relation

$$Q_S/Q_0 = 1 - 0.62C + 0.0019\beta, \tag{1.7}$$

wherein Q_S is the insolation under cloudy conditions, C is the cloud cover (tenths) and β is the noon solar altitude. The linear relation (1.7) appears to be valid from the tropics to high latitude for cloud cover from 0.3 to 1.0 (Reed 1977).

Albedo of the Sea Surface. Following Payne (1972), the albedo α is defined as the ratio of upward to downward solar irradiance just above the sea surface, i.e. $\alpha = Q_{SU}/Q_{SD}$. Sea surface albedo depends on solar elevation, sea state and cloud cover, and is generally less than 0.1 (Smith et al. 1996). Equation 1.7 does not include any information about the reflection of light by the sea surface. Thus, a more complete definition of Q_S is

$$Q_S = Q_{SD} - Q_{SU} = (1 - \alpha)Q_{SD}. \tag{1.8}$$

where Q_{SD} corresponds to the RHS of (1.7). The upward irradiance Q_{SU} above the sea surface has two components: back-scattered radiation from below the surface (emergent irradiance) and reflected radiation from the surface. Observational evidence shows that the ratio of upward to downward irradiance is about 0.005 (Payne 1971); since the albedo has a minimum value of 0.03, the upward irradiance consitutes at most about 15% of the total upward irradiance. Payne (1972), to construct his climatological albedo table of values, reads monthly downward irradiances from Budyko (1963) charts, and obtains monthly average atmospheric transmittance values. Then, he computes a monthly mean albedo value for each month and at each 10° interval of latitude and longitude from 80°N and 60°S over the Atlantic Ocean. The accuracy of his albedo values varies with latitude, because at middle/high latitude the Sun does not reach a very high altitude on the horizon. So, there can be considerable difference in the daily averaged distribution of radiance with altitude between a clear and an overcast day.

Longwave Radiation Flux

In general, the net longwave radiation is usually, but not always, upward directed; the loss is nearly all from the top few mm and is responsible (together with latent heat flux) for a "cool skin", a few top tenths or even a degree cooler than the bulk of the near-surface water (Smith et al. 1996). Owing to the lack of experimental data, most the Bulk Formulas employed to compute the net longwave flux over the ocean are developed from land-based observations (Bignami et al. 1995). However, Schiano et al. (1993) demonstrate that some observed bias are due to the weight that each parameter has in the formula. Indeed, although based on physical theories, bulk relations are empirical equations and the coefficients must be determined by fitting appropriate parameters; but, empirical coefficients of net longwave irradiance developed from land-based observations can lead to potentially large errors, when applied over the ocean. Early results from Schiano et al. (1993) and comparisons by Bignami et al. (1995) show that Bulk Formulas systematically underestimate the net longwave budget by about 30 W/m^2, primarly because these formulations are regressions derived from land or lake databases.

In-Situ Observations. The net longwave flux at sea ($IR\uparrow\downarrow$) is the difference between the upward infrared radiation flux emitted by the ocean ($IR\uparrow$) and the atmospheric radiation reaching the surface ($IR\downarrow$). In particular, the upward flux can be computed as

$$IR\uparrow = \epsilon\sigma T_S^4 + \rho IR\downarrow, \tag{1.9}$$

wherein ϵ =0.98 is the water exitance, and ρ =0.045 is the longwave reflectance; these values are taken from Mikhaylov and Zolotarev (1970). In order to make a comparison between direct measurements and bulk formula estimates, Bignami et al. (1995) use data collected concurrently with weather observations obtained during several cruises in the Western Mediterranean Sea from 1989 to 1992.

Longwave Radiation Bulk Formulas. Empirical formulas to compute the longwave radiation budget between Earth surface and atmosphere have been developed starting from the original expressions proposed by Angstrom (1929) and Brunt (1932). The general expression of most of the bulk formulas is

$$IR\uparrow\downarrow = \epsilon\sigma T^4 f(e)g(C), \tag{1.10}$$

wherein e is the water vapor pressure, C is cloud cover, and T is the air or surface temperature; the difference between the temperature of the air at the measurement level and the emitting surface can be important when the temperature jump is greater than 4°C (Berliand and Berliand 1952).
The bias variability among the bulk formulas compared by Bignami et al. (1995) does not seem to be related to seasonal or basin characteristics. Anyway, it can be notice that bulk formula estimates differ from observations by 30-50% of the net flux itself, but they seem to follow the short-period oscillations of the data. The same comparison made only for clear sky data reveals that the principal effect on the bias is due to an incorrect determination of the relationship between $IR\uparrow\downarrow$ and the surface water vapor pressure. The water vapor content in the surface atmosphere significantly varies from land to sea; so, the use of surface water vapor pressure values obtained over the sea, together with coefficients determined over land, can produce an overestimate of the atmospheric radiation.
Estimating the radiation budget as a function of the water vapor pressure, air temperature, sea surface temperature and cloud cover, Bignami et al. (1995) determine two different formulas to estimate the upwelling and downwelling components of the flux separately. Given that the upwelling longwave radiation is set by the Stefan-Boltzmann law, the chosen functional form for the downwelling longwave radiation under clear sky condition results in

$$IR\downarrow = \sigma T_a^4 (a + be^{\gamma}), \tag{1.11}$$

wherein a, b, and γ are constants to be determined; Bignami et al. (1995) state that a linear $f(e)$ is the most reasonable choice in (1.10), and their regression gives

$$a = 0.684, \quad b = 0.0056, \quad \gamma = 1.$$

A similar regression for cloud cover factor (where a quadratic relation is used for $g(C)$ in (1.10)) brings to the following expression for the downwelling longwave radiation

$$IR\downarrow = \sigma T_a^4 (0.684 + 0.0056e)(1 + 0.1762C^2). \tag{1.12}$$

Bignami et al. (1995) finally find the following radiation budget

$$IR\uparrow\downarrow = \epsilon\sigma T_S^4 - [\sigma T_a^4 (0.653 + 0.0053e)](1 + 0.1762C^2). \tag{1.13}$$

Trying to find a formulation that uses fewer parameters, they observe that a strong correlation exists between air and sea temperatures, indicating that these two parameters can be used alternatively in the functional form of either net longwave radiation or sky radiation.

Turbulent Heat and Momentum Fluxes

The rates of heat and mass transfer in the immediate neighborhood of the rough surface are controlled by the purely molecular property of the fluid; there, momentum is transferred by skin friction and form drag, resulting by the pressure force against the surface. Using Roll (1965) formalism, transfers of momentum, water vapor and sensible heat are given by the bulk aerodynamic formulas

$$\frac{\tau}{\rho} = u^{*2} = C_D u^2, \tag{1.14a}$$

$$\frac{E}{\rho} = C_E(q_s - q)u, \tag{1.14b}$$

$$\frac{H}{c\rho} = C_H(T_s - T)u, \tag{1.14c}$$

wherein τ is the wind stress, E the evaporation, H the sensible heat, c the specific heat of air, ρ the air density, and q_s the saturated specific humidity at the water-surface temperature T_s; C_D, C_E, and C_H are the bulk transfer coefficients for momentum, water vapor and sensible heat, respectively. Kondo (1975) defines the respective generalized resistances for momentum, water vapor, and heat, as

$$f = \frac{u}{u^*}, \tag{1.15a}$$

$$r_E = \frac{\rho u^*(q_s - q)}{E}, \tag{1.15b}$$

$$r_H = \frac{c\rho u^*(T_s - T)}{H}, \tag{1.15c}$$

and then expresses bulk coefficients as

$$C_D = f^{-2}, \tag{1.16a}$$

$$C_E = (r_E f)^{-1}, \tag{1.16b}$$

$$C_H = (r_H f)^{-1}. \tag{1.16c}$$

In absence of bouyancy effects (due to sensible and latent heat) on transfers and assuming logarithmic profiles of wind speed, temperature and humidity, the generalized resistances are

$$f = \frac{1}{k} \ln\left(\frac{z}{z_0}\right), \tag{1.17a}$$

$$r_E = \frac{1}{k} \ln\left(\frac{z}{z_q}\right), \tag{1.17b}$$

$$r_H = \frac{1}{k} \ln\left(\frac{z}{z_T}\right), \tag{1.17c}$$

wherein z_q and z_T are defined as the parameters to which the log profile extrapolates at the surface value, namely $q = q_s$ and $T = T_s$ (analogously to the aerodynamic roughness length z_0), and k =0.4 is the Von Karman constant. Further, two dimensionless parameters, equivalent to the sublayer Stanton number and Dalton number respectively, are defined by Kondo (1975) as

$$B_H^{-1} = r_H - f = \frac{1}{k} \ln\left(\frac{z_0}{Z_T}\right) = \frac{c\rho u^*}{H}(T_s - T_0), \tag{1.18a}$$

$$B_E^{-1} = r_E - f = \frac{1}{k} \ln\left(\frac{z_0}{Z_q}\right) = \frac{\rho u^*}{E}(q_s - q_0), \tag{1.18b}$$

to obtain

$$C_H^{-1} = f(f + B_H^{-1}), \tag{1.19a}$$

$$C_E^{-1} = f(f + B_E^{-1}). \tag{1.19b}$$

The wind stress vector $\boldsymbol{\tau}$ is calculated by Hellerman and Rosenstein (1983) using the quadratic bulk aerodynamic formulation

$$|\boldsymbol{\tau}| = \rho C_D (u^2 + v^2). \tag{1.20}$$

Drag coefficient used by Hellerman and Rosenstein (1983) have a wind speed dependence based on Bunker (1976) and a stability dependence based on Deardorff (1968). Then, C_D coefficient is a function of wind speed $(u^2+v^2)^{1/2}$ and of air-minus-sea temperature $(T_a - T_s)$, and it is approximated by the polynomial expression

$$\begin{aligned} C_D = {} & \alpha_1 + \alpha_2(u^2 + v^2)^{1/2} + \alpha_3(T_a - T_s) \\ & + \alpha_4(u^2 + v^2) + \alpha_5(T_a - T_s)^2 \\ & + \alpha_6(u^2 + v^2)^{1/2}(T_a - T_s). \end{aligned} \tag{1.21}$$

Bunker (1976) provides a table of drag coefficients as a function of wind speed and stability. To determine the drag coefficient formula equivalent to his table, six normal equations are formulated by Hellerman and Rosenstein (1983) from the tabular values of $M = (u^2 + v^2)^{1/2}$ and $\Delta T = (T_a - T_s)$, and solved by least squares for the coefficients of the best fitting second-degree polynomial; the best fit gives

$$C_D(M, \Delta T) = 0.934 \times 10^{-3} + 0.788 \times 10^{-4} M + 0.868 \times 10^{-4} \Delta T - 0.616 \times 10^{-6} M^2 - 0.120 \times 10^{-5} (\Delta T)^2 - 0.214 \times 10^{-5} M(\Delta T). \quad (1.22)$$

1.3.2 Air-Sea Fluxes in the Mediterranean Sea

Air-sea fluxes are a key element in the interpretation of many basical issues related on Mediterranean Sea general and local circulation, as well as Water Mass Formation and Coastal Upwelling processes.

The Mediterranean Heat Budget Closure Problem. There exists a *Mediterranean Heat Budget Closure Problem*, which states that the heat flux gained through the Gibraltar Strait by advection (considering the Black Sea contribution negligible) must be compensated, over a long enough period of time, by a net heat loss at the surface of the same amount, while keeping the water budget of the basin reasonable (Castellari et al. 1998). Following Bethoux (1979), the Mediterranean heat budget has an annual average of (7 $\pm$ 3) W/m^2, or (5.2 $\pm$ 1.3) W/m^2 as estimated in the more recent study of Macdonald et al. (1994). At steady-state, the advective heat flux through Gibraltar should be compensated by a net heat loss at the sea surface of the same amplitude.

MFS Model Bulk Formulas

MFS Bulk Formulas have been chosen by Castellari et al. (1998) on the basis of the Mediterranean Heat Budget Closure Problem. With the support of a numerical model based on MOM-GFDL (Pacanowski et al. 1990) and adapted for the Mediterranean Sea by Roussenov et al. (1995), they test different sets of bulk formulas estimating heat fluxes at the model surface. Relying on description made in Section 1.3.1, in the calibrated Bulk Formula set chosen by Castellari et al. (1998):

- the wind stress computation uses a drag coefficient computed according to Hellerman and Rosenstein (1983);

- the surface boundary condition for temperature involves the balance between surface solar radiation, net longwave radiation, latent, and sensible heat fluxes, wherein:

  – solar radiation at the sea surface is computed by means of Reed (1977) formula,

  – albedo monthly values come from Payne (1972) as means of the values at 40°N and 30°N for the Atlantic Ocean (about the same latitudinal band of the Mediterranean Sea),

  – the net longwave radiation flux is a function of air temperature, sea surface temperature, cloud cover, and relative humidity, as Bignami et al. (1995) state,

  – sensible and latent heat fluxes are computed by classical bulk formulas parametrized according to Kondo (1975).

The required seven input fields provided on the MFS grid model are:

- zonal and meridional components of the 10-m wind (m s^{-1}),

- total cloud cover (%),

- 2-m air temperature (K),

- 2-m dew point temperature (K),

- total precipitation (kg m^{-2} s^{-1}),

- mean sea level pressure (Pa).

The solar radiation flux is the largest term in the heat budget (1.5). Several parameters are needed for its calculation, including the total radiation reaching the ocean surface under clear sky Q_S^{TOT}, the transmissivity of the atmosphere τ, and the cloudiness C. The total radiation under clear sky is

$$\begin{aligned} Q_S^{TOT} &= Q_{DIR} + Q_{DIF} \\ &= Q_{TOA}\tau^{\sec z} + \frac{[(1-A_a)Q_{TOA} - Q_{TOA}\tau^{\sec z}]}{2}, \end{aligned} \tag{1.23}$$

wherein Q_{TOA} is the solar radiation at top of atmosphere (TOA), computed according to Rosati and Miyakoda (1988) and the *Smithsonian Meterological Tables* (List 1958) as

$$Q_{TOA} = \frac{J_0}{a^2} \cos z D_F(\phi, \lambda), \tag{1.24}$$

with J_0 being the solar constant, a the Earth radius, z the zenith angle, and D_F the fraction of daylight depending on latitude ϕ and longitude λ. More, A_a is the water vapor plus ozone absorption; Castellari et al. (1998) pose τ=0.7 and A_a=0.09. Historically, the most used bulk formulas for computing solar radiation flux are those from Lumb (1964) and Reed (1977) papers. However, Schiano et al. (1993) find that both formulas underestimate solar radiation under cloudy conditions, suggesting that they do not account for the extra downward radiation reflected by the cloud edges. Nonetheless, Castellari et al. (1998) use Reed (1977) formula

$$Q_S = Q_S^{TOT}(1 - 0.62C + 0.0019\beta)(1 - \alpha) \tag{1.25}$$

according to Rosati and Miyakoda (1988), wherein it is imposed that $Q_S = Q_S^{TOT}$ if $C < 0.3$. This relation is slightly different from (1.7), because Rosati and Miyakoda (1988) find that Equation 1.6 is valid only over limited latitudinal bands and does not account for diurnal variations. More, Equation 1.25 includes sea surface albedo, according to Payne (1972).
Regarding the net outgoing longwave radiation, Bignami et al. (1995) formula, obtained through radiation measurements in the Western Mediterranean Sea during different seasons, can be used; it is written as

$$Q_B = \epsilon\sigma T_S^4 - [\sigma T_A^4(0.653 + 0.00535 e_A)](1 + 0.1762C^2), \tag{1.26}$$

wherein e_A is the atmospheric vapor pressure, T_S is the sea surface temperature and T_A is the air temperature at the sea surface.
The sensible and latent heat fluxes are parametrized through classical bulk aerodynamical formulas as

$$Q_H = \rho_A c_p C_H |\mathbf{u}|(T_S - T_A), \tag{1.27}$$

$$Q_E = \rho_A L_E C_E |\mathbf{u}|(q_S - q_A), \tag{1.28}$$

wherein ρ_A is the density of moist air, c_p is the specific heat capacity, C_H and C_E are turbulent exchange coefficients (Kondo 1975), $\mathbf{u}$ is the wind speed, L_E is the latent heat of vaporization, q_S is the saturation specific humidity at T_S

temperature, whilst q_A is the saturation specific humidity of the air.
The net evaporation budget E can also be estimated from the terrestrial branch of the water cycle, as

$$E = P + G + R, \tag{1.29}$$

wherein P is the precipitation, G is the Gibraltar exchange, and R is the river runoff and Black Sea contribution.

1.3.3 Climatological Estimates

Castellari et al. (1998) work assesses climatological trends of (1.5) components, computed with the aforementioned Bulf Formulas set, with an atmospheric dataset composed of 12-hourly operational analyses at 1000 hPa for a 9-years period, from January 1980 to December 1988, provided from NCEP (Washington DC, USA). Such dataset was already used to force realistic simulations of the ocean circulation (Rosati and Miyakoda 1988). From the twice-daily NCEP dataset, Castellari et al. (1998) obtain that Q_T time series show a smooth signal dominated by Q_S (a strong seasonal cycle with a small interannual signal) and interannualy modulated by Q_E.
In Castellari et al. (2000) study (described in Section 1.1.2), negative anomalies of heat balance are evident in both experiments during the winters of 1981, 1987 and 1988. The climatological annual heat budgets are all negative, greater (in absolute value) in daily experiments (-10 W/m^2) than in monthly simulations (-5 W/m^2). The model climatological annual heat budgets show large standard deviations of about 6.8-8 W/m^2, being subject to a strong interannual variability. Castellari et al. (2000) estimates of the surface integrals of the water fluxes for the experiments are about 0.4 m yr^{-1} for the 1980-1988 period, which are 30% lower then observational values (0.63-0.69 m yr^{-1}) for the period 1968-1973 as calculated by Peixoto et al. (1982).

ERA-40 Surface Budgets

The Mediterranean Heat Budget Closure Problem places a valuable constraint on the long-term mean basin averaged Q_T of the Mediterranean Sea, which should be compensate for the measured net heat inflow at Gibraltar, as already mentioned. Furthermore, freshwater budget considerations constrain the evaporation and consequently the latent heat flux; Boukthir and Barnier (2000) determine a water deficit of -0.6 m/yr, while Mariotti et al. (2002) deficit estimate lies between -0.5 and -0.7 m/yr. So, according to Pettenuzzo

et al. (2010), if the multiyear averages of surface heat and water fluxes range respectively within (-6±3) W/m^2 and between -0.5 and -1.0 m/yr, they could be considered to satisfy the imposed balance.
To evaluate the surface heat balance, Pettenuzzo et al. (2010) use an approach based on the work of Large and Yeager (2009), where spatially dependent correction factors are applied to the basic atmospheric fields required as input to air-sea Bulk Formulas. Correction factors are obtained by comparison of the European Center for Medium Range Weather Forecast (ECMWF) ERA-40 Reanalysis fields (Uppala et al. 2005), with satellite observation and in-situ datasets available for the period 1985-2001. ERA-40 fields have been interpolated with a bilinear algorithm to a regular 1/16°× 1/16° resolution grid, applying a "sea-over-land" process. Nonetheless, Pettenuzzo et al. (2010) denote that the simple usage of the surface flux components, given directly by the ERA-40 dataset, yields a lower than measured estimate of the net surface heat flux; the reason of that is the underestimation of the shortwave radiation flux by about 12%, which is only partially compensated by a less negative latent heat flux.

Corrected Air-Sea Fluxes. To satisfy the heat balance required by the Closure Problem, Pettenuzzo et al. (2010) apply objective corrections on atmospheric fields of ERA-40 products, obtained from an observational data sets from various periods between 1985 and 2001: this procedure leads to solve the Heat Budget Closure Problem in the studied period and, assuming that bias reduction corrections are constant in time, they may be applied over the entire ERA-40 period (1958-2001). The computed bias reduction terms are factors (denoted by R, and used for wind, shortwave radiation and precipitation) or differences (denoted by D, and used for sea surface temperature and specific humidity); then, a linear regression between observed and ECMWF fields is performed to evaluate slope (R) and offset (D) values. Referring to Figures 7 and 8 of Pettenuzzo et al. (2010), it is shown that:

- monthly net shortwave radiation Q_S is dominated by a strong seasonal cycle with a small interannual signal, due to the cloud coverage; the same effect is also evident in the net longwave radiation Q_B time series;
- the sensible heat flux Q_H is the smallest of four terms; it becomes positive during the months of April and May and remains negative for the remaining part of the year, with strong interannual variability relative to its mean;

- the latent heat flux Q_E time series is always negative, meaning a continuous heat loss by the ocean.

As a result, the surface total heat flux Q_T time series shows a smooth signal dominated by the net shortwave radiation flux and modulated by Q_E and Q_H. MFS model has been used to check the correction method for the atmospheric fields and air-sea physical parametrizations. Preliminary results obtained by Pettenuzzo et al. (2010) during an one-year integration experiment show an improvement in the estimation of SST, and a positive result on the model temperature and salinity profiles if compared with in-situ data.
MFS Reanalysis heat flux is compared with Pettenuzzo et al. (2010) corrected fluxes in Figure 1.5 (for the entire Mediterranean Basin) and Figure 1.6 (for Western and Eastern Mediterranean, separately), in order to validate our database on a robust climatology. Table 1.2 contains averages and standard deviation for both MFS and ERA-40 heat flux for the overlap period. The overlap period between the datasets extents from January 1987 to December 2001. Trends and numerical values show that differences between datasets

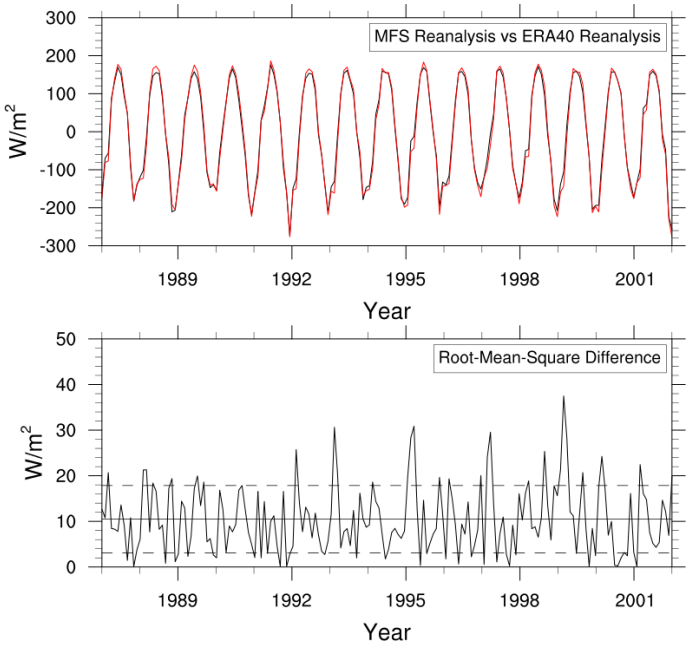

Figure 1.5: Top panel: MFS Reanalysis surface heat flux (black line) and ERA-40 corrected surface heat flux (red line) trends (Pettenuzzo et al. 2010), in the period 1987-2001. Bottom panel: Root Mean Square difference between the trends.

are larger in the Western Mediterranean Basin, where MFS presents a mean positive (downward) heat flux in contrast to the ERA-40 average. This is possibly due to the coarser resolution of ERA-40 dataset, which could miss some small-scale sea surface cold feature in the WM Basin.

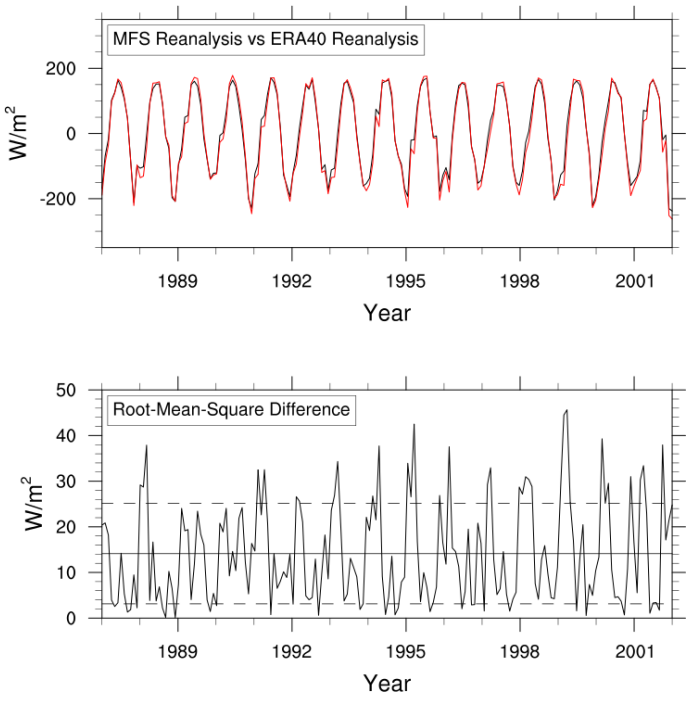

(a) West Mediterranean

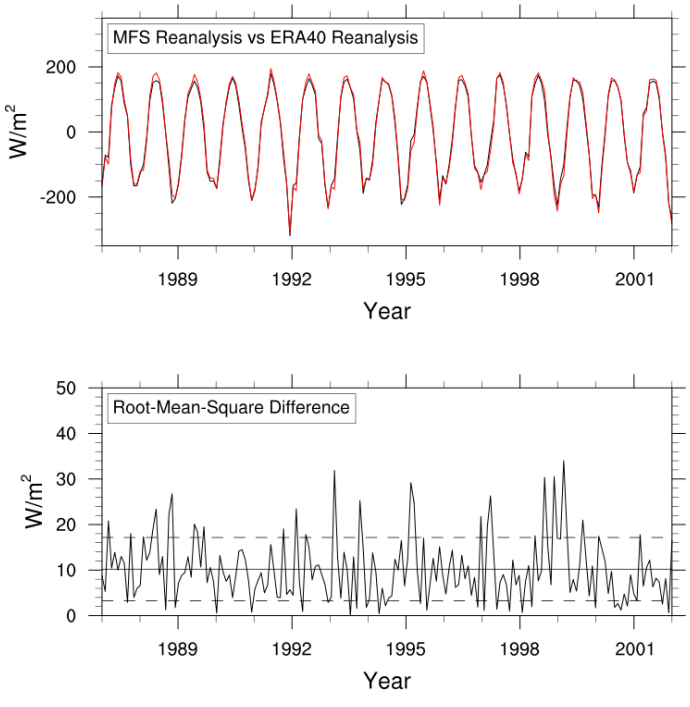

(b) East Mediterranean

Figure 1.6: Comparison between MFS Reanalysis surface heat flux (black lines) and ERA-40 corrected surface heat flux (red lines) trends (Pettenuzzo et al. 2010), separated for Western and Eastern Mediterranean basins.

Table 1.2: Averages and standard deviations (W/m^2) obtained from MFS Reanalysis and ERA-40 heat fluxes, for the period 1987-2001.

	MFS	ERA-40	RMSD
Mediterranean Basin	-2 ± 9	-4 ± 10	10 ± 7
WM Basin	4 ± 9	-4 ± 10	14 ± 11
EM Basin	-5 ± 10	-4 ± 10	10 ± 7

Chapter 2

Deep Water Mass Formation Processes

In the World Ocean, in a few special regions shown in Figure 2.1, subject to intense buoyancy losses due to the atmospheric forcing during Winter season, violent and deep-reaching convection processes can mix surface waters to great depth. Open-ocean convection occurs in the Labrador Sea (LabSea Group 1998), the Greenland Sea (GSP Group 1990), the Mediterranean Sea (MEDOC Group 1970), and occasionally in the Weddell Sea (Gordon 1982). Generally, open-ocean regions adjacent to boundaries are favored, where cold and dry winds from land or ice surface blow over water, inducing large sensible heat, latent heat and moisture fluxes; also, weakly stratified subsurface waters must be brought up by cyclonic circulation. Not only is the integral buoyancy supply important, but also its timing: an integral buoyancy loss, that may have resulted in deep convection when concentrated in a few intense Winter storms, may not yield deep mixed layers if distributed evenly over the Winter months (Marshall and Schott 1999).

2.1 Open-Ocean Convection

There are two fundamental theoretical aspects about open-ocean convection: (1) the timescales of the convective process in the ocean could be sufficiently long that it may be influenced by the Earth rotation, and (2) in the early phase vertical buoyancy transfer (by upright convection) can cause slantwise motion, due to baroclinic instability. We shall study these aspects in the following. The Rayleigh number in convective regions is many orders of magnitude larger than the critical value (Whitehead et al. 1996), and the convection is fully

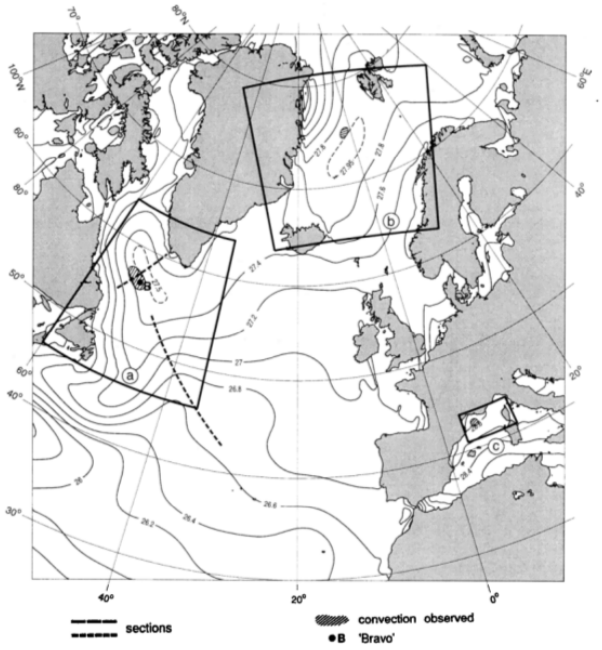

Figure 2.1: The major deep convection sites in the North Atlantic Ocean, i.e. the Labrador Sea (box a, near 'Bravo' station), the Greenland Sea (box b), and the Western Mediterranean Sea (box c); contour lines show the potential density in November at 100-m depth, as obtained from the climatological data of Levitus et al. (1994) and Levitus and Boyer (1994). Taken from Marshall and Schott (1999).

turbulent.

The buoyancy force acting on a water parcel is determined by

$$b = -g(\rho'/\rho_0), \tag{2.1}$$

where g is the gravity acceleration, $\rho' = \rho - \rho_{amb}$ is the difference in the density of the parcel relative to the surroundings, and ρ_0 is a constant reference density. Furthermore, the vertical stability of the water column is also given by the Brunt-Vaisala frequency

$$N^2 = \partial b/\partial z, \tag{2.2}$$

that is a measure of the frequency of wave disturbancies induced by stratification. In an inertial period, such disturbancies can travel for a distance given by the Rossby radius of deformation

$$L_p = NH/f, \tag{2.3}$$

where H is the layer depth and f is the Coriolis parameter. In deep convection regions, L_p sets the scale of the geostrophic eddy field (a few kilometers large); at scales greater than L_p the Earth rotation controls the dynamics and

geostrophic balance pertains, whilst at smaller scales the balanced dynamics breaks down (Marshall et al. 1997). The Buoyancy Flux $\mathbb{B}$ is expressed in terms of heat and water fluxes as

$$\mathbb{B} = \frac{g}{\rho_0}\left[\frac{\alpha_\theta}{c_w}Q_T + \rho_0\beta_S S\left(E - P - \frac{R}{/}A\right)\right], \tag{2.4}$$

where α_θ is the thermal expansion coefficient, c_w is the heat capacity of water, Q_T is the surface heat flux, β_S is the haline contraction coefficient, S is the sea surface salinity; $\mathbb{B}$ has units of m^2s^{-3}, that of a velocity times an acceleration. At the convection sites, the stratification is sufficiently weak ($N/f \approx 10$) and the buoyancy forcing is sufficiently strong ($\mathbb{B} \sim 10^{-7}m^2s^{-3}$) that convection may reach depths greater than 2000 m (Marshall and Schott 1999). It should be noted that typical vertical heat fluxes achieved by a population of convective elements (which constitutes the mixed patch, as explained in Section 1.1.2) are comparable in atmospheric and oceanic convection; however, the Buoyancy Flux are very different, because typically $\mathbb{B}_{atmos}$ is five orders of magnitude greater than $\mathbb{B}_{ocean}$.

2.1.1 The Convective Scale

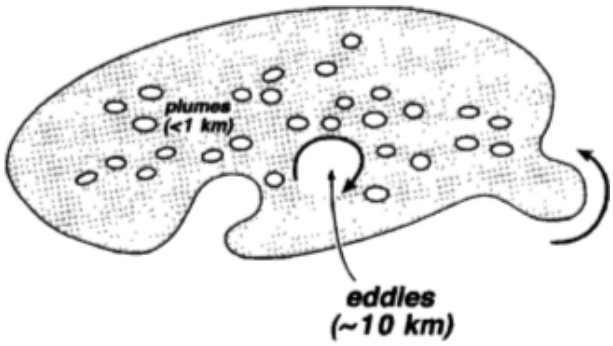

Figure 2.2: Lateral scales of the key elements involved in open-ocean deep convection process; mixed fluid is shaded, stratified fluid is unshaded. Taken from Marshall and Schott (1999).

The gross transfer properties of the convecting plumes depend on the large-scale dynamics, drawing buoyancy from depth at a rate sufficient to compensate the loss caused by the surface forcing; a comparison of lateral scales of key elements involved in deep convection process is show in Figure 2.2.

Upright Convection

Let us consider a resting stratified ocean (with $N = N_{th}$, where th stands for "thermocline"), subject to uniform and widespread buoyancy loss: on the large scale the flow must fulfill geostrophic balance and is therefore almost horizontally nondivergent, so the fluid cannot simultaneously overturn on these scales; rather, the response to a widespread cooling is such that relatively small convection cells develop. Unlike the classical convection problem (Howard 1964), in the open ocean the "thermal layer" (where water parcels are in direct contact with the atmosphere) is not the rate-controlling one; we have already described such "cool skin" in Section 1.3.1. Jones and Marshall (1993) argue that its

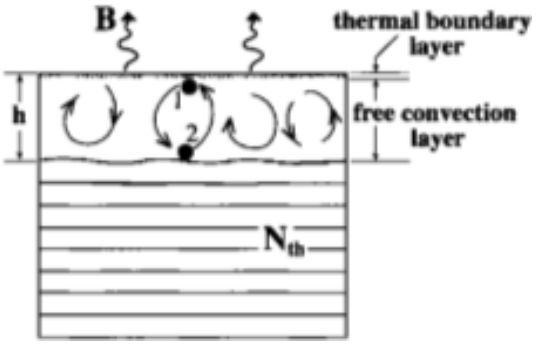

Figure 2.3: A schematic diagram showing the the convective deepening of a mixed layer. Taken from Marshall and Schott (1999).

depth δ, measured against the free convective layer depth h (Figure 2.3), is given by

$$\delta/h = 1/Pe^{1/2} \tag{2.5}$$

where $Pe = HW/k$ is the thermal Peclet Number (H is the convective length scale, W is the vertical velocity scale, and k is the thermal diffusivity); it is a measure of the efficiency of buoyancy transfer on the plume scale relative to turbulent processes in the thermal boundary layer. Peclet Number can be very large in deep open-ocean convection sites ($\sim$1000, Tables 2.1 and 2.2), meaning that the boundary layer is shallow when compared to the vertical scale of the convective plumes.

Scaling Laws and Nondimensional Numbers

Let us pose that a sustained surface Buoyancy Flux of magnitude $\mathbb{B}_0$ drives convection in a homogeneous fluid of depth h: a buoyancy-driven turbulence layer deepens as the plumes evolve in time, penetrating into the fluid below and extending down, at the end, to the depth h. For times $t \ll f^{-1}$, rotation is

not important and only $\mathbb{B}_0$ remains as the controlling parameter. Then, Jones and Marshall (1993) scales can be formed from $\mathbb{B}_0$ and t, that is:

$$l \sim (\mathbb{B}_0 t^3)^{1/2} \tag{2.6a}$$

$$u \sim w \sim (\mathbb{B}_0 t)^{1/2} \tag{2.6b}$$

$$b \sim (\mathbb{B}_0 / t)^{1/2} \tag{2.6c}$$

where l is the scale of the convective elements. Further, according to Deardorff (1985), it can be assumed that the depth h limits the vertical scale of convection, and a scaling independent of rotation can be drawn as

$$l \sim l_{norot} = h \tag{2.7a}$$

$$u \sim u_{norot} = (\mathbb{B}_0 h)^{1/3} \tag{2.7b}$$

$$b \sim b_{norot} = (\mathbb{B}_0^2 / h)^{1/3}. \tag{2.7c}$$

However, if h is large enough, the evolving convection comes under geostrophic balance; so, replacing t with f^{-1} we can obtain a scaling constrained by Earth rotation (Fernando et al. 1991):

$$l \sim l_{rot} = (\mathbb{B}_0 / f^3)^{1/2} \tag{2.8a}$$

$$u \sim u_{rot} = (\mathbb{B}_0 / f)^{1/2} \tag{2.8b}$$

$$b \sim b_{rot} = (\mathbb{B}_0 f)^{1/2} \tag{2.8c}$$

As the plume sinks, it becomes subject to entrainment from the surrounding waters, leading to an expansion in its lateral scale as it goes down; however, if the convective layer is deep enough, the entraining plume attains a lateral scale at which it becomes affected by rotation before it reaches the bottom of the layer. The inibition of lateral growth in the presence of rotation is a consequence of the existence of Taylor columns (Jacobs 1964), which impart rigidity to the fluid column. The previous considerations suggest that, if l_{rot}/h is small, one might expect to see an upper convective layer beneath which plumes, under rotational control, extend down to the bottom (Figure 2.4): the *natural Rossby Number*

$$Ro^* = \frac{l_{rot}}{h} = \left(\frac{\mathbb{B}_0}{f^3 h^2} \right)^{1/2} \tag{2.9}$$

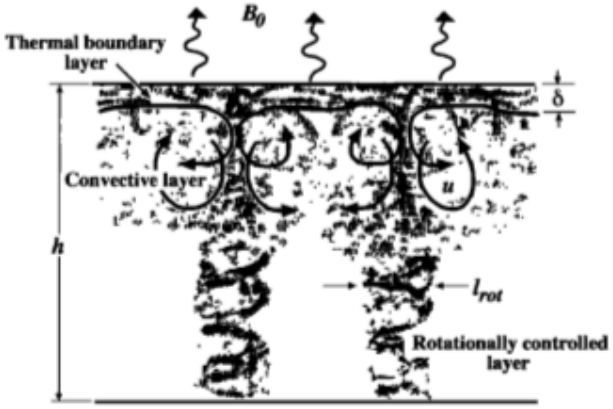

Figure 2.4: Evolution of a population of convective plumes under rotational control. Taken from Marshall and Schott (1999).

allows to study this aspect, comparing the l_{rot} length, at which sinking motion is affected by Earth rotation, with the estimated convective layer depth. Following Boubnov and Golitsyn (1990) and Fernando et al. (1991), two other nondimensional numbers can be introduced to characterize convection on a rotating system: the f-independent *flux Rayleigh Number*

$$Ra_f = \frac{\mathbb{B}_0 h^4}{\kappa^2 \nu}, \tag{2.10}$$

where ν and κ are respectively the eddy viscosity and the thermal diffusivity, and the *Taylor Number*

$$Ta = \frac{1}{Ek^2} = \left(\frac{fh^2}{\nu}\right)^2, \tag{2.11}$$

where Ek is the *vertical Ekman Number*, which determines the importance of frictional terms on the convective motion (Vallis 2006).

Numerical and Observational Evidences. Laboratory studies of rotating convection, using horizontally homogeneous sources, show that scaling equations (2.7) and (2.8) are appropriate for the non-rotating and rotating (low Ro^*) cases (Fernando et al. 1991). Marshall and Schott (1999) affirm that the consensus of the laboratory experimentalists is that rotational effects are felt only when $Ro^* < 0.1$, rather than $Ro^* < 0.7$ obtained in the numerical experiments of Jones and Marshall (1993). The approach of Jones and Marshall (1993) is that of Large Eddy Simulation (LES), wherein turbulence is isotropic and homogeneous; however, rotating convection is heavily anisotropic, primarly because the plumes are strongly stiffened by rotation. Laboratory ex-

periments on isolated mixed patches in unstratified fluids (Maxworthy 1997) suggest that u_{rot} and l_{rot} may not be entirely appropriate in the case of cooling over an extended but finite patch, because of the strong horizontal exchange of fluid between the convection region and the ambient fluid, imposing the size of the patch r as an additional variable (Coates and Ivey 1997).

2.1.2 Dynamics of the Mixed Patches

The defining feature of homogeneous patches is that properties (such as T and S) are mixed by convection, leading to a local diminution of property gradients interior to the patch, but stronger gradients around the periphery (Marshall and Schott 1999). The degree of the horizontal homogeneity of the convection patch can be very variable, due to vertical and horizontal temperature and salinity inhomogeneities. This aspect can be evaluated from observations: for example, during the 1987 Water Mass Formation event in the Gulf of Lion the homogeneity was nearly complete (Leaman and Schott 1991), whilst in the same area during the 1992 WMF event there were significant inhomogeneities in the deep convection patches (Schott et al. 1996). The development of the mixed layer depth in the Gulf of Lion was successfully observed by Schott et al. (1996) during Winter 1991/1992 using CTD casts, moored stations, air-sea flux and stratification measurements. They find steps in the temperature and salinity profiles at the bottom of deep mixed patches, apparently compensated in density profiles; thus, they suggest that deep mixing by convective plumes is, on first approximation, non penetrative. Comparing observations of mixed-layer deepening over a convective season with the evolution of the layer as predicted by a simple 1-D model (Rahmstorf 1991) and assuming static erosion of the stratification due to surface buoyancy loss alone, Marshall and Schott (1999) show departures occurring when the mixed layer is shallow and wind mixing is important. So, they states that simple mixed layer models can be successfully used to represent the evolving mixed layer and interior mixed patch properties on short timescales; however, lateral advection plays an increasingly important role as time progresses, and can dominate over seasonal and interannual timescales.

Baroclinic Instability

Large horizontal buoyancy gradients on the edge of the convection patch support strong horizontal currents in a thermal wind balance, leading to the "rim current". Then, on a large-scale rotating fluid, a thermal wind relation can be

stated: assuming a lateral inhonomogeneity (such as a lateral shear, a density front, or a pre-existing eddy) along the x-direction, a thermal-wind current $u(y, z)$ must develops from the relation

$$fu_z = -b_y. \tag{2.12}$$

Thus, in the presence of rotational and angular momentum constraints, such as

$$m = u - fy, \tag{2.13}$$

if u is constant then m isolines are vertical, and the fluid is stiffened parallel to the rotation vector: so, if m is conserved following fluid elements, they must acquire a speed $u = f\delta y$ on moving a distance δy, or u_{rot} on moving a distance l_{rot}. As a consequence, the m-surfaces are pressed together at the top (inducing cyclonic vorticity) and pushed out below (generating anticyclonic vorticity). Instead, if u is not constant, Equation 2.13 states that m-surfaces are tilted over, because $\partial u/\partial z \neq 0$, and they induce fluid particles to move along slanting paths (Figure 2.5), rather than vertical (Figure 2.3). So, the stability of the

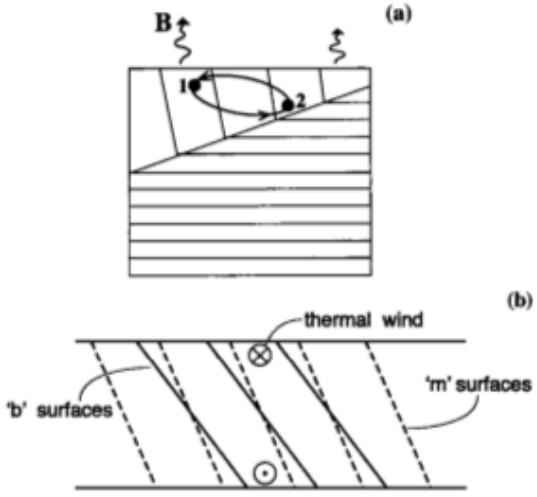

Figure 2.5: (a) Lateral gradients in mixed-layer depth induced by spatial density inhomogenities. (b) Angular momentum (m) and buoyancy (b) surfaces in the presence of a thermal wind shear. Taken from Marshall and Schott (1999).

layer must depend on the sign of Δb measured along the m-surface, or the sign of the absolute vorticity normal to the b-surface. This more general instability is called *slantwise convection* by Emanuel (1994), where the stability depends on the sign of the potential vorticity

$$Q = \frac{1}{g}(\mathbf{q} \cdot \nabla b), \tag{2.14}$$

where $\mathbf{q} = 2\boldsymbol{\Omega} + \nabla \times \mathbf{u}$ is the absolute vorticity vector. Indeed, if $Q < 0$ the flow is convectively unstable to the simmetrical instability: slantwise convection might then be expected to set on, to return the Q of the layer to zero. For the particular case of open-ocean convection in the NorthWestern Mediterranean Sea, Legg and McWilliams (2001) find that homogenization of the water column during the violent mixing phase in the Gulf of Lion, which diminishes the Rossby radius of deformation, favors baroclinic instability of the flow; thus, the flow during the first weeks after the deep convection phase is dominated by relatively small eddies, which tend to merge and enlarge (Demirov and Pinardi 2007).

Invertibility Principle. Simple angular momentum constraints suggest that if rotation is felt on the convective scale, radial inflow at upper levels spins up cyclonic vorticity, while radial outflow below sets up anticyclonic vorticity (Davey and Whitehead 1981). Further, it is possible to consider the convective process and the subsequent evolution of the mixed patch from the perspective of the potential vorticity Q, invoking the invertibility principle (Hoskins et al. 1985): if the large-scale flow is in geostrophic and hydrostatic balance, Q can be expressed (entering the geostrophic and hydrostatic relations in to (2.14)) in terms of the pressure fields through an elliptic operator. So, a dense (cold and/or salty) water mass at the surface induces cyclonic circulation, because it is equivalent to a positive sheet of PV; instead, since the convection causes lowering of PV in the interior of the convective system, anticyclonic circulation is established at the bottom of the convective layer. The homogeneous water column at the surface is colder and denser relative to the surroundings, so ∇Q points inward to the positive PV sheet; instead, the interior of the mixed patch has very low (essentially zero) PV, and ∇Q points outward from the patch. However, air-sea interactions may alter the vertical velocity structure in a cyclonic vortex, inducing a secondary circulation wherein eddy surface velocity is decreased while deeper flow is increased (Williams 1988); nonetheless, at the level of the quasi-geostrophic approximation, there is no change in the depth-integrated circulation.

2.1.3 Properties of Convective Plumes

Figure 2.6 shows different convective regimes from three Water Mass Formation events, occurred in 1969, 1987, and 1992; for each event, a dedicated study was realized. During MEDOC Group (1970) experiment, the first one

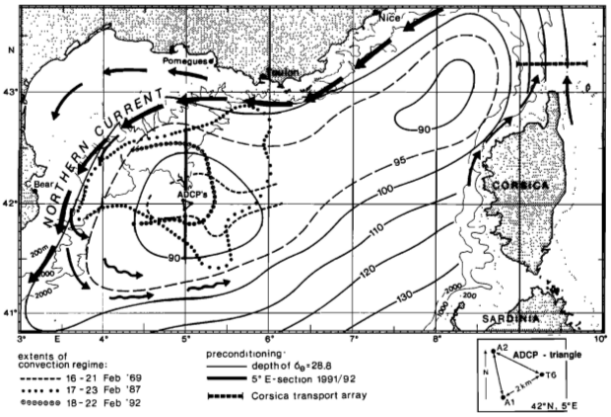

Figure 2.6: Circulation and convective conditions of the NorthWestern Mediterranean; isolines show depths of 1028.8 kg/m^3 isopycnal surface; extents of observed mixed patches are shown for 1969 (dashed line), 1987 (large dots), and 1992 (circled small dots). Taken from Marshall and Schott (1999).

with direct measurements, downward velocities of 12 cm/s were observed by a rotating float (Voorhis and Webb 1970); nevertheless, the convective elements scale could not be determinated. The first experiment using moored ADCP (Acoustic Doppler Current Profiler) was carried out in early 1987 in the Gulf of Lion, associated with a Mistral event (Leaman and Schott (1991); Schott and Leaman (1991)): observed heat fluxes reached 500 W/m^2 and caused vertical motions up to 13 cm/s with duration of only 1-2 hours; the order of magnitude of the plumes horizontal scale was estimated to be 1 km. In a subsequent experiment, a 2-km side ADCP instruments array was employed in the Gulf of Lion during 1991/1992 Winter: using the beam spreading of the ADCPs, the increase of decorrelation with increasing transducer distance allows to estimate the horizontal plume scales in the range 500-800 m (Marshall and Schott 1999). Small convective cells was detected at the 300-m level about 4 hours after the cooling began to be effective, with an observed decay timescale of 6 hours, suggesting that the plumes decay before they become subject to Earth rotation.

Vertical Mass Transport. On the large scale, stretching/compression of Taylor columns generates horizontal circulation due to vorticity conservation: this enables to relate the vertical velocity in the convective area to the time rate of change of the circulation around the mixed patch, that is

$$\frac{\partial}{\partial t} \oint \mathbf{u} \cdot d\mathbf{l} = f \frac{\partial \overline{w}_{area}}{\partial z}, \tag{2.15}$$

where $\overline{w}_{area}$ is the vertical velocity averaged over the patch. Schott et al. (1996) observations in the Gulf of Lion suggest that small-term (few days) changes in horizontal circulation around a convective patch do not exceed 20-30 cm s^{-1}; from Equation 2.15, the subsequent vertical velocity is less than 0.1 mm s^{-1}, much smaller with those associated with individual plumes. So, the plume scale does not play a significant role in vertical mass transport, even though they are very efficient mixers of properties (Send and Marshall 1995); this implies that the water mass formation rate cannot be computed directly from any measurement or computation of w, but instead through volumes of homogenized fluid generated in the mixing phase, as we do in Section 2.2.

2.2 Analysis of Western Mediterranean Deep Water Formation Events

In this section, we show some basical properties of the Water Mass Formation processes in the Gulf of Lion area (Western Mediterranean Basin) using MFS Reanalysis data. The geographical extent ranges from 0°E to 10°E in longitude and from 38°N to 44°N in latitude.

Water Mass Formation Rate. The Lascaratos et al. (1993) method is used to compute WMF rate, as in Pinardi et al. (2013): for each day it is computed the volume of waters on a specified density interval (in our case 1029-1029.1 kg m^{-3}, as indicated by Castellari et al. (2000)), and then it is divided by one day in seconds; a description of MFS model in-situ density function is given in Appendix A. The computation is done only in the mixed layer, which depth is obtained using the density difference (0.1 kg m^{-3}, in our case) from the subsurface value. Then, monthly and seasonal values are obtained by summing daily values and dividing by the time interval.
In Figure 2.7, monthly trend is characterized by single peaks, corresponding to Winter WMF events which happen in almost every year in the MFS Reanalysis period: the major events occurred in 1987 (Leaman and Schott 1991), in 1999 (Bethoux et al. 2002), in 2005-2006 (Smith et al. 2008), and in 2010; this latter event, nevertheless its dimension, has not been studied yet so intensively in the literature. As we can see from the green line on the left panel and from the histogram on the right panel, the February-March contribution is the main one in every WMF event, with other months (e.g. January) giving a perceptible contribution only in 2006 event (not shown). The WMF event

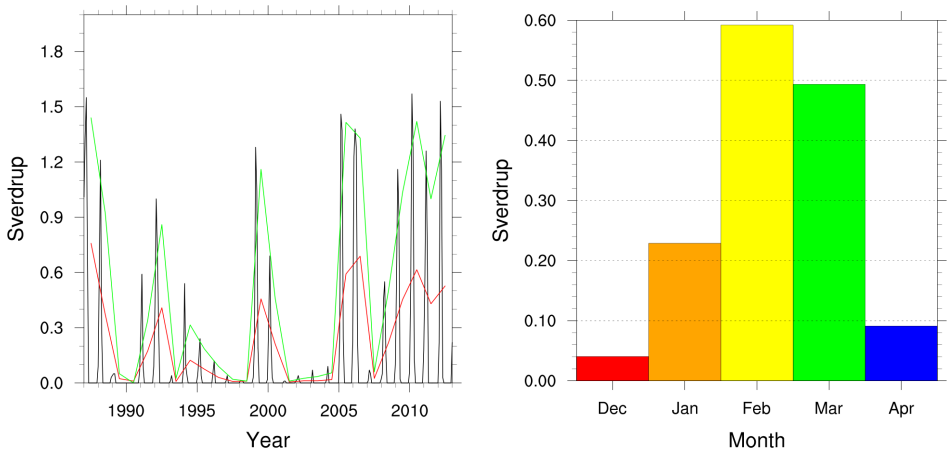

(a) WMF Trends (b) Average Monthly Contributions

Figure 2.7: Water Mass Formation rate (Sv) in the Gulf of Lion area in the MFS Reanalysis period (1987-2012): the black line corresponds to the monthly WMF value, the green line to the February-March contribution, and the red line to the seasonal contribution.

described in our work is the 2005-2006 one, which more precisely is composed by two distinct episodes, characterized by different formation area extents and atmospheric forcings, although the newly-formed water volume is comparable. Thus, in the following we shall expose the main characteristics about this two-fold WMF event separately, lingering on atmospheric forcing, horizontal and vertical density structure, and then comparing MFS Reanalysis results with ARGO float observations. It must be stressed that ARGO floats rarely profile the same water column more than once, and may drift more than 30 km between subsequent profiles; however, given that deep convection processes act over fairly large regions, Smith et al. (2008) prescribe that the features observed in one region are similar to those in adjacent locations within the same subbasin, as we shall see in Section 2.4. Finally, Marshall Numbers, introduced in Section 2.1.1, are estimated for both events.

2.2.1 2004/2005 Winter Water Mass Formation Event

Atmospheric Forcing. We can see from the Figure 2.8 the downward heat flux (W m^{-2}, red line), compared with the upward water flux (blue line, please note the reversed y-axis) expressed as a rate (mm day^{-1}); these trends are computed as daily values in the point of minimum heat flux located in 41.3°N-4.1°E, not far from the well-known MEDOC area (42°N-5°E; MEDOC Group (1970)). The correlation between trends seems good (equal to 0.66), confirming that the latent heat flux, resulting from water exchanges, is the main component of the surface heat balance (as we shall see in Section 2.3). The

minimum heat flux value, equal to -1039 W m^{-2} at the minimum point, is reached November 13th, 2004, showing that substantial surface heat loss can precede the "usual" open-ocean convection preconditioning phase by even two months. Nevertheless, this massive heat transfer cannot lead to a deep WMF, being just an isolated peak; rather, repeated and continuous losses in the following months (between December and March) give the suitable conditions to deep WMF occurs. The total heat loss in the minimum point for the period between November 1st, 2004, to April 30th, 2005, is 30.9 kW m^{-2}.

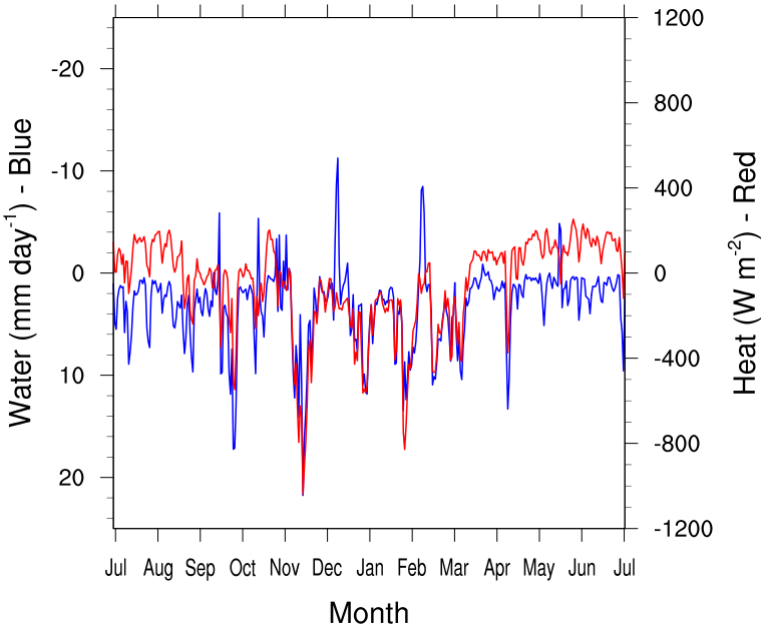

Figure 2.8: Heat (W/m^2, red line) and water (mm/day, blue line) fluxes trends during the 2004/2005 Winter season, computed at the heat flux minimum point in the Gulf of Lion area.

Density Structure. Convection does not appear to be a strongly localized phenomenon, but rather to be spread within an extended area, comprised between the Balearic subbasin and the Ligurian Sea, dependly on the strength and the extension of the forcing. Figure 2.9 shows the 8-m depth in-situ density map of the Gulf of Lion area for six days during the 2004/2005 Winter season, using the density range defined by Castellari et al. (2000): only in February and March the stratification is eroded enough by atmospheric forcing to permit convection to occurs, while in April re-stratification has already operated to recover the normal situation.

This point-of-view seems to be confirmed by the longitudinal/latitudinal slices shown in Figure 2.10 and Figure 2.11, along the black lines in Figure 2.9: although January slices (and also the previous-months ones, not shown) does

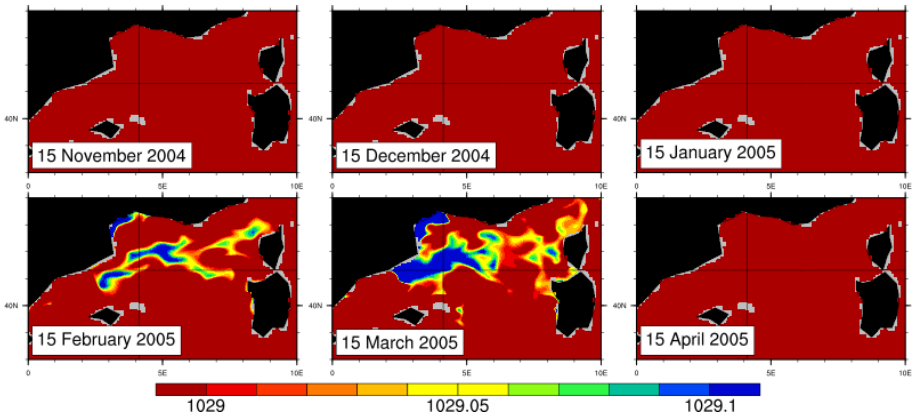

Figure 2.9: In-situ density (kg/m^3) at 8-m depth on the Gulf of Lion area during the 2004/2005 WMF event; black lines show slice locations (Figure 2.10 and Figure 2.11).

not exhibit an outcropping of 1029 kg m^{-3}, finally in February and March the stratification has been eroded and the water column is well mixed on its entire depth. In our opinion, what we see here does not contrast with Marshall and Schott (1999) approach (Section 2.1), being a whole sight of the concert action of many single convective plumes; furthermore, the use of daily values does not allow to resolve phenomena occurring on hourly timescales, such as convective plumes.

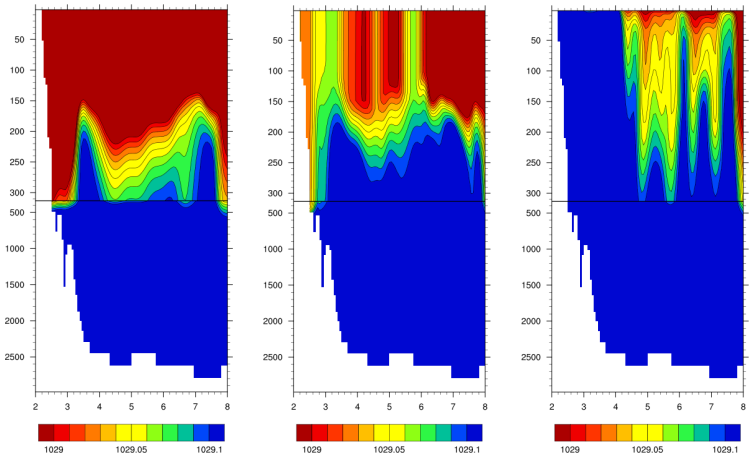

(a) 15 January (b) 15 February (c) 15 March

Figure 2.10: Longitudinal slice of in-situ density (kg/m^3) during the 2004/2005 WMF event, in the location shown in Figure 2.9.

ARGO Observations. ARGO profiler 6900279 was floating in Balearic sub-basin during 2004/2005 WMF event, near Maiorca island. Temperature and salinity profiles obtained from MFS Reanalysis and ARGO float 6900279 are thus compared in Figure 2.12. Major differences come from the upper layer,

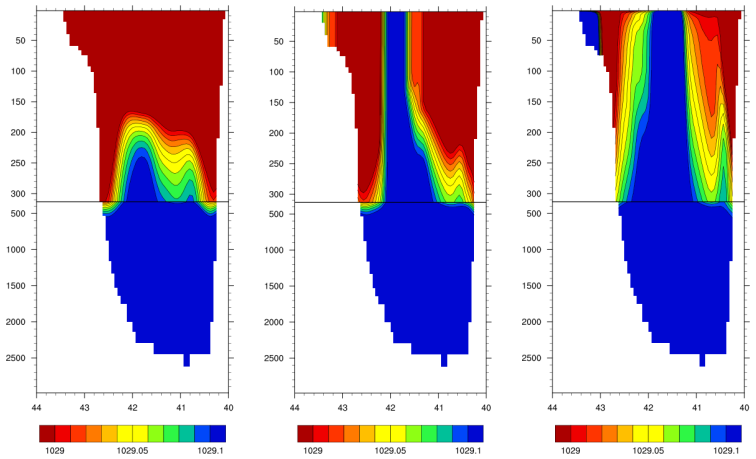

(a) 15 January (b) 15 February (c) 15 March

Figure 2.11: Latitudinal slice of in-situ density (kg/m^3) during the 2004/2005 WMF event, in the location shown in Figure 2.9.

where MFS profiles exhibit some little fluctuations around ARGO values (primarly in January), while at the thermocline/alocline depth and downward the agreement is good.

Marshall Numbers. Table 2.1 shows Marshall Numbers values computed on a monthly average in the heat flux minimum point, for the 2004/2005 case. Buoyancy Flux is consistent with what expected by Marshall and Schott (1999) for a buoyancy loss giving way to deep convection. Computed thermal Peclet Number values seem too high during 2004/2005 Winter, approaching reference value only in December and January; this might mean that the thermal layer (the region of the water column directly under the atmospheric influence) increases its depth respect to the convective layer, due to a strong external forcing. Likewise, the natural Rossby Number is always one order of magnitude larger than the reference given by Marshall and Schott (1999); being Ro^* descripted by Equation 2.9, we can say that the convective layer depth is quite smaller than the l_{rot} scale, so the sinking plumes do not feel a noticeable influence from Earth rotation. The computed flux Rayleigh Number is two-three orders of magnitude higher than the reference value given by Jones and Marshall (1993), but it is included in the range 10^4-10^{13} of Klinger and Marshall (1995) numerical work. Evaluated Taylor Number is in the expected range of values given by Jones and Marshall (1993), and the same applies to the vertical Ekman Number.
According to Boubnov and Golitsyn (1990) approach, scatterplot of Ra_f and Ta values is shown in Figure 2.18; since for open-ocean deep convection appro-

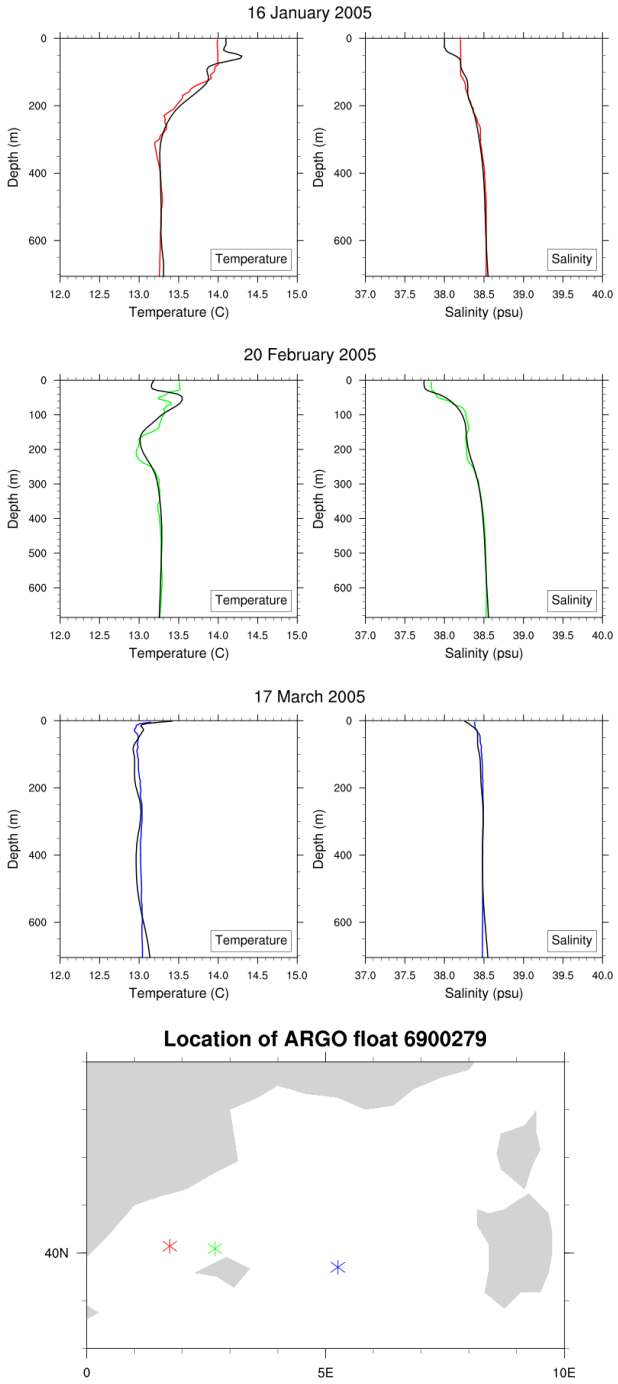

Figure 2.12: Comparison between MFS Reanalysis potential temperature (°C) and salinity (psu) profiles (black lines), with ARGO float 6900279 measurements (coloured lines) in the Balearic area during the 2004/2005 WMF event.

priate values for these parameters are not known without any certainty, Klinger and Marshall (1995) propose to characterize the process in terms of Ra_f and Ro^*, as we do in Figure 2.19. Both graphs suggest that the 2004/2005 Water Mass Formation event is characterized by a fully turbulent, three-dimensional dynamics, as we expected from theoretical speculations (Section 2.1).

2.2.2 2005/2006 Winter Water Mass Formation Event

To examine the 2005/2006 WMF event characteristics, the same approach of the 2004/2005 could be used. Nonetheless, we will show that there are some differences: the formation area seems more extensive, and the atmospheric forcing is somewhat "smoother" than in the previous event. Indeed, we prefer to examine surface fluxes on the minimum point of monthly averaged heat flux, instead of considering the daily minimum as in the previous case; in fact, the daily minimum for this event is located near the Corsica island, in our opinion too distant from the usual formation area.

Atmospheric Forcing. The monthly heat flux minimum is located at 41.7°N-4.4°E, in the Gulf of Lion. Heat (W m^{-2}) and water (mm day^{-1}) daily fluxes in this point are shown in Figure 2.13: actually, the preconditioning phase for this events is already observed in December 2005, with at least three heat loss episodes reaching 600-700 W m^{-2} in two months, from mid November to mid January. The minimum value reached in this period is -700 W m^2 at December 28th, 2005. The total heat loss in the minimum point for the period between November 1st, 2005, to April 30th, 2006, is 27.0 kW m^{-2}.

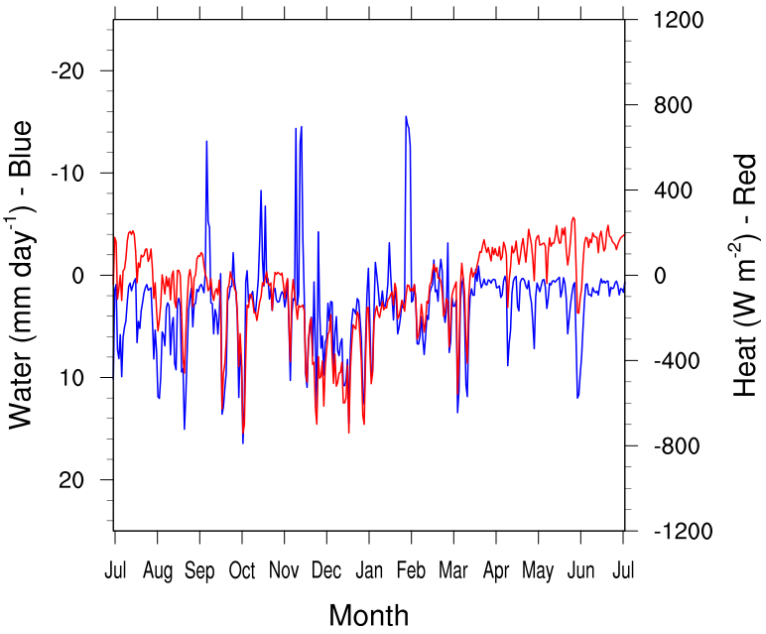

Figure 2.13: Heat (W/m^2, red line) and water (mm/day, blue line) fluxes trends during the 2005/2006 Winter season, computed at the mean heat flux minimum point in the Gulf of Lion area.

Density Structure. The 8-m depth density map displays the near-surface outcropping of 1029 kg m^{-3} isoline yet in January, and the wide extent of

the formation area comparing to the previous event; it confirms the actual occurrence of a earlier preconditioning phase. Cross-section slices clearly show

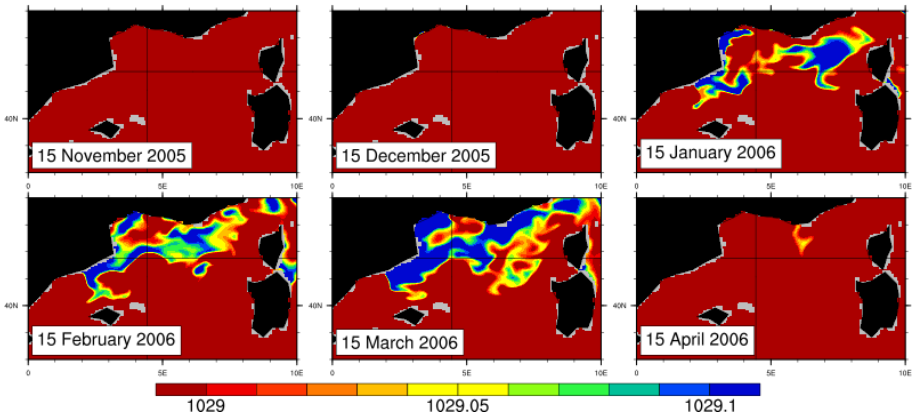

Figure 2.14: In-situ density (kg/m^3) at 8-m depth on the Gulf of Lion area during the 2005/2006 WMF event; black lines show slice locations (Figure 2.15 and Figure 2.16).

the near-homogenization of the water column already in January, but the erosion of surface stratification begins to be evident in December and remains noticeable still in April (not shown).

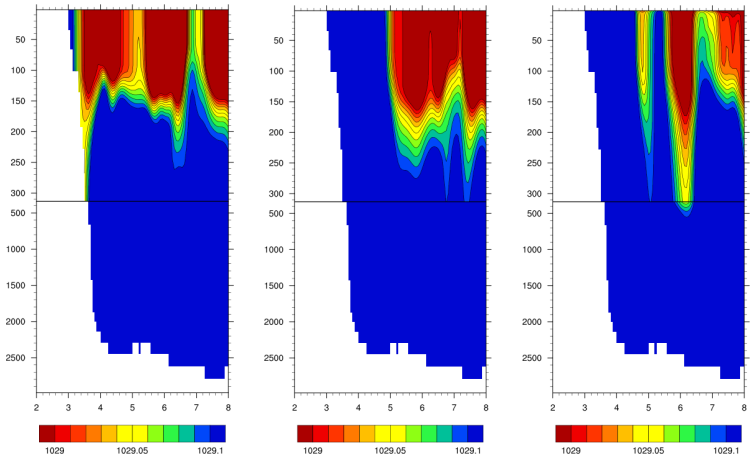

(a) 15 January (b) 15 February (c) 15 March

Figure 2.15: Longitudinal slice of in-situ density (kg/m^3) during the 2005/2006 WMF event, in the location shown in Figure 2.14.

ARGO Observations. During this WMF event, ARGO float 6900292 was floating exactly inside the formation area, in the Gulf of Lion; relative profiles are shown in Figure 2.17. The agreement between MFS Reanalysis and observation is very close, showing a complete homogenization of the water column already in January, nevertheless some little fluctuations in the near-surface layer.

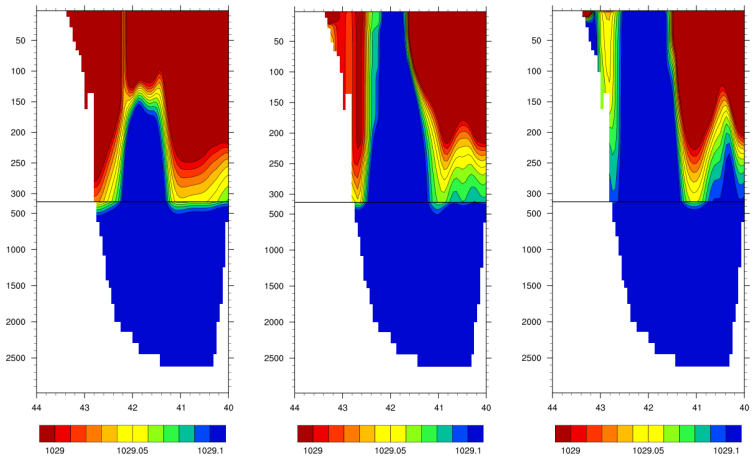

(a) 15 January (b) 15 February (c) 15 March

Figure 2.16: Latitudinal slice of in-situ density (kg/m^3) during the 2005/2006 WMF event, in the location shown in Figure 2.14.

Marshall Numbers. Table 2.2 shows Marshall Numbers values computed on a monthly average in the 2005/2006 heat flux minimum point. The Buoyancy Flux is maximum in December and decreases until April, when it becomes negative; computed values are of the same order of what expected by Marshall and Schott (1999). Computed thermal Peclet Number is very high, becoming closer to reference value (Marshall and Schott 1999) only in February; so, the thermal layer is much thinner than the convective layer during the whole WMF event. The high values of natural Rossby Number obtained show that the maximum depth involved into convective process is smaller than the scale l_{rot}. Flux Rayleigh Number is always two-three orders of magnitude higher than the value used by Jones and Marshall (1993) in their numerical work, but lies in the range 10^4-10^{13} employed by Klinger and Marshall (1995). Taylor Number is found in the expected range of values given by Jones and Marshall (1993), as for the vertical Ekman Number.
Figure 2.18 and Figure 2.19 show scatterplots obtained by (Ra_f,Ta) and (Ra_f,Ro^*), respectively. Comparing with Boubnov and Golitsyn (1990) and Klinger and Marshall (1995), it seems that the 2005/2006 Water Mass Formation event fall in a fully turbulent, three-dimensional regime, as we speculated in Section 2.1.

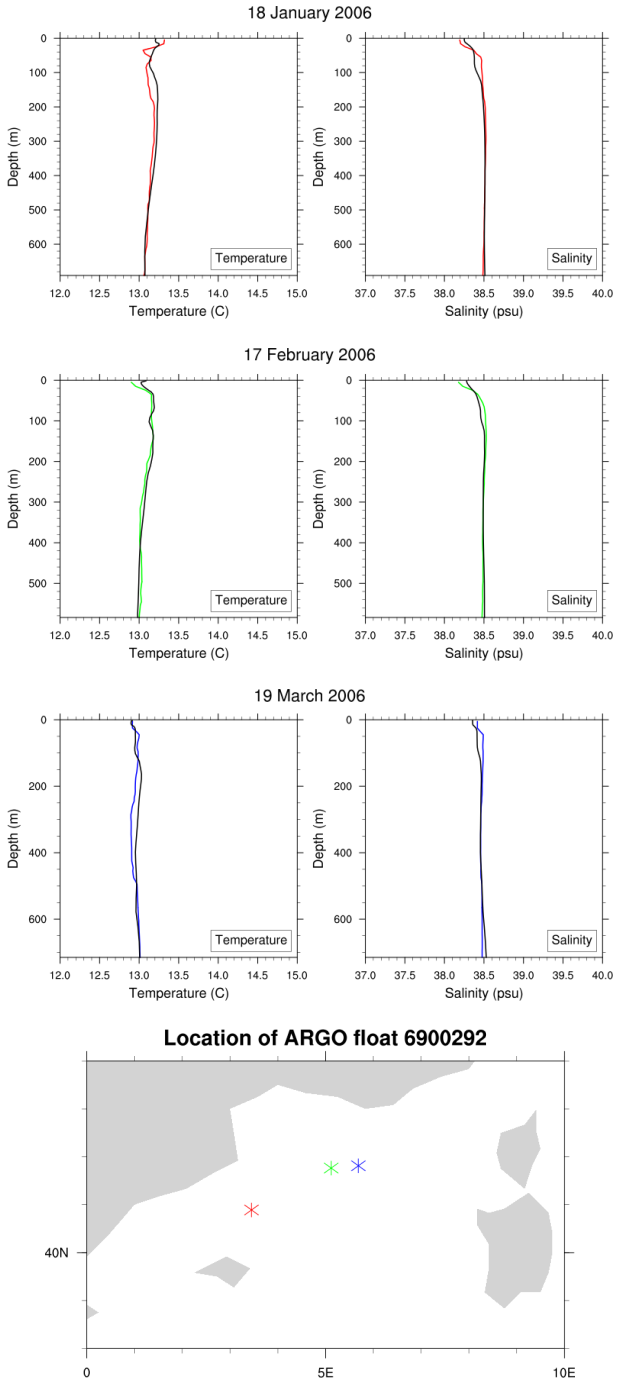

Figure 2.17: Comparison between MFS Reanalysis insitu temperature (°C) and salinity (psu) profiles (black lines), with ARGO float 6900292 measurements (coloured lines) in the Gulf of Lion area during the 2005/2006 WMF event.

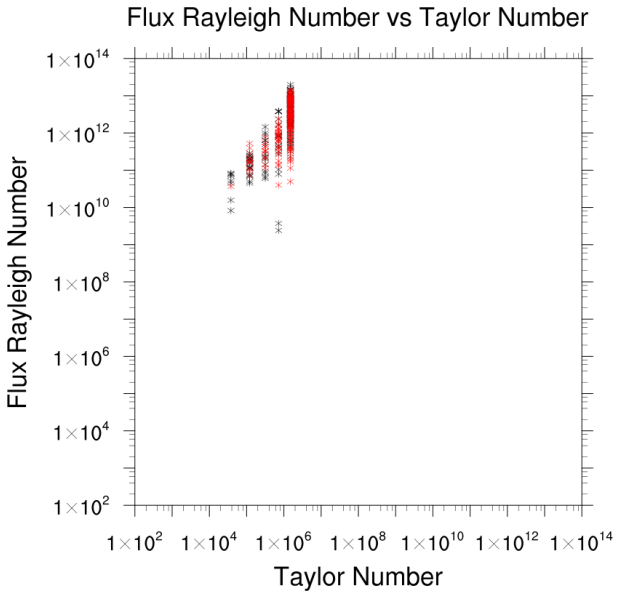

Figure 2.18: Scatterplot of Taylor Number vs flux Rayleigh Number obtained during 2004/2005 (black stars) and 2005/2006 (red stars) Water Mass Formation events. To be compared with Figure 2 of Boubnov and Golitsyn (1990).

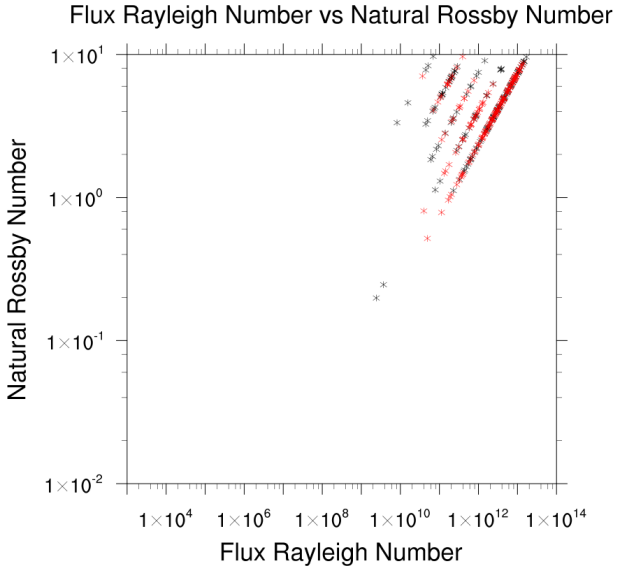

Figure 2.19: Scatterplot of Flux Rayleigh Number vs natural Rossby Number obtained during 2004/2005 (black stars) and 2005/2006 (red stars) Water Mass Formation events. To be compared with Klinger and Marshall (1995).

Table 2.1: Estimates of Marshall Numbers in the heat flux minimum point for the 2004/2005 WMF event in the Gulf of Lion, averaged for each month. Reference values from Jones and Marshall (1993) and Marshall and Schott (1999).

	Buoyancy Flux ($m^2\ s^{-3}$)	Thermal Peclet Number	Natural Rossby Number	Flux Rayleigh Number	Taylor Number	Vertical Ekman Number
Reference	10^{-7}	100	0.3	10^{9}	10^{2}-10^{8}	10^{-1}-10^{-4}
November	1.61×10^{-7}	808	5.62	6.26×10^{12}	1.29×10^{6}	0.97×10^{-3}
December	1.05×10^{-7}	364	6.36	2.60×10^{12}	0.69×10^{6}	2.14×10^{-3}
January	1.25×10^{-7}	163	4.36	5.09×10^{12}	1.50×10^{6}	0.82×10^{-3}
February	0.88×10^{-7}	834	3.96	3.61×10^{12}	1.36×10^{6}	0.88×10^{-3}
March	0.19×10^{-7}	1082	3.84	1.17×10^{11}	1.03×10^{6}	1.34×10^{-3}
April	-0.18×10^{-7}	1415	5.05	1.27×10^{11}	0.48×10^{6}	2.26×10^{-3}

Table 2.2: Estimates of Marshall Numbers in the heat flux minimum point for the 2005/2006 WMF event in the Gulf of Lion, averaged for each month. Reference values from Jones and Marshall (1993) and Marshall and Schott (1999).

	Buoyancy Flux ($m^2\ s^{-3}$)	Thermal Peclet Number	Natural Rossby Number	Flux Rayleigh Number	Taylor Number	Vertical Ekman Number
Reference	10^{-7}	100	0.3	10^{9}	10^{2}-10^{8}	10^{-1}-10^{-4}
November	1.25×10^{-7}	870	4.91	4.96×10^{12}	1.37×10^{6}	1.05×10^{-3}
December	1.77×10^{-7}	411	6.49	6.74×10^{12}	1.36×10^{6}	0.97×10^{-3}
January	0.65×10^{-7}	441	3.82	2.68×10^{12}	1.40×10^{6}	0.86×10^{-3}
February	0.58×10^{-7}	238	3.36	2.31×10^{12}	1.44×10^{6}	0.84×10^{-3}
March	0.17×10^{-7}	509	3.51	1.14×10^{11}	1.01×10^{6}	1.14×10^{-3}
April	-0.32×10^{-7}	364	4.59	-3.29×10^{11}	0.56×10^{6}	1.99×10^{-3}

2.3 Simulations of Water Mass Formation Events

In the Water Mass Formation process, the role of the surface latent heat flux is critical. To demonstrate this, two specific numerical configuration have been tested for the 2004/2005 and 2005/2006 WMF events in the Gulf of Lion: in the first one, the model is runned on its normal setup (Section 1.2.2), while in the second simulation the surface latent heat flux is turned off.

Water Mass Formation Rate. The left panel (*NORMAL* configuration) of Figure 2.20 presents the comparison between daily WMF rate values between the two events: the 2004/2005 Winter (black line) shows a single mode centered on late-February/early-March, while the 2005/2006 trend has a maximum on late-March and is smaller elsewhen. Further, the massive deep water formation begins in February for the 2004/2005 event, and already in January for the 2005/2006 one. The right panel of Figure 2.20 shows instead the WMF rate in the *NO LATENT* configuration: the average WMF rate for the 2004/2005 *NO LATENT* simulation is 4 times smaller respect to the *NORMAL* one, while in the 2005/2006 simulation there is a 6-factor of reduction.

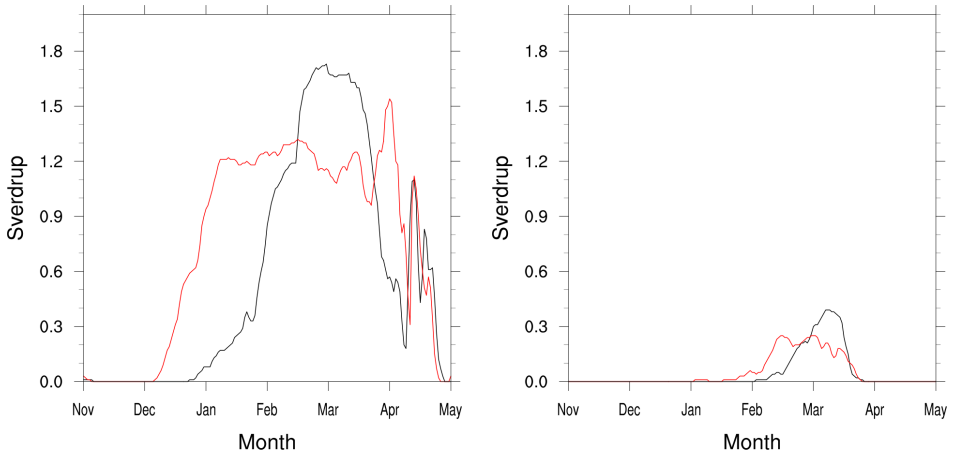

(a) NORMAL (b) NO LATENT

Figure 2.20: Simulated Water Mass Formation rate (Sv) in the Gulf of Lion area for two WMF events (2004/2005 and 2005/2006), with (panel *a*) and without (panel *b*) surface latent heat flux. In both panels, the black line corresponds to the daily 2004/2005 WMF rate, and the red line to the daily 2005/2006 WMF rate.

The comparison between the monthly contributions of WMF rate in the two simulations is shown in Figure 2.21. In the *NO LATENT* configuration, the WMF rate is non-zero only during February and March, but still one order of magnitude smaller than the *NORMAL* values.

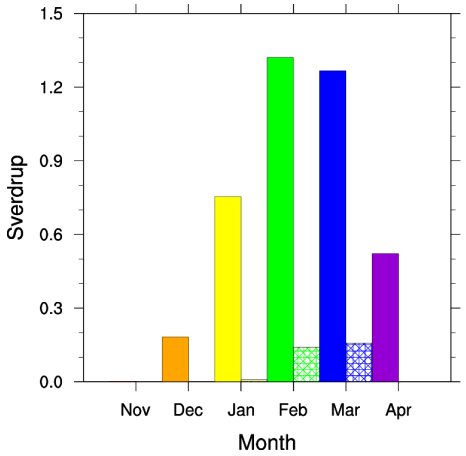

Figure 2.21: Comparison between the average simulated monthly WMF rate (Sv) for two WMF events (2004/2005 and 2005/2006), with (filled box) and without (stripped box) latent heat flux.

2.3.1 Analysis of 2004/2005 Water Mass Formation Event with Simulations

Atmospheric Forcing. For what concerns the 2004/2005 WMF event, Figure 2.22 shows that the latent heat flux is the main component of the total heat balance: indeed, in the *NO LATENT* configuration the minimum downward heat flux reached in the simulation is -475 W m^{-2}, while in the *NORMAL* configuration the minimum value is -1125 W m^{-2}. Heat budget are also very different between the two configurations; indeed, in the heat flux minimum point is estimated a heat loss of 32.9 kW/m^2 (from November 1st, 2004, to April 30th, 2005) for the *NORMAL* configuration, and a halved loss of 16.3 kW/m^2 for the *NO LATENT* simulation. Table 2.3 shows that the driving component of the heat balance is the latent heat flux in the *NORMAL* configuration; in the *NO LATENT* simulation, the sensible heat flux becomes the principal component.

Table 2.3: Correlations between total downward heat flux and heat balance components for the 2004/2005 WMF event.

Heat Component	NORMAL	NO LATENT
SW Radiation	0.51	0.63
LW Radiation	0.69	0.69
Sensible Heat	0.94	0.89
Latent Heat	0.96	–

Density Structure. The difference between the two configuration on the horizontal density patterns is clearly evident in Figure 2.23: during Febru-

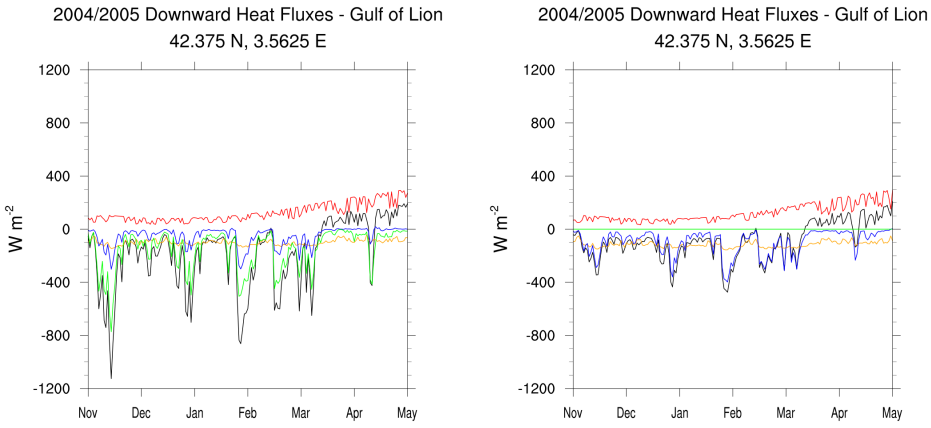

(a) NORMAL (b) NO LATENT

Figure 2.22: Downward heat flux (black line), with shortwave radiation (red line), longwave radiation (orange line), sensible heat flux (blue line), and latent heat flux (green line) components during the 2004/2005 Winter season, computed on the heat flux minimum point (42.4°N-3.6°E) in the Gulf of Lion area for the two configurations.

ary and March, for the *NORMAL* configuration the increase in density is widespread over the area, while for the *NO LATENT* one there is no evidence for a near-surface density increase. On the black line shown in Figure 2.23, cross-section slices have been drawn for January 15th (Figure 2.24), February 15th (Figure 2.25), and March 15th (Figure 2.26): there is a dramatic difference in density structure between the two simulations, with a completely eroded stratification in the *NORMAL* situation, and a more stable structure in the *NO LATENT* one.

ARGO Observations. The comparison of simulated profiles (in both configurations) and ARGO data in Figure 2.27 shows that turning off the surface latent heat flux causes an increase of the near-surface temperature and salinity, and a more noticeable thermocline/alocline in the subsurface layer during the whole Winter season. Apart from that, there are some differences between the *NORMAL* configuration and the observated profile in the upper layer, where ARGO profiles show generally a better homogenization of the water column, while simulated profiles exhibit permanence of stratification still in February.

2.3.2 Analysis of 2005/2006 Water Mass Formation Event with Simulations

Atmospheric Forcing. As in the previous case, latent heat flux is the main component of the total heat balance also during the 2005/2006 WMF event

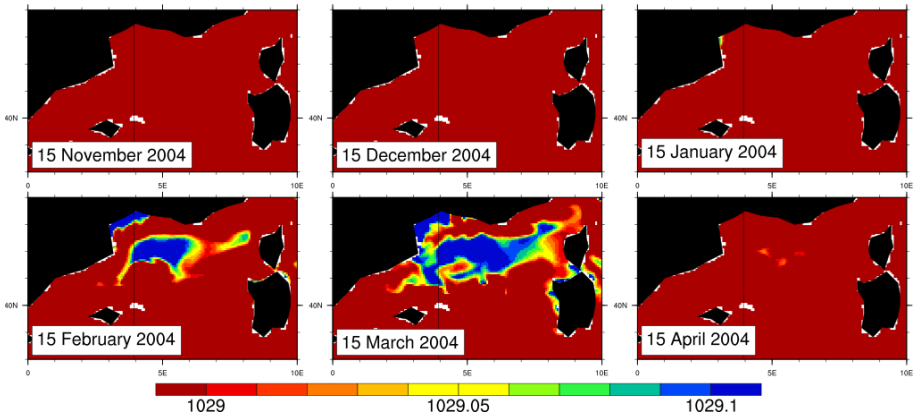

(a) NORMAL

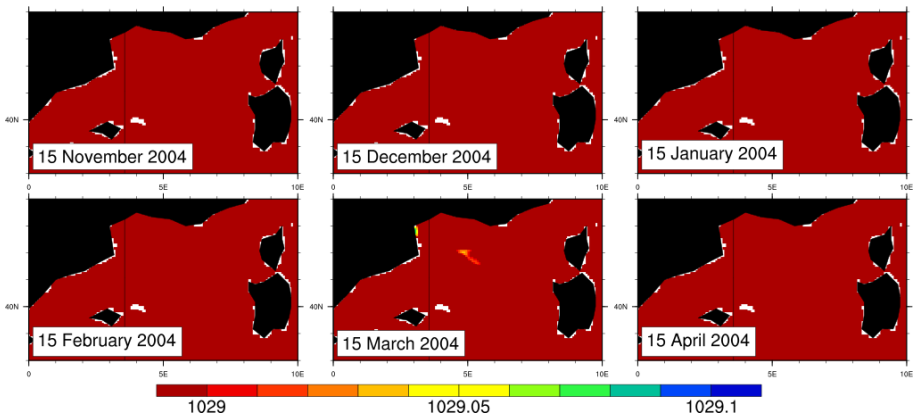

(b) NO LATENT

Figure 2.23: In-situ density (kg/m^3) at 8-m depth on the Gulf of Lion area during the 2004/2005 WMF event; black lines show slice locations (Figure 2.24, Figure 2.25, and Figure 2.26).

(Figure 2.28): in the *NO LATENT* configuration the minimum downward heat flux reached in the simulation is -470 W m^{-2}, while in the *NORMAL* configuration the minimum value is -962 W m^{-2}. The difference in the computed heat budget for the different configuration is dramatic: in the *NORMAL* simulation the heat flux minimum point exhibits a heat loss on 36.5 kW/m^2, and is riduced by a three-factor in the *NO LATENT*, being 12.9 kW/m^2. Surprisingly, from the correlation coefficients shown in Table 2.4 seem that sensible heat flux is the main component of the heat balance in both configurations, although in the *NORMAL* simulation values are comparable.

Density Structure. Figure 2.29 shows that already in January density increases enough to give way to deep water formation, in the *NORMAL* configuration. Instead, the *NO LATENT* configuration does not exhibit any increase in density in the uppermost 350 m. Density structure is quite different in the

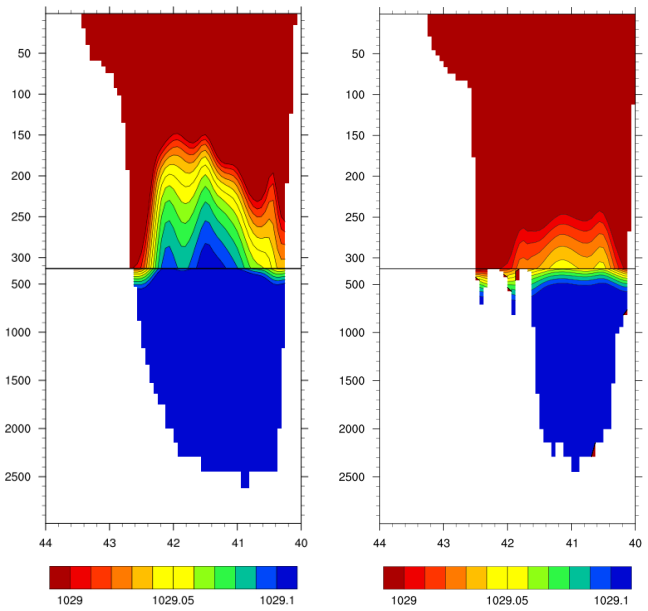

(a) NORMAL (b) NO LATENT

Figure 2.24: Latitudinal slice of in-situ density (kg/m^3) during the 2004/2005 WMF event, in the location shown in Figure 2.23.

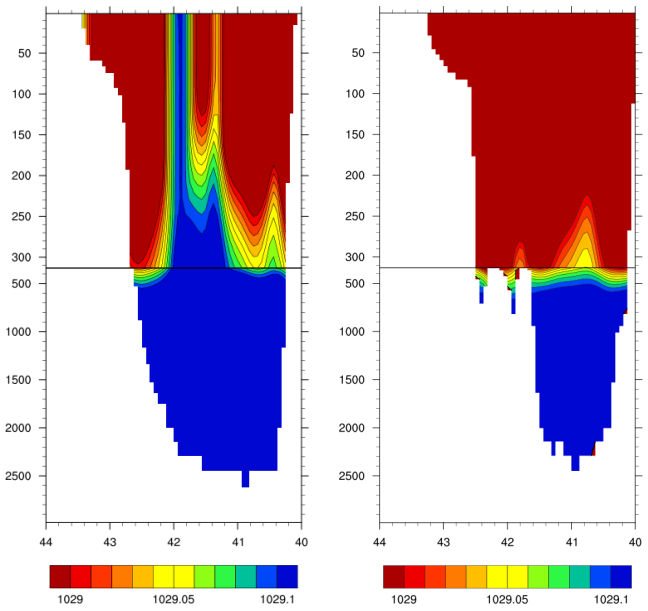

(a) NORMAL (b) NO LATENT

Figure 2.25: Latitudinal slice of in-situ density (kg/m^3) during the 2004/2005 WMF event, in the location shown in Figure 2.23.

two situations (Figure 2.30, Figure 2.31, Figure 2.32), but, respect to what we said in Section 2.3.1, stratification in the *NO LATENT* seems weaker in 2005/2006 event, with 1029 kg m^{-3} isoline reaching 120-m depth.

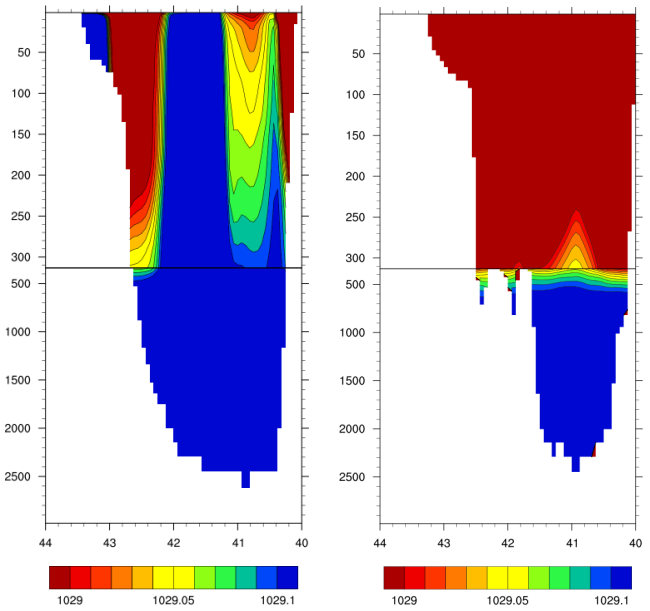

(a) NORMAL (b) NO LATENT

Figure 2.26: Latitudinal slice of in-situ density (kg/m^3) during the 2004/2005 WMF event, in the location shown in Figure 2.23.

Table 2.4: Correlations between total downward heat flux and heat balance components for the 2005/2006 WMF event.

Heat Component	NORMAL	NO LATENT
SW Radiation	0.59	0.76
LW Radiation	0.72	0.64
Sensible Heat	0.94	0.89
Latent Heat	0.92	–

ARGO Observations. Again, the absence of latent heat flux forcing at the surface causes an increase on both near-surface temperature and salinity, respect to the *NORMAL* model configuration (Figure 2.33), especially in the early part of the WMF event. There is more resemblance between *NORMAL* simulation and observation profiles, maybe because the surface forcing during this event is less intense than in 2004/2005 Winter.

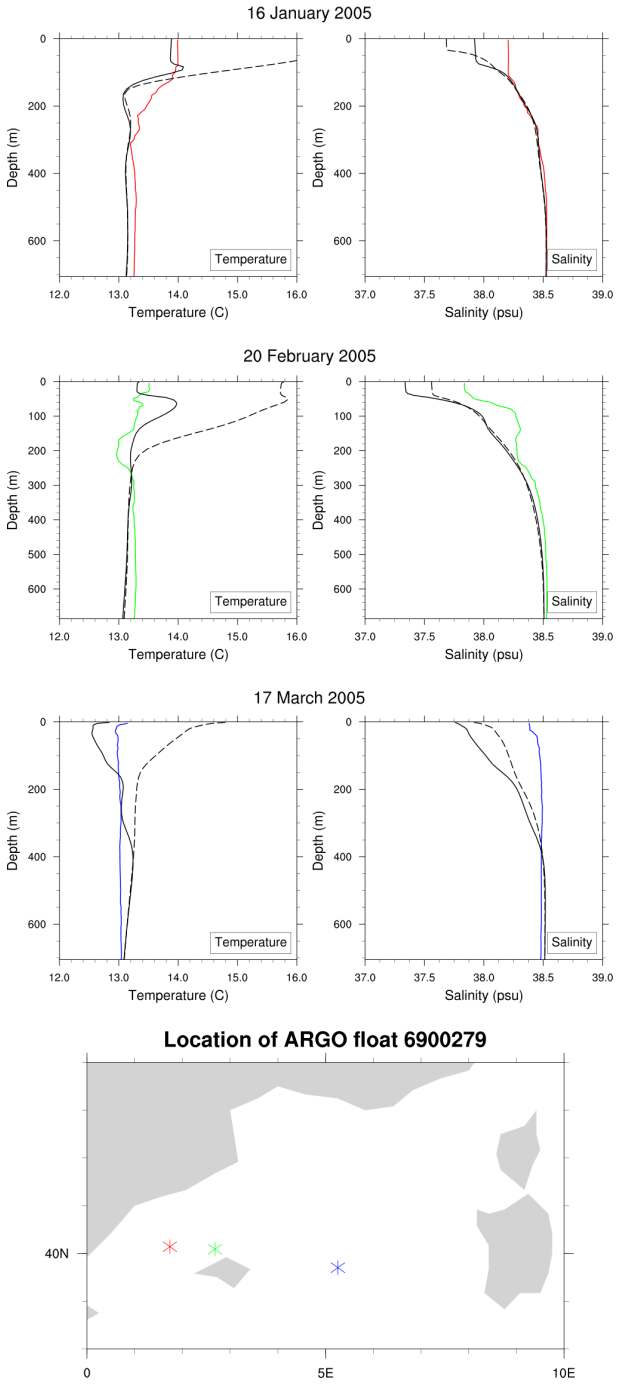

Figure 2.27: Comparison between MFS Reanalysis potential temperature (°C) and salinity (psu) profiles, with ARGO float 6900279 measurements in the Balearic area during the 2004/2005 WMF event; filled lines regard the *NORMAL* simulation, dashed lines the *NO LATENT* simulation.

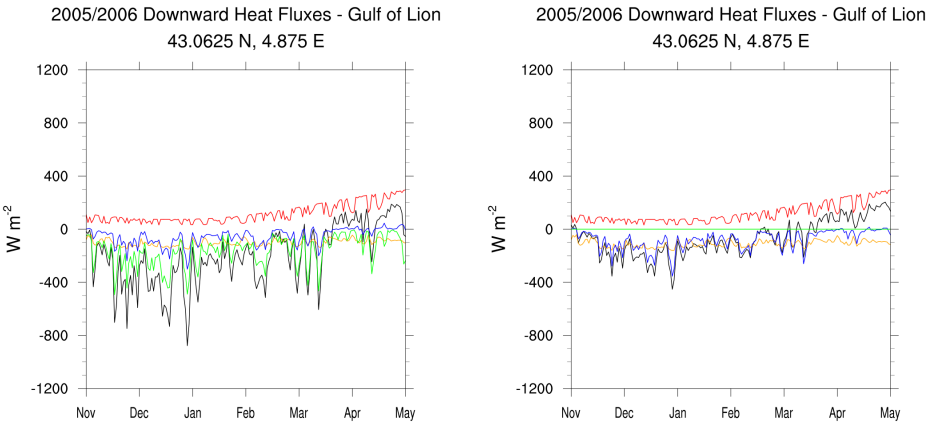

(a) NORMAL (b) NO LATENT

Figure 2.28: Downward heat flux (black line), with short-wave radiation (red line), long-wave radiation (orange line), sensible heat flux (blue line), and latent heat flux (green line) components during the 2005/2006 Winter season, computed on the heat flux minimum point (43.1°N-4.9°E) in the Gulf of Lion area for the two configurations.

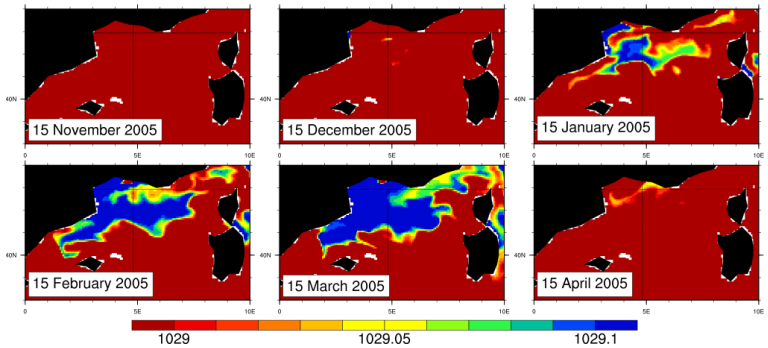

(a) NORMAL

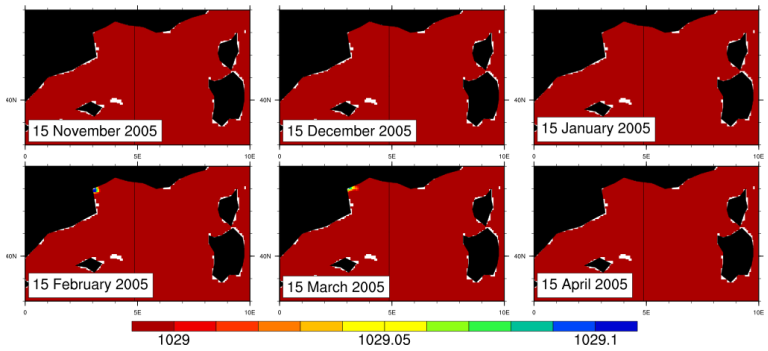

(b) NO LATENT

Figure 2.29: In-situ density (kg/m^3) at 8-m depth on the Gulf of Lion area during the 2005/2006 WMF event; black lines show slice locations (Figure 2.30, Figure 2.31, and Figure 2.32).

2.4 Observations of 2004/2005 and 2005/2006 Water Mass Formation Events

Smith et al. (2008) examine more accurately the wintertime characteristics of the Western Mediterranean Basin, through description and analysis of ARGO

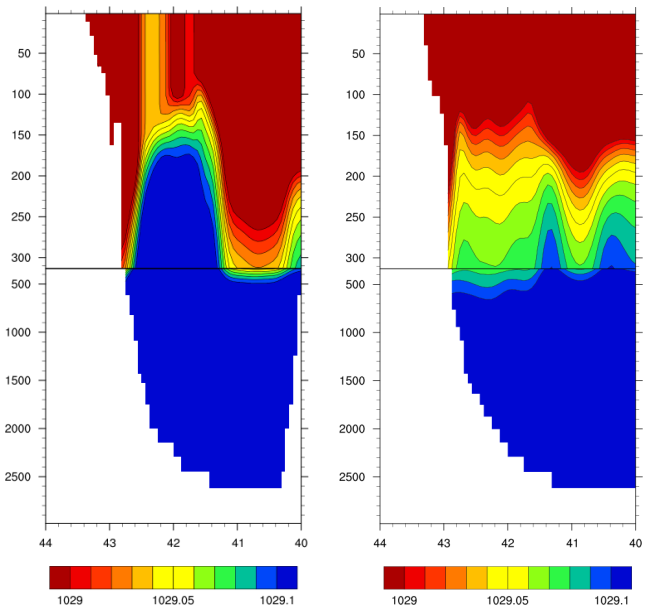

(a) NORMAL (b) NO LATENT

Figure 2.30: Latitudinal slice of in-situ density (kg/m^3) during the 2005/2006 WMF event, in the location shown in Figure 2.29.

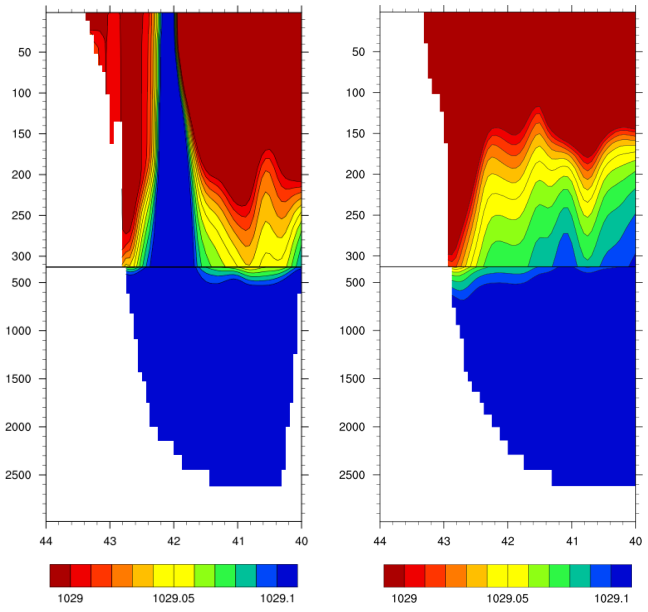

(a) NORMAL (b) NO LATENT

Figure 2.31: Latitudinal slice of in-situ density (kg/m^3) during the 2005/2006 WMF event, in the location shown in Figure 2.29.

float data collected during the Winter months of 2004/2005 and 2005/2006. To support their conclusions, they use daily air-sea fluxes data from NCEP/NCAR Reanalysis (Kalnay et al. 1996), computed at two separate grid cells (near 40.9°N, 3.75°E for the 2004/2005 event and 42.9°N, 7.5°E for the 2005/2006

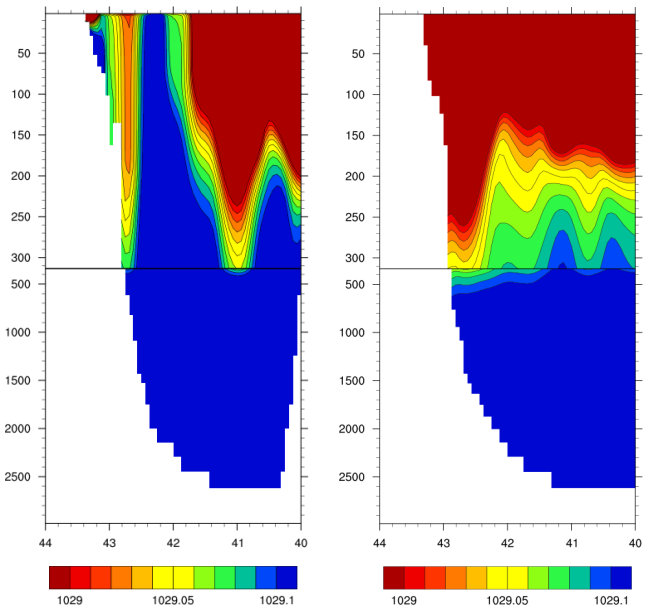

(a) NORMAL (b) NO LATENT

Figure 2.32: Latitudinal slice of in-situ density (kg/m^3) during the 2005/2006 WMF event, in the location shown in Figure 2.29.

event) where ARGO float sampled occurring deep water convection.

2.4.1 2004/2005 Event

ARGO float 6200279 time series (Figure 2.34) show convection occurring in the Catalan subbasin during March 2005; time evolution of potential temperature vertical profiles exhibits a distinct transition from strong, surface thermal stratification in November to a well-mixed homogeneous water column by mid March. Figure 6 of Smith et al. (2008) displays that water column cooling between November and late January was largely restricted to the upper 200 m in the Catalan subbasin, and surface forcing have been of sufficient duration and magnitude (by late February) to overcome the density gradient, progressively mixing and entraining deeper layers. This view seems to confirm some of our statements done in Section 2.2.1. Smith et al. (2008) also report that some ARGO float in the Western Mediterranean Basin detected a low salinity surface layer of Atlantic Water during 2004/2005 Winter, which persisted over much of the upper water column of the Provençal and Ligurian subbasins; this fresh surface layer prevented mixed layer entrainment of the LIW and, inhibiting the preconditioning phase required for deep convection in that area. NCEP/NCAR daily reanalysis air-sea flux data evidence four period (lasting less than 3 days) when heat flux in the Catalan subbasin reaches or exceeds

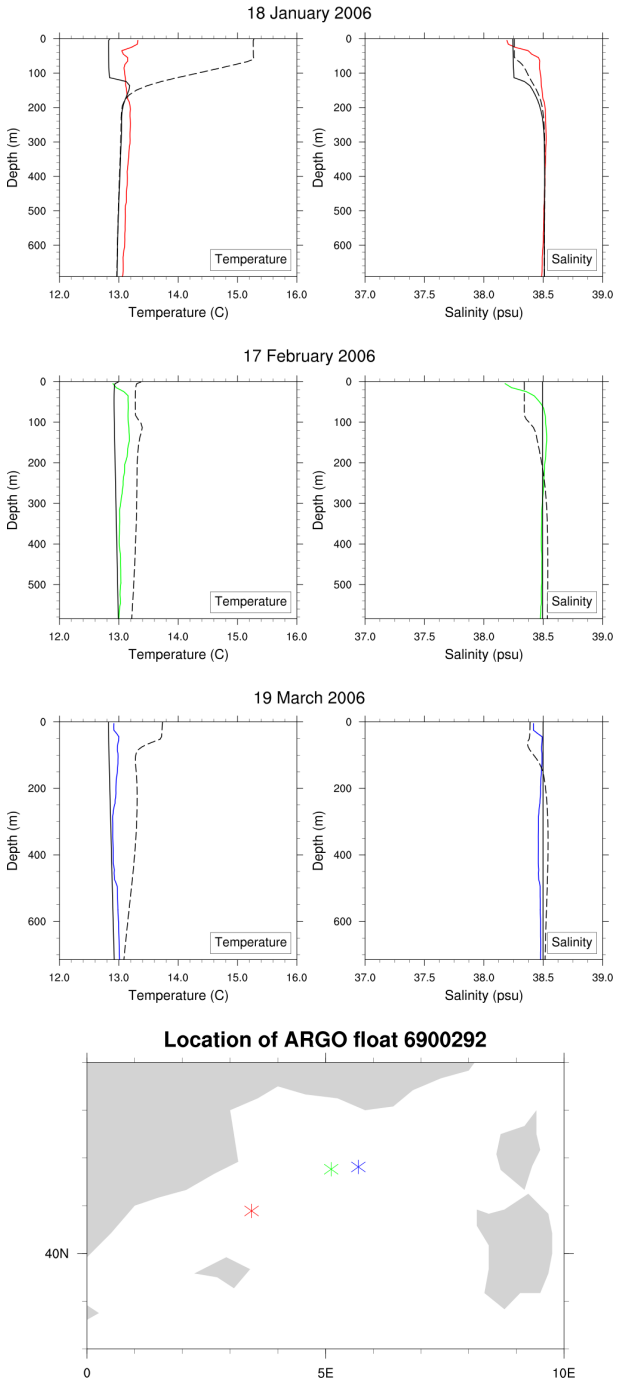

Figure 2.33: Comparison between MFS Reanalysis potential temperature (°C) and salinity (psu) profiles, with ARGO float 6900292 measurements in the Gulf of Lion area during the 2005/2006 WMF event; filled lines regard the *NORMAL* simulation, dashed lines the *NO LATENT* simulation without surface latent heat flux.

600 W/m^2, suggesting that the major meteorological forcing took place for short periods (Figure 2.36).

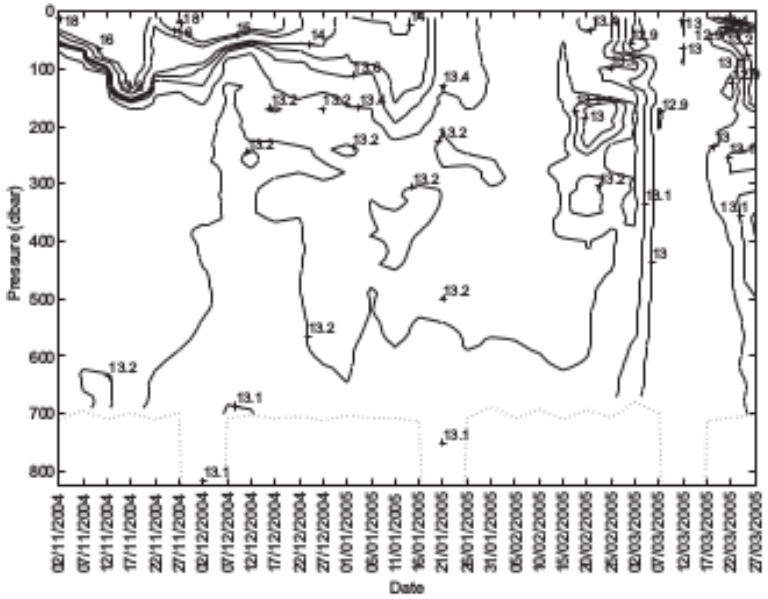

Figure 2.34: Time series of vertical potential temperature profiles from ARGO float 6900279, limited to shallow dive depth (700 m), during the 2004/2005 WMF event. Taken from Smith et al. (2008).

2.4.2 2005/2006 Event

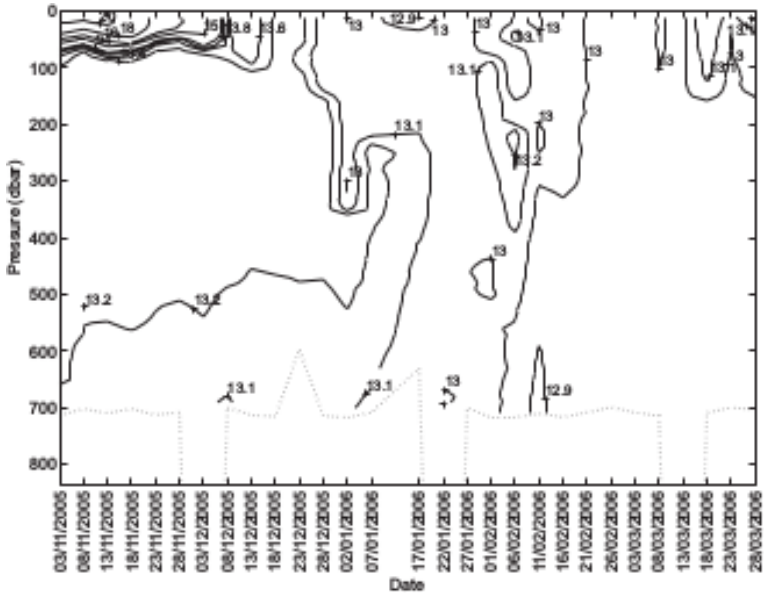

Figure 2.35: Time series of vertical potential temperature profiles from ARGO float 6900293, limited to shallow dive depth (700 m), during the 2005/2006 WMF event. Taken from Smith et al. (2008).

ARGO float 6900293 detects newly-formed WMDW during March 2006 in the Ligurian subbasin (Figure 2.35); although the newer WMDW at 2000 m in the WM is warmer than the older, it also has a sufficiently high salinity to be denser (Smith et al. 2008). The layers below 200-m depth are progressively entrained,

creating a continuously deepening mixed layer which is exposed to surface forcing, suggesting presence of the LIW into the mixed layer. NCEP/NCAR data from the Ligurian subbasin show that heat flux did not exceed 400 W/m^2 and was consistently weaker, with less distinct episodes observed in comparison to the previous Winter (Figure 2.36).

In our opinion, nevertheless the very extended formation area characterizing this WMF event, the Ligurian subbasin cannot give a considerable contribution to newly-formed WMDW, or at least this contribution must be lower than the MEDOC area one. For this reason, we choose to analyze ARGO float 6900292 in Section 2.2.2, being floating inside the classical WMF area in the Gulf of Lion.

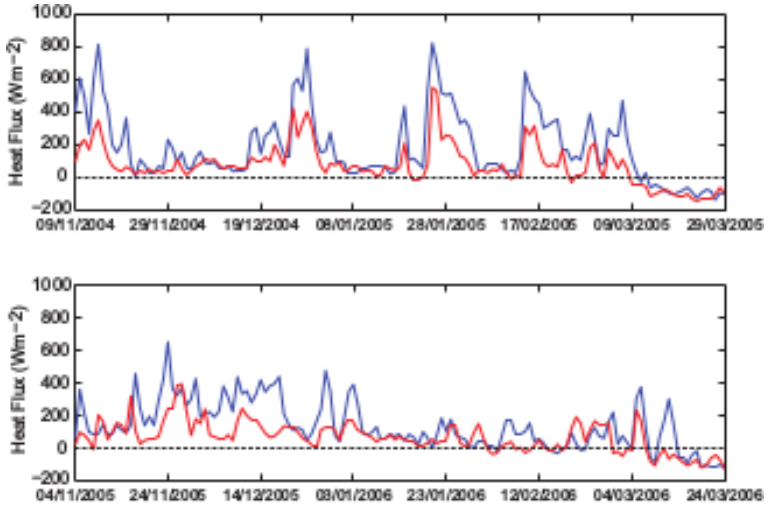

Figure 2.36: NCEP/NCAR Reanalysis daily heat flux for the 2004/2005 (top) and 2005/2006 (bottom) Winters; blue lines represent values in the Catalan subbasin, red lines regard the Ligurian subbasin. Taken from Smith et al. (2008).

2.4.3 General Remarks

Through analysis of the ARGO and NCEP/NCAR Reanalysis data, for Smith et al. (2008) it is apparent that surface cooling was stronger and more prolonged within the Catalan subbasin during the 2004/2005 Winter, compared to the 2005/2006 Winter in the Ligurian Sea, leading to a greater heat loss; nonetheless, the 2004/2005 WMDW had indistinguishable density to the 2005/2006 one. As a major difference between the preconditioning phases, they underline the presence of a shallower and saltier LIW in the Ligurian subbasin during November 2005, which should promote homogenization of the surface and intermediate waters during Winter, despite weaker buoyancy fluxes. From the combination of shallow, warm and saline intermediate waters and saline surface

waters in the Ligurian subbasin during Winter 2005/2006, it seems that the homogenization of surface and intermediate waters required lower cumulative buoyancy loss; so, the preconditioning phase was concluded by mid-January in 2006, compared to late-February/early-March in 2005.
Lopez-Jurado et al. (2005) report of a number of WMDW formation events occurred in the 2004/2005 Winter, with Canals et al. (2006) and Schroder et al. (2006) indicating new WMDW formed off the Gulf of Lion shelf at 2000 m and detecting it in the Provençal subbasin with similar properties to the new WMDW identified by Smith et al. (2008). These findings suggest to Smith et al. (2008) that Water Mass Formation process in the Western Mediterranean is regionally variable, and can occur in a number of regions within the basin, where the meteorological and hydrographic characteristics required for deep water production coincide. Our point-of-view is slightly different, because we still think the main WMF area is centered around the MEDOC Group (1970) area, but actually both horizontal extension and vertical strength of the deep convection fundamentally depend on atmospheric forcing and pre-existing water column structure.

Chapter 3

Coastal Upwelling in the Mediterranean Sea

According to Bakun and Agostini (2001), the general effect of the wind stress on the sea surface can be separated in (1) **coastal upwelling** resulting from the flow divergence due to offshore transport of surface waters from a solid coastal boundary, the driving force being the component of wind stress which is parallel to the coast, and (2) **open-ocean upwelling** induced by spatial variation in the pattern of sea surface wind stress, the driving force being the wind stress curl. In the following, we will focus on the Coastal Upwelling process in the Mediterranean Sea, starting from the Ekman theory, and passing through the principal studies about the principal upwelling zones in the World Ocean.

3.1 Ekman Upwelling Theory

A divergent flow of surface waters induces uplift of subsurface waters, in order to conserve seawater mass. Addressing time scales of variation long enough to allow a steady-state approach, the Ekman (1905) approximation can be used, in which

$$Q_E^y = \int_{-2\delta_E}^{0} v_E dz = -\frac{\tau_x}{\rho_0 f}, \tag{3.1a}$$

$$Q_E^x = \int_{-2\delta_E}^{0} u_E dz = \frac{\tau_y}{\rho_0 f}. \tag{3.1b}$$

The actual water transport responding to the applied wind stress is computed in the Ekman layer, the uppermost region of the water column where wind

forcing takes effect; the Ekman layer depth δ_E can be defined as the e-folding depth of the wind-induced currents (Patara et al. 2009), or as the depth where turbulent stress vanishes (Brink 1983). The speed component $\mathbf{u}_E$ =(u_E,v_E) are written from the analitical solution of the Ekman problem, which can be found in (Vallis 2006). Following this steady-state approximation, wind-driven transport must be perpendicular to the right of the wind direction; assuming a wind stress $\tau_\parallel$ parallel to the coast, Equation 3.1 allows to obtain the transport magnitude as

$$Q_E = \frac{\tau_\parallel}{\rho_0 f}. \tag{3.2}$$

Thus, near a coastal region of the Northern Hemisphere located on the left side of the wind stress, Ekman transport upwells deep waters, characterized by lower temperature and higher density, producing a Coastal Upwelling event. The principle of conservation of mass in an incompressible fluid, such as seawater, is expressed by the continuity equation

$$\frac{\partial u}{\partial x} + \frac{\partial v}{\partial y} + \frac{\partial w}{\partial z} = 0 \quad \Rightarrow \quad \frac{\partial w}{\partial z} = -\nabla_h \cdot \mathbf{u}_h. \tag{3.3}$$

Integrating in the surface Ekman layer between $z = 0$ and $z = -\delta_E$, we can obtain

$$\begin{aligned} w_E = w(-\delta_E) &= \mathbf{k} \cdot \nabla \times \left(\frac{\boldsymbol{\tau}}{\rho_0 f} \right) \\ &= \frac{1}{\rho_0 f} \left(\mathbf{k} \cdot \nabla \times \boldsymbol{\tau} + \frac{\beta_0 \tau_x}{f} \right), \end{aligned} \tag{3.4}$$

where we assume zero vertical velocity at the surface. For the Mediterranean Sea, δ_E lies between 20 and 40 m, as estimated by the scaling formula (Pond and Pickard 1983)

$$\delta_E = \pi \sqrt{2 \frac{A_v}{|f|}}, \tag{3.5}$$

where the vertical eddy coefficient A_v normally lies between 10^{-2}-10^{-3} $\mathrm{m^2 s^{-3}}$ (Tonani et al. 2008). The Coriolis parameter in (3.4) is $f = f_0 + \beta_0 y$, and its addends can be approximated as

$$f_0 = 2\Omega \sin\phi, \quad \beta_0 = \frac{\partial f}{\partial y} = \frac{2\Omega}{a} \cos\phi,$$

where a and Ω are the Earth radius and angular velocity, respectively, and ϕ is the latitude.

The upwelling vertical velocity can also be evaluated from numerical models. As before, the continuity equation (3.3) is integrated over the Ekman layer, to obtain

$$w_m = w(-\delta_E) = w(\eta) + \int_{-\delta_E}^{\eta} \nabla_h \cdot \mathbf{u}_h dz, \tag{3.6}$$

where now

$$w(\eta) = \frac{D\eta}{Dt} + \left(E - P - \frac{R}{A}\right) \tag{3.7}$$

is the free-surface boundary condition, accounting for the total derivative of the free surface η and for the water balance at the interface. For practical reasons, the material derivative is approximated with the local derivative, so

$$\frac{D\eta}{Dt} \approx \frac{\partial \eta}{\partial t} \approx \frac{\Delta \eta}{\Delta t} = \frac{\eta(t + \Delta t) + \eta(t)}{\Delta t}.$$

Island Effect. The classical conceptual model of Ekman Coastal Upwelling, as derived from Sverdrup (1938), consists in a very long straight coastline, in order to avoid the establishment of a horizontal component in the offshore transport; in a realistic case, the island must be very large to apply this approximation. Instead, according to Bakun and Agostini (2001), for a relatively small island lying in the path of a large scale wind flow, Ekman transport is directed toward the left side of the island (looking downwind), and away from the right side: the water accumulating on one side may flow around the island in response to the resulting alongshore pressure gradient, to fill the loss of water on the other side. For larger islands, where quasi-geostrophic dynamics operate, coastal trapped waves have the same effect, propagating entrained velocity fields around the island (Gill and Clarke 1974).

3.2 Coastal Upwelling Studies

After Ekman (1905) pioneering work, many other studies treated with wind forcing on coastal areas. Most early estimates of large-scale wind stress distribution were based on the U.S. Hydrographic Office Pilot Chart wind data (Hidaka 1958): for example, using that database Wooster and Reid (1963) calculate offshore Ekman transport and describe major Coastal Upwelling regimes in terms of upwelling indeces. In his classical review work, Smith (1968) means for upwelling "an ascending motion, of some minimum duration and extent, by which water from subsurface layers is brought into the surface layer and is removed from the interested area by horizontal flow"; furthermore, he recognizes

the wind stress as the most important driving force for Coastal Upwelling.
Upwelling features can propagate away from their formation area. Charney (1955) observes that Coastal Upwelling systems are confined to the neighbourhood of the coast only on timescales shorter than Rossby waves period; indeed, Anderson and Gill (1975) observe that the propagation of such waves widens the upwelling zone and makes it a nonlocal phenomenon. Aside, advection by cross-shore currents modifies Coastal Upwelling system on long timescales (Philander and Pacanowski 1981).

3.2.1 Near-Surface Dynamics

The near-surface regime of Coastal Upwelling can be defined as the region roughly coinciding with the turbulent surface Ekman layer; in most upwelling regions, this means the upper 10-30 m of the water column, but its depth varies considerably with time and space (Brink 1983). Apart from the surface Ekman layer, defined in Section 3.1, upwelling systems include also *upwelling fronts*, *upwelling centers*, and *upwelling filaments*.

Coastal Upwelling Front. Mooers et al. (1976) treats the upwelling front as an upwelled pycnocline, so that the frontal formation is given by a passive advective process. Instead, DeSzoeke and Richman (1981) states that such density fronts follow from the advection of recently upwelled water, then resulting from a splitting of the pycnocline into an upper layer front and a weakened nearshore thermocline. However, Pedlosky (1978) model demonstrates that an initial pronounced pycnocline is not necessary for the formation of a coastal front.
Technically, the upwelling front is a region of strong near-surface horizontal density gradient, which can be thought of as a clear discontinuity in density caused by the Coastal Upwelling process. It is known that, through the "thermal wind" relation

$$f\frac{\partial v}{\partial z} = -\frac{g}{\rho}\frac{\partial \rho}{\partial x}, \tag{3.8}$$

which links vertical shear of the alongshore velocity v with horizontal density gradient, fronts are expected to cause an alongshore jet, affecting surface Ekman transport through nonlinear coupling (Brink 1983).

Three-Dimensional Upwelling Systems. An upwelling center is defined as an area of intensified Coastal Upwelling having comparable alongshore and

offshore spatial scale. It may be helpful to differentiate between *upwelling centers*, broad extended structures attached to the coast, and *upwelling filaments*, elongated bands of upwelled water which may protrude far offshore. In many cases the structures appear to be influenced by local, both coastal and bathymetric, topography. In a simple coastal two-layer model, with the upper layer depth d being much smaller than the lower layer and neglecting wind forcing and friction, the potential vorticity

$$P = \frac{\xi + f}{d}$$

is conserved for a given fluid parcel; so, a locally vorticity decrease causes a decrease of upper layer depth in order to conserve P, and the consequent reduction of the upper layer corresponds to upwelling. Using this kind of model, Yoshida (1967) shows that the influence of a cape into an alongshore motion is to accelerate locally the flow: when the motion is southward (northward) along an eastern oceanic boundary in the Northern Hemisphere, this causes a relative raising (lowering) of the interface at the coast, enhancing upwelling (downwelling) at the cape. Nonetheless, numerical evidences from Peffley and O'Brien (1976) suggest that bottom topography structures are more important than coastline curvature in causing localized upwelling.

One of the better known Coastal Upwelling centers in the world is found near 15°S, off the coast of Peru (Brink et al. 1981): its structure is defined by the sea surface temperature distribution, which generally shows the coldest water near the coast, and warmer water farther offshore and in both directions alongshore from the center. As observed off Oregon in weak wind conditions (Curtin 1979), the alongshore density nonuniformity of the Peru feature is limited to the upper 20-40 m, so the strong three-dimensionality occurs mainly in the near-surface regions. The variability in strength and size of the Peru center is clearly correlated to the local alongshore wind stress; during weak winds, the structure tends to become more irregular, with fronts and warm/cold patches appearing (Brink et al. 1980). Upwelling filaments, on the other hand, represent irregular protrusions of upwelled water advected far beyond the coast. Their strength is related to the local alongshore wind stress, but they can remain intact offshore for many days before their physical structure deteriorates. Coastal Upwelling systems can present a large variety of different characteristics. Indeed, Peru upwelling features rarely extend far beyond the shelf break, and the surface offshore flow component apparently is largely determined by Ekman dynamics (Brink 1983). Conversely, the filaments off California break

far beyond the shelf, having flow fields which are apparently not well understood using Ekman theory. Lastly, the upwelling center near Cape Town (South Africa) is complicated by the presence of a strong persistent current and an upwelling front located just offshore (Bang 1973), and its development is at least partially constrained by the large-scale dynamics.

3.2.2 Observations of Coastal Upwelling Systems

Among the different observational campaigns on Coastal Upwelling systems in the World Ocean, we can cite the Coastal Upwelling Ecosystems Analysis (CUEA) programs of Oregon (1973, CUE-II; Halpern (1976)) and Peru (1977, JOINT-II; Smith (1981)), the two Coastal Ocean Dynamics Experiments off northern California (1981 and 1982, CODE I and II; Winant et al. (1987)), and the CUEA experiment off northwest Africa (1974, JOINT-I; Halpern (1977), Badan-Dangon et al. (1986)). Smith (1981) revises observations from different midshelf locations in the three major CUEA field programs, finding in each case that, for the time mean and for low frequency fluctuations (periods greater then 47 hours), the offshore transport in the surface Ekman layer agrees with (3.4). Similarly, it has been observed that both the surface heat flux and cross-shelf advection of heat are large in Coastal Upwelling regions, being important components of the heat balance as recognized by Bryden et al. (1980), Richman and Badan-Dangon (1983), Lentz (1987), Rudnick and Davis (1988).

Mixed Layer in Coastal Upwelling Zones. The surface Ekman layer is that region of the water column where turbulent shear stresses are non-negligible and where the applied wind stress is absorbed; for this reason, the water is generally well-mixed (Brink 1983). Indeed, in the surface layer, turbulence is sufficient to overcome stratification, causing homogenization of the density field; below this region, stratifications inhibits turbulence (Turner 1979) which becomes weaker and intermittent (Dillon and Caldwell 1980). Periods when near-surface waters are characterized by weak vertical gradients are a common feature of temperature observations from Coastal Upwelling regions (Lentz 1992). Surface mixed layer depth can be defined as the maximum depth over which the observed temperature is within some ΔT of the sea surface temperature. Averages and standard deviations of the surface mixed layer depth range from 2 m over the Oregon shelf to about 10 m over the northwest Africa and northern California shelves; but, because the values distribution is highly skewed, the mean surface mixed layer depth does not represent the

"most representative" value. Lentz (1992) find a clear relationship between surface mixed layer depth and wind stress magnitude in all locations considered, such that stronger winds result in a deeper surface mixed layer, with a lag time of typically 6-12 hours; however, the magnitude of the response to wind stress varies considerably among the regions.

The transition problem is not easy to solve. Considering an idealized example of *mixed layer deepening*, Niiler (1975) demonstrates that the Ekman transport sets up within half an inertial period, and the Ekman layer depth increases monotonically with time; the maximum depth is imposed by the balance of the wind stress and by the rate of surface heating. The problem of *mixed layer shoaling* can also be solved (Davis et al. 1981), but it is complicated by the need to account for momentum which remains in the previously turbulent water.

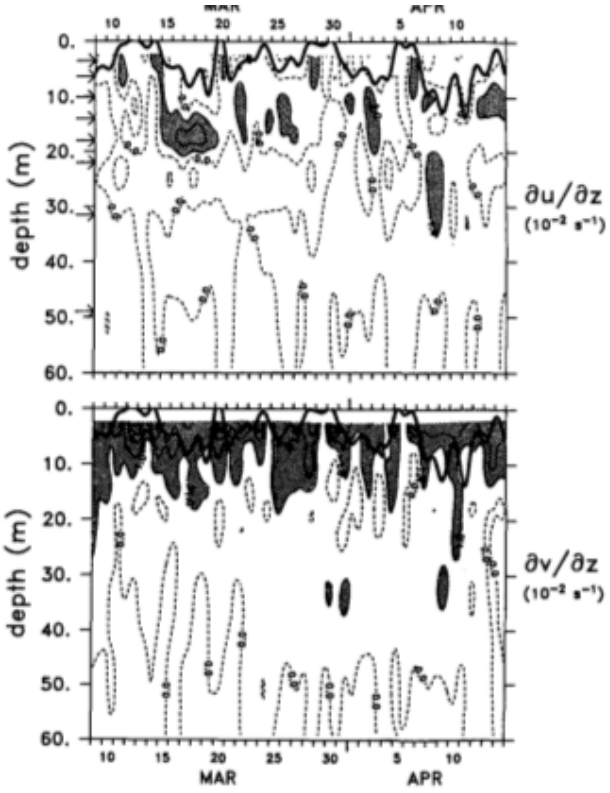

Figure 3.1: Contour plots of the vertical shear in the cross-shore u (top) and alongshore v (bottom) velocities, during the CUEA JOINT-II experiment in Peru (1977). Taken from Lentz (1992).

Velocity Structure. The near-surface, mean horizontal flow in Coastal Upwelling regions has a substantial offshore component, with a magnitude consistent with the expected Ekman transport and confined within the uppermost 40-m layer. Lentz (1992) observes that the vertical shear in the cross-shelf

velocity often has a subsurface maximum in the upper 10-30 m layer, while the maximum vertical shear typically lies just below the mixed layer; instead, the maximum vertical shear in the alongshelf velocity occurs at or near the surface (Figure 3.1).
Current vertical velocities are difficult to directly measure, because of their extremely low values (less than 1 m day^{-1}). However, in corrispondence of open-ocean submesoscale features, arising as a result of nonlinear interaction of mesoscale eddies in regions of strong shears, large vertical velocities higher than 10 m day^{-1} may occur (Levy et al. 2001); it can be difficult to detect such structures using numerical models, unless having a properly high spatial resolution (Patara et al. 2009).

Water Mass Transport. It is possible to compare Q_{ML}, the cross-shelf transport in the surface mixed layer, with the Ekman transport (3.2), attempting to account for variations in the thickness of the surface boundary layer by mooring measurements. The magnitude of Q_{ML} calculated by Lentz (1992) is generally smaller than the magnitude of Q_E, because Equation 3.2 only account for the wind-driven transport while Q_{ML} may include other contributions, such as interior pressure-driven flows. To determine whether the flow extending below the surface mixed layer could account for the difference of magnitude between Q_{ML} and Q_E, the transport can be computed introducing a transition layer between the surface mixed layer and the interior: Lentz (1992) obtains that the agreement between Q_{ML} and Q_E is much closer. His observations indicate that a significant fraction of the wind-driven transport occurs below the surface mixed layer; that is, the surface boundary layer as defined by momentum is thicker than the surface mixed layer.

3.2.3 Mediterranean Sea Upwelling Patterns

In the ocean, the surface boundary layer response to wind stress forcing is a key element in continental-shelf processes, such as upwelling (Lentz 1992); focusing on the Mediterranean Basin, we could mention the Gulf of Lion and the Sicily Strait as examples of extended shelf areas. The actual Coastal Upwelling response has a scale width given by the Rossby radius of deformation; computed estimates of the radius for temperate values generally does not exceed several tens of km, although the continental shelf width may provide an additional offshore scale for Coastal Upwelling (Yoshida 1967).
Because of the convoluted and complex topographic relief of the Mediterranean

coastlands, strong spatial patterning of the sea surface wind stress is to be expected (Bakun and Agostini 2001). Meteorological large-scale features in the Mediterranean Sea are reflected in the gross distribution of resulting wind-induced Coastal Upwelling patterns. The major Coastal Upwelling zones in the Mediterranean Basin are:

1. Libian (during spring) and Algerian (in Summer and fall) coastlines, due to a southward wind stress flowing in those periods;

2. the Eastern Aegean Sea, where upwelling is observed throughout the year, becoming remarkably intense in the Summer and fall seasons, in response to strong northerly wind stress and correspondingly intense westward Ekman transport; vertical velocities can reach 1.5 m day^{-1} within a band placed along the eastern boundary of the sea;

3. the Eastern Ionian Sea along the western coast of Greece, where vertical velocity reaches intensities greater than 0.5 m day^{-1};

4. the Gulf of Lion, along the southern France coastline, in response to the Tramontane wind (sloping down to the Mediterranean coasts from the topographic gap between the Pyrenees and the Massif Central mountains) and the Mistral wind (generated in the valley of the Rhone river);

5. western and/or southern sides of the major islands, such as Sicily and Cyprus, due to the already exposed *island effect* (Section 3.1).

Several Mediterranean upwelling areas exhibit substantial vertical velocity by world standard (Bakun and Agostini 2001). Furthermore, because of the relatively high latitude location of the Mediterranean Basin (especially its northernmost part), a given intensity of offshore Ekman transport is accompanied by a much higher input of turbulent mixing energy by the wind, with respect to the case at lower latitude locations (Bakun 1996).

3.3 A New Upwelling Index

The frequency of observations is not high enough, both in space and time, to allow an accurate description of the large-scale variability of the ocean. This limitation can be overcome by applying a data assimilation system which allows, thanks to a numerical model, to dynamically interpolate information in space and time.

Masina et al. (2001) use an univariate optimal interpolation method (developed by Derber and Rosati (1989)) associated with a relatively high-resolution primitive equation global ocean circulation model, assimilating both temperature profiles and satellite altimeter data. Satellite altimeter observations are transformed into "synthetic" temperatures by applying a statistical method by Mellor and Ezer (1991). Using Masina et al. (2001) approach, an attempt is done to elaborate a method relating vertical speed (difficult to detect and measure) during upwelling events with surface heat flux: a new upwelling speed can thus be introduced as

$$w_{syn} = F H'_F + \overline{w}_E, \tag{3.9}$$

$$F = \frac{\overline{w'_E H'_F}}{\overline{H'^2_F}} = \frac{\sum_t (w_E^{(t)} - \overline{w}_E)(H_F^{(t)} - \overline{H}_F)}{var(H_F^{(t)} - \overline{H}_F)}, \tag{3.10}$$

where the subscript *syn* stands for "synthetic", w_E is the Ekman upwelling speed (Equation 3.4, $\overline{w}_E$ is the average), H_F is the surface heat flux ($\overline{H}_F$ is the average), and

$$w'_E = w_E^{(t)} - \overline{w}_E, \quad H'_F = H_F^{(t)} - \overline{H}_F.$$

The sum in (3.10) is computed using daily values for any grid point of the upwelling region, on a monthly basis; indeed, as Masina et al. (2001) suggest, the F term should not be fixed in time. The error for the Upwelling Synthetic Speed is computed following Mellor and Ezer (1991) as

$$\overline{w_{syn} w_{syn}} = F^2 \frac{1 - C^2}{C^2} \overline{H'^2_F}, \tag{3.11}$$

where

$$C(w^*_E, H^*_F) = \frac{\overline{w^*_E H^*_F}}{(\overline{w^{*2}_E H^{*2}_F})^{1/2}} \tag{3.12}$$

is the correlation coefficient between the nondimensional quantities

$$w^*_E = \frac{w_E - \overline{w}_E}{std(w_E)} \tag{3.13a}$$

$$H^*_F = \frac{H_F - \overline{H}_F}{std(H_F)}. \tag{3.13b}$$

3.4 Analysis of Coastal Upwelling Events

In the present section, we study some properties of wind-induced Coastal Upwelling events in the Mediterranean Sea from the perspective of the surface heat transfer, driven by the temperature difference between air and ocean at the interface. As explained in the previous sections, such thermal discrepancy is given by the upperward transport of cold water from the sea interior to the surface in the coastal region, due to the wind stress action at the open sea.

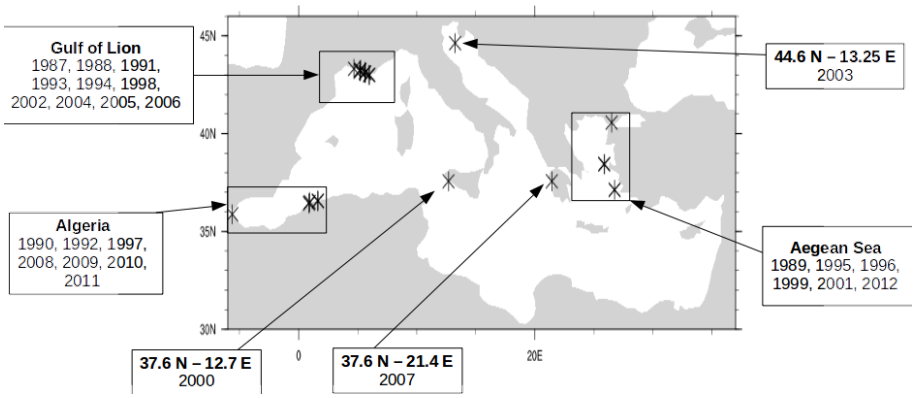

Figure 3.2: Spatial distribution of annual heat flux maxima in the Mediterranean Sea, during the MFS Reanalysis period (1987-2012).

In Figure 3.2 we show the spatial distribution on the heat flux maxima, computed on annual basis for the MFS Reanalysis period: it can be seen that the most intense upwelling zones are the Gulf of Lion coastline, the Aegean Sea subbasin along the Turkey shoreline, and off Algerian coast. This is coherent with what is said by Bakun and Agostini (2001) and resumed in Section 3.2.3. In the following, three different coastal areas will be characterized, namely:

1. the southern coast of Sicily (Section 3.4.1, Figure 3.3), posed on the left side of a predominantly northwesterly wind stress pattern, and influenced by the large mesoscale phenomena characterizing the Sicily Strait (Beranger et al. (2004); Askari (2001); Kostianoy et al. (1998));

2. the Gulf of Lion coastline near Marseille (Section 3.4.2,Figure 3.13), where Mistral and Tramontane winds cause strong upwelling episodes throughout the year (Johns et al. (1992); Millot and Wald (1981));

3. the Aegean Sea coastline (Section 3.4.3, Figure 3.23), where strong upwelling events occur in response to steady northerly winds (Savvidis et al. (2004); Stergiou et al. (1997)).

For each area, a single Coastal Upwelling event has been chosen, either the most intense (in terms of heat flux magnitude) or the most interesting in a geographical-location sense. Each event is then characterized through the analysis of the atmospheric forcing on the area, and the density structure (both horizontal and vertical); finally, the wind stress curl pattern is studied and different vertical velocitis are computed.

3.4.1 Sicily Upwelling

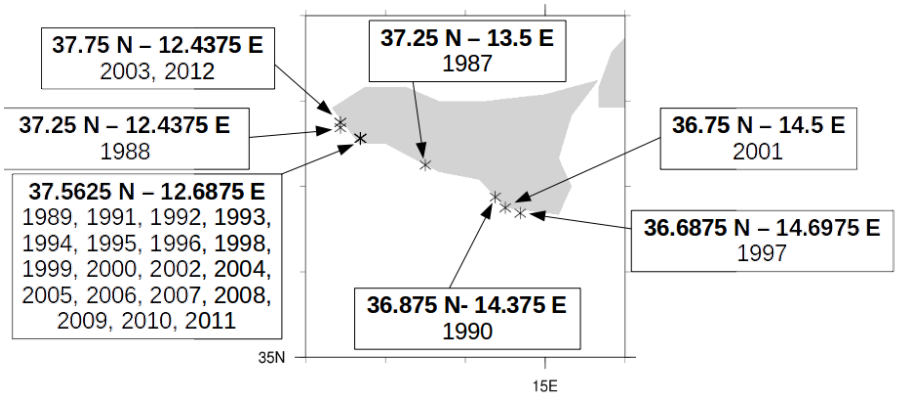

Figure 3.3: Spatial distribution of annual heat flux maxima in Sicily, during the MFS Reanalysis period (1987-2012).

Figure 3.3 shows the spatial distribution of heat flux miximum points in the Sicily area, which are mainly localized on the westernmost part of the island. The 2003 annual maximum has been selected from the MFS Reanalysis database; during this year, more precisely August 2nd, it is recorded the maximum value of downward heat flux (750 W m^{-2}) in the Sicily area, in the point of coordinates 37.7°N-12.4°E, near the westernmost corner of the Sicily island (Figure 3.4).

Atmospheric Forcing. Heat and water fluxes trends in the maximum point show a correlation equal to 0.14, not as good as the Gulf of Lion winter trends seen in the previous chapter (Figure 2.8 and Figure 2.13); this is likely due to a major contribution, during the Summer season, by the other heat balance components respect to the latent heat flux. At the beginning of the Coastal Upwelling event (late July) heat flux shows an abrupt increase, and a slower decrease in the early part of August; looking at the peak width, the event seems to last about 21 days, with an e-folding time of 9 days from August, 2nd. In the heat flux maximum point, we estimate a heat gain of 19.6 kW/m^2 for the time period ranging from June 15th to September 15th, 2003.

Figure 3.4: Google Maps screenshot on selected coastal box for Sicily case.

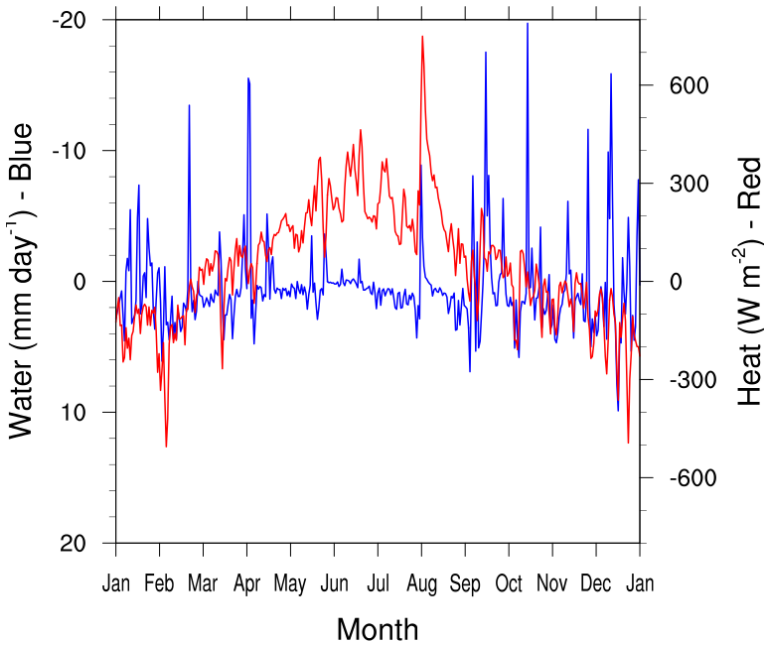

Figure 3.5: Heat (W/m^2, red line) and water (mm/day, blue line) fluxes in the 2003 year, computed at the heat flux maximum point in the Sicily area.

Density Structure. Figure 3.6 shows the 8-m depth density map for Sicily area during the most intense Summer upwelling event in 2003: a density increase is evident along the southern coast of the island, up to 2-3 kg m^{-3} close the coastline. The presence of a density surface front is confirmed by looking at the latitudinal slice in Figure 3.7: August 2nd slice, in particular, shows the outcropping of the 1027 kg m^{-3} at the coastline.

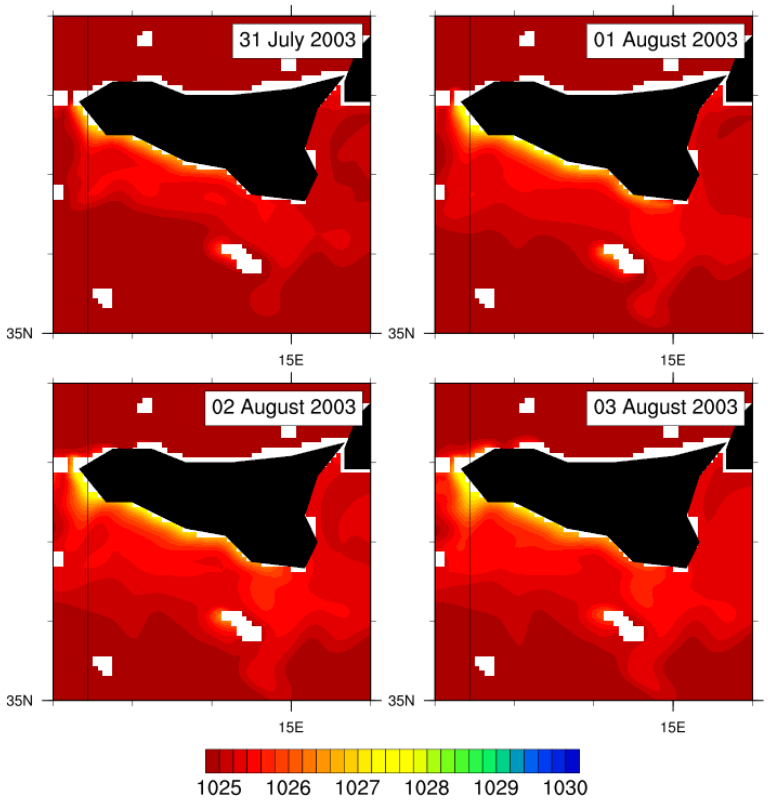

Figure 3.6: In-situ density (kg/m^3) at 8-m depth on Sicily area during the Summer upwelling event; black line shows slice location (Figure 3.7).

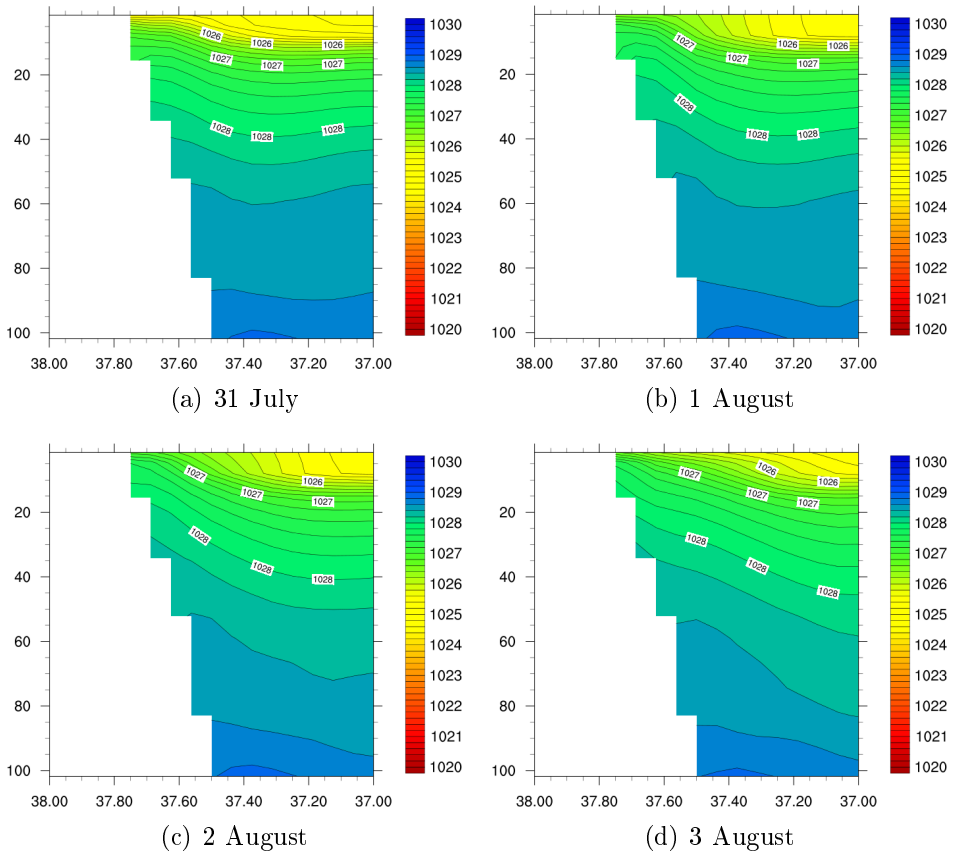

(a) 31 July (b) 1 August

(c) 2 August (d) 3 August

Figure 3.7: Latitudinal slice of in-situ density (kg/m^3) in the Sicily coastal area during the Summer upwelling event in 2003, in the location showed in Figure 3.6.

Sea Surface Height. Another important approach to detect intense upwelling is the sea surface height. Figure 3.8 shows the SSH relative to the most intense Summer upwelling event in Sicily (August 2nd, 2003), where the strongest (negative) anomaly is visible in the westernmost part of the island, up to values of 27 cm on the southern side.

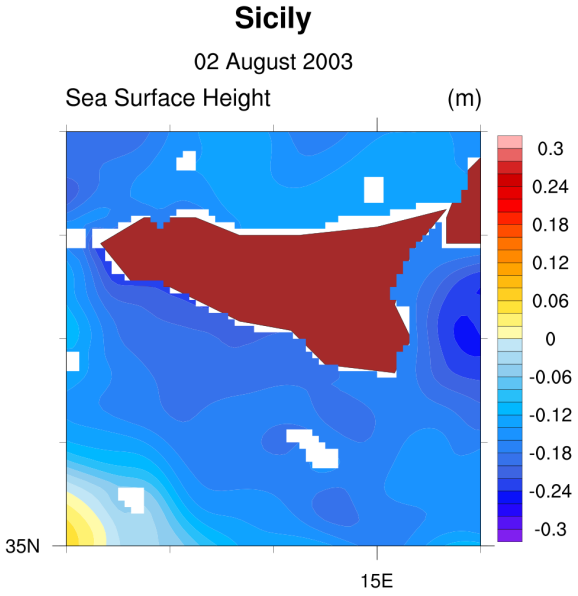

Figure 3.8: Sea surface height anomaly (m) on Sicily area during the heat flux maximum day in 2003.

Wind Stress Curl and Upwelling Speeds. Figure 3.9 displays the vertical component of the wind stress curl (10^{-5} N m^{-3}), superimposed with the wind stress itself, computed in the Sicily area during the most intense Summer upwelling event. In the early part of the period, a quite evident separation between positive (related to upward motion) and negative (related to downward motion) regions is clearly visible; then, a northward rotation in the wind direction causes a strong localization of upwelling forcing in the northernmost part of the southern coast of the island.

The Ekman Potential Speed, which retains only the wind stress contribution and computed using Equation (3.4), can be compared to the Continuity True Speed computed using the continuity equation (3.6). Figure 3.10 shows a comparison of both Ekman Potential Speed and Continuity True Speed for the most intense Summer upwelling event in Sicily: the former is smooth and regular, following the wind stress curl pattern and reaching a maximum value of 6×10^{-5} m s^{-1}; instead, the maximum Continuity True Speed in the area is one order of magnitude higher (up to 2×10^{-4} m s^{-1}) and its appearance is

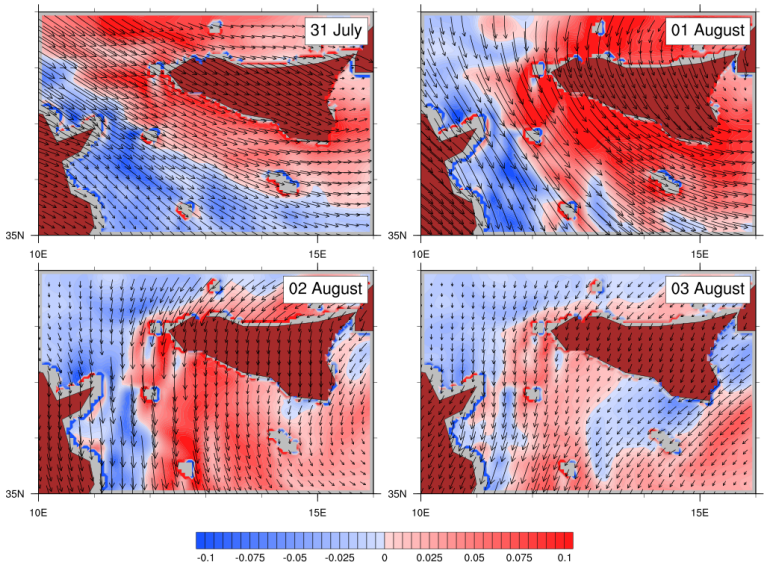

Figure 3.9: Comparison between the wind stress (N/m^2, vectors) and the vertical component of the wind stress curl (10^{-5} N/m^3, contours) on Sicily area during the Summer upwelling event.

far more patchy, being influenced from the mesoscale vortex structures of the Sicily Strait. Superimposition of surface current vectors with the Ekman speed presents a consistent picture of the phenomenon: surface currents move away from the Southern Sicily coast, corresponding to positive (upward) values of vertical speed; instead, in the northern side of Malta island, currents move toward the coast and induce negative (downward) motion. For what concerns the Continuity True Speed, the description is complicated by the presence of an intense mesoscale vortex activity, and it is difficult to relate this speed pattern with the surface current structure.

Using the method outlined in Section 3.3, the Upwelling Synthetic Speed is computed for the present case. Figure 3.11 shows a comparison between the three computed vertical velocities averaged on the Sicily coastal area for the year 2003 (Figure 3.4). During the 2003, the correlation between the Upwelling Synthetic Speed and the Ekman Potential Speed is 0.65, while with the Continuity True Speed is 0.43. The peak associated with the upwelling event is quite distinguishable in all vertical speeds. In Figure 3.12, it is shown in detail the spatial comparison between downward heat flux and vertical speeds for the day of maximum heat flux, only relative to the coastal box values. The Upwelling Synthetic Speed is more intense than the Continuity True Speed, but is capable to capture the velocity pattern near the heat flux maximum area. Nonetheless, near the coastline the Upwelling Syntethic Speed shows an irregular pattern; this is due to the numerical method used in the wind stress

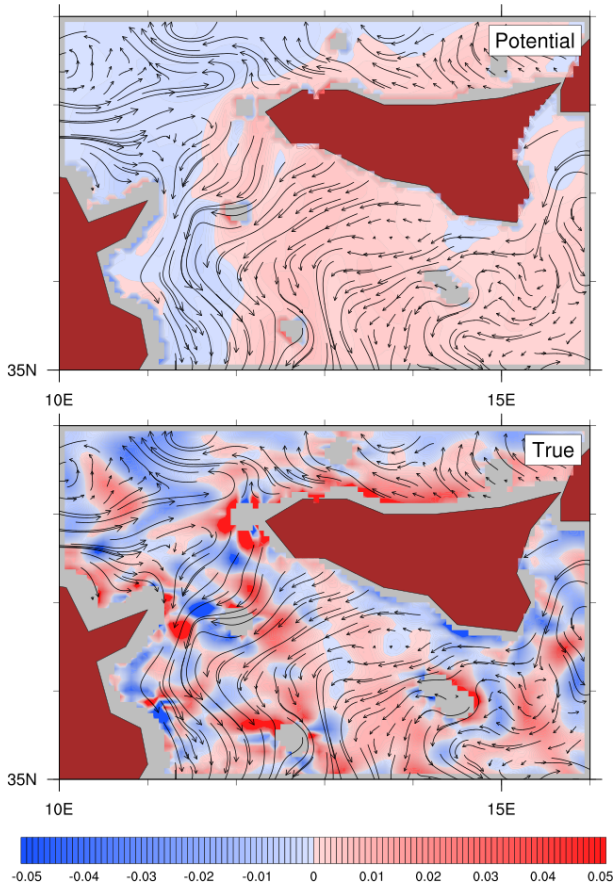

Figure 3.10: Comparison between the Ekman Potential speed (mm/s, panel top) and the Continuity True Speed (mm/s, panel bottom), superimposed with the surface current vectors, on Sicily area.

curl computation of (3.4), which fails at the coastal boundary.

3.4.2 Gulf of Lion Upwelling

Figure 3.13 displays the heat flux maximum points distribution in the Gulf of Lion area, concentrated close the French coastline near Marseille. The Gulf of Lion case study regards the 1998 year, when August 22nd daily heat flux experienced a heat gain of 867 W m^{-2}, that is the highest positive downward heat flux value in the MFS Reanalysis database. The maximum point is located at 43°N-6°E, near the city of Toulon (France), in the southernmost corner of the Gulf of Lion (Figure 3.14).

Atmospheric Forcing. Heat and water fluxes trends (Figure 3.15) show that the correlation between the two quantities is good in wintertime (thanks to the latent heat component), but in Summer it decreases because of the other heat balance components; the correlation coefficient is 0.36, on an annual basis.

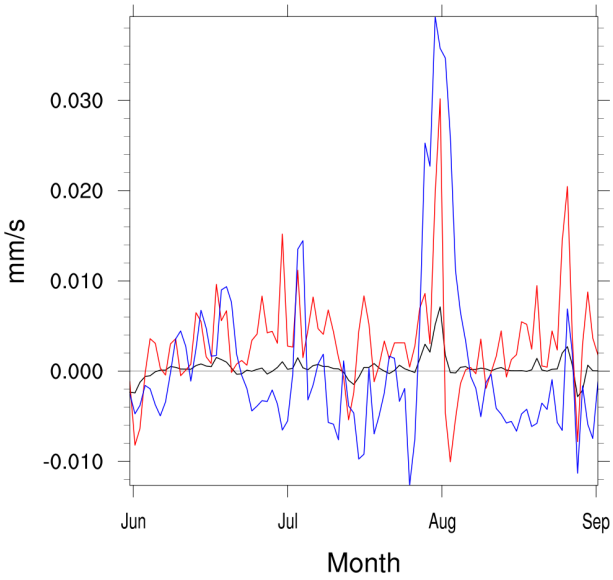

Figure 3.11: Comparison among the Ekman Potential Speed (mm/s, black line), the Continuity True Speed (mm/s, red line), and the Upwelling Synthetic Speed (mm/s, blue line) on the Sicily coastal area during the Summer upwelling event; a "learning period" of 30 days has been set.

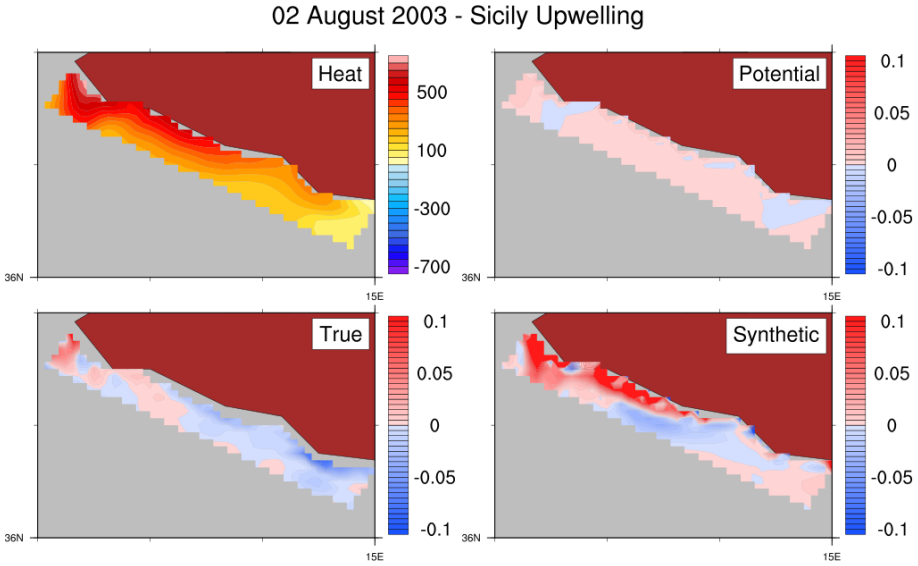

Figure 3.12: Comparison among the downward heat flux (W/m^2) and the vertical speeds (mm/s) on Sicily coastal area during the heat flux maximum day in 2003.

Heat flux is characterized by a single, distinguishable peak, during the second part of August and lasting about 8 days, with an e-folding time of 4 days from the maximum day. In the heat flux maximum point, we estimate a net heat gain of 24.1 kW/m^2 in the period June 15th - September 15th, 1998.

Density Structure. Figure 3.16 shows the 8-m depth density map for the Gulf of Lion area during the most intense Summer upwelling event in 1998:

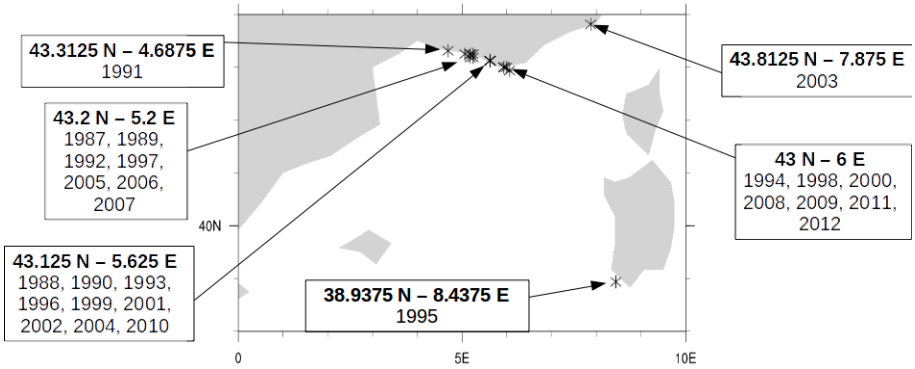

Figure 3.13: Spatial distribution of annual heat flux maxima in the Gulf of Lion area, during the MFS Reanalysis period (1987-2012).

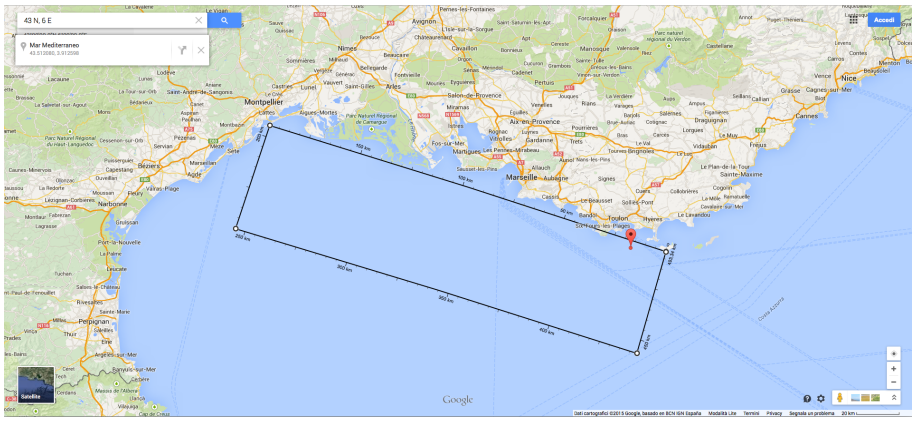

Figure 3.14: Google Maps screenshot on selected coastal box for Gulf of Lion case.

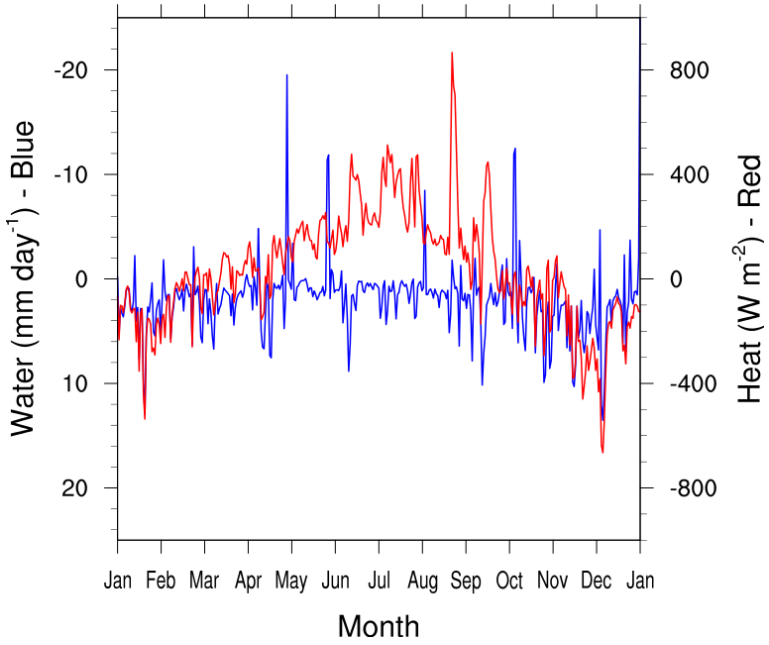

Figure 3.15: Heat (W/m^2, red line) and water (mm/day, blue line) fluxes in the 1998 year, computed at the heat flux maximum point in the Gulf of Lion area.

density increases evidently along the whole extension of the shoreline, with a maximum value of more than 1028 kg m^{-3}. More, the upwelling feature seems to extend offshore, forming a little filament which is a common characteristics of many upwelling zones in the World Ocean (Section 3.2). Longitudinal slice in

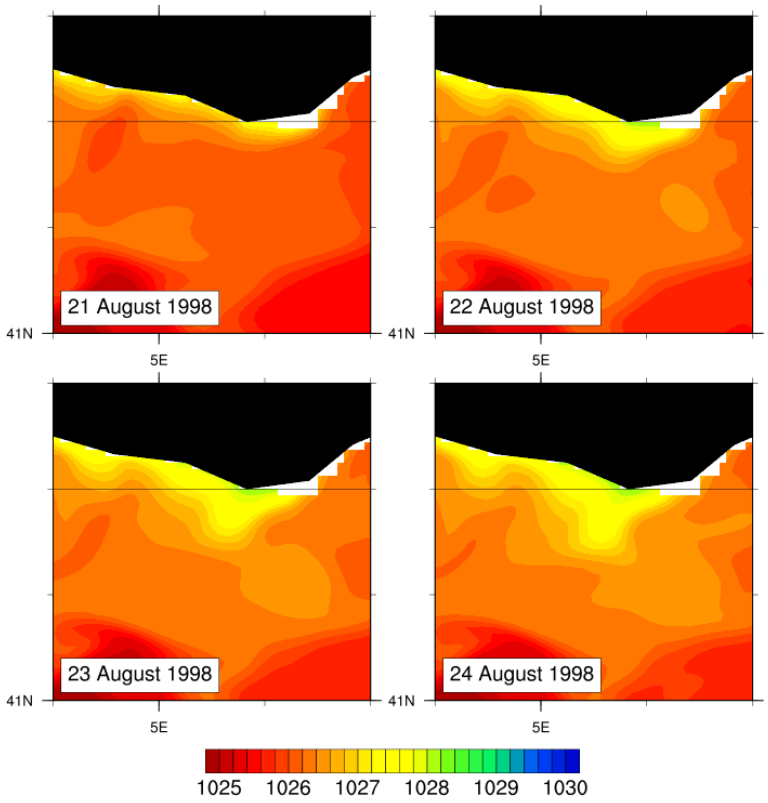

Figure 3.16: In-situ density (kg/m^3) at 8-m depth on the Gulf of Lion area during the Summer upwelling event; black line shows slice location (Figure 3.17).

Figure 3.17 shows an evident density front in the uppermost part of the water column, with the 1028.4 kg m^{-3} isoline passing from 55-m depth (August 21st) to about 20-m depth two days later. At the surface, it is visible the outcropping of 1028 kg m^{-3} isoline at the end of the most intense phase of the upwelling event.

Sea Surface Height. The sea surface height (Figure 3.18) exhibits a relative maximum value close to a cyclonic vortex in the middle of the gulf, clearly evident by the current vectors in Figure 3.20. Minimum values are found in proximity of the coastline, close to the upwelling zone, in corrispondence of the maximum of Continuity True Speed in the bottom panel of Figure 3.20.

Wind Stress Curl and Upwelling Speeds. As shown in Figure 3.19, the wind stress separate two distinct regions of the gulf with respect to the wind

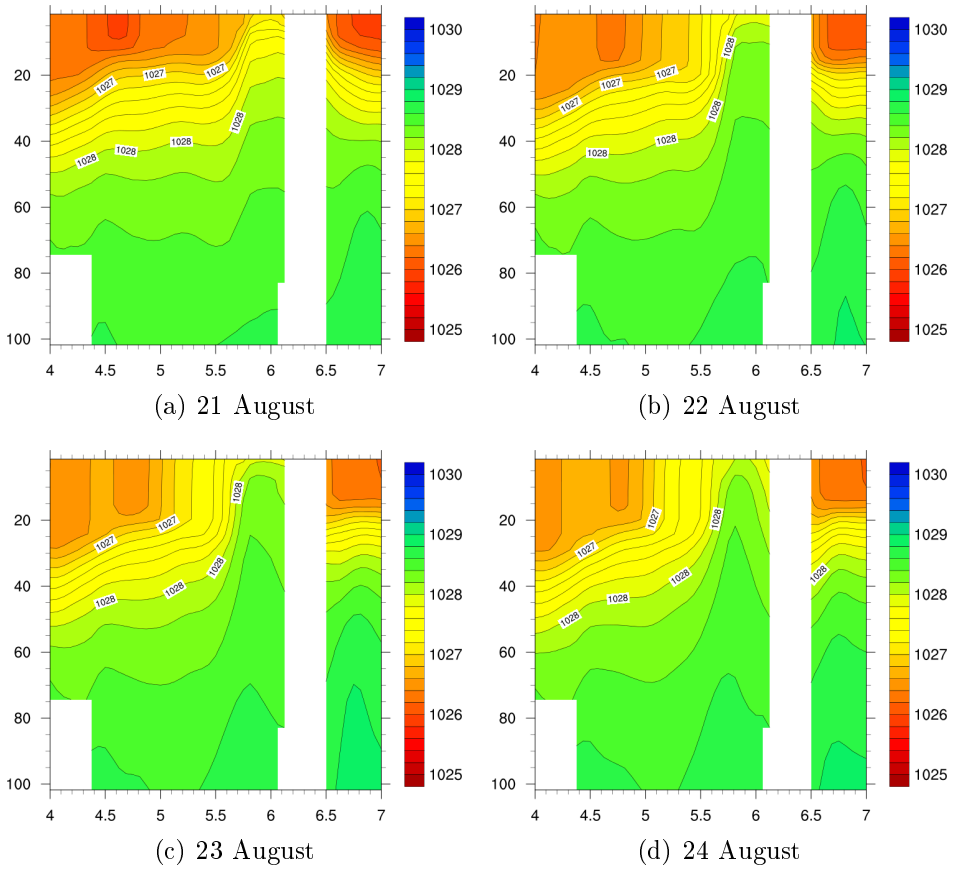

(a) 21 August (b) 22 August

(c) 23 August (d) 24 August

Figure 3.17: Longitudinal slice of in-situ density (kg/m^3) in the Gulf of Lion coastal area during the 1998 Summer upwelling event, in the location showed in Figure 3.16.

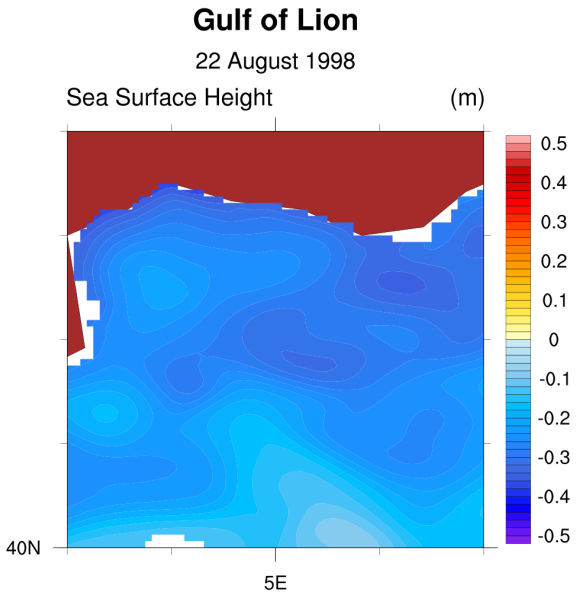

Figure 3.18: Sea surface height anomaly (m) on the Gulf of Lion area during the heat flux maximum day in 1998.

direction: the left side is characterized by high positive values of wind stress curl and upward motion, while in the other side of the Gulf of Lion there is downward motion.

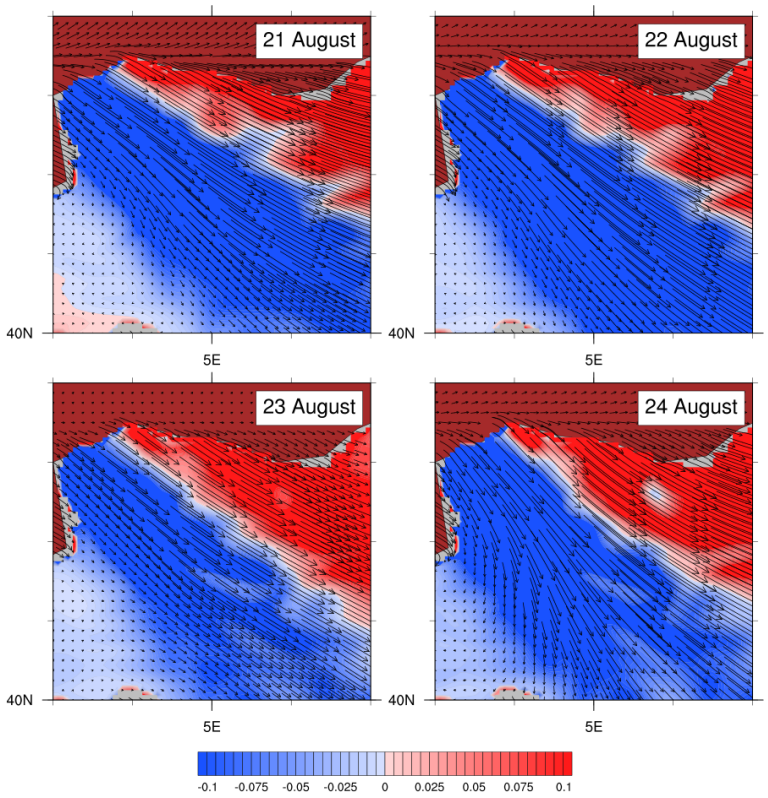

Figure 3.19: Comparison between the wind stress (N/m^2, vectors) and the vertical component of the wind stress curl (10^{-5} N/m^3, contours) on the Gulf of Lion area during the 1998 Summer upwelling event.

The comparison between Ekman and Continuity vertical speeds with surface currents (Figure 3.20) displays the presence of some permanent eddies structure, in the lee of predominant wind stress direction. Ekman Potential Speed is smaller and smoother in the whole area, with positive values close to the shoreline, where surface currents are directed perpendicular and away from the coastline; instead, the Continuity True Speed is more irregular, exhibiting the highest values on the coastline and the smallest in correspondence to the big anticyclonic vortex in the middle of the gulf, visible also in Figure 3.18 as a SSH relative maximum.

The comparison among the different vertical speeds in Figure 3.21 displays a rather irregular structure of the Continuity and the Synthetic vertical speeds; nonetheless, maxima trends are similar, as for the main one in early August. The Upwelling Synthetic Speed shows a correlation of 0.64 with the Ekman Potential Speed and of 0.42 with the Continuity True Speed. The spatial pat-

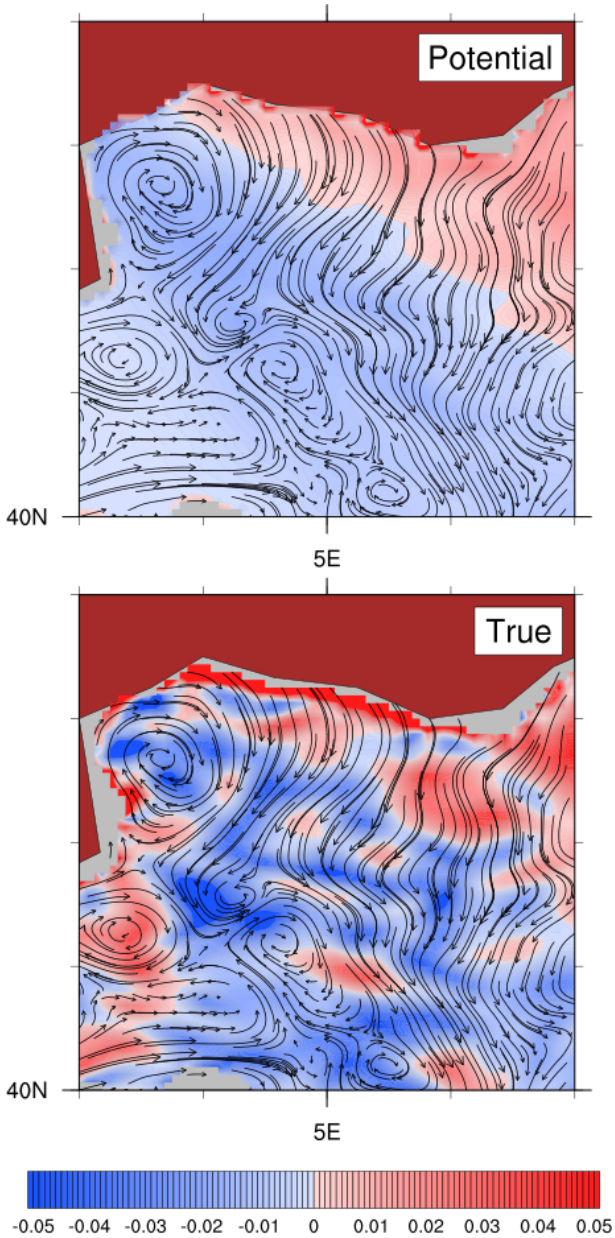

Figure 3.20: Comparison between the Ekman potential vertical speed (mm/s, panel top) and the Continuity vertical speed (mm/s, panel bottom), superimposed with the surface current vectors, on the Gulf of Lion area.

terns of August 22nd downward heat flux and vertical speeds are shown in Figure 3.22, relative to the coastal box area in Figure 3.14. Apart from the features closest the coastline, influenced by the computation of wind stress curl in w_E, the Upwelling Synthetic Speed shows a pattern similar to the Continuity True Speed.

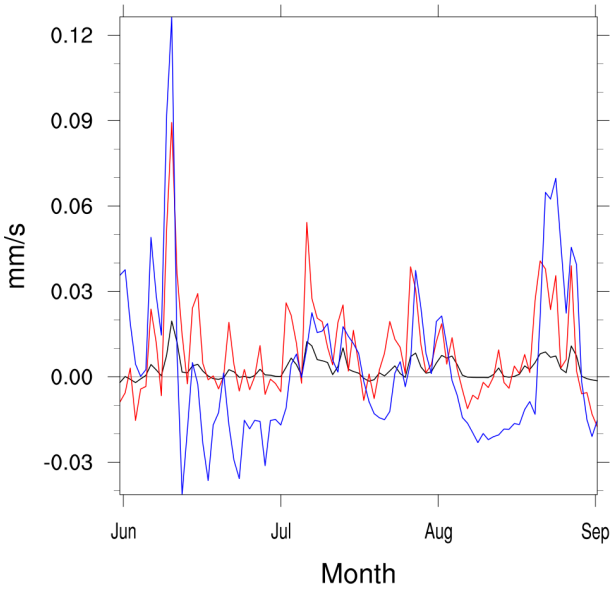

Figure 3.21: Comparison among the Ekman Potential Speed (mm/s, black line), the Continuity True Speed (mm/s, red line), and the Upwelling Synthetic Speed (mm/s, blue line) on the Gulf of Lion coastal area during the Summer upwelling event.

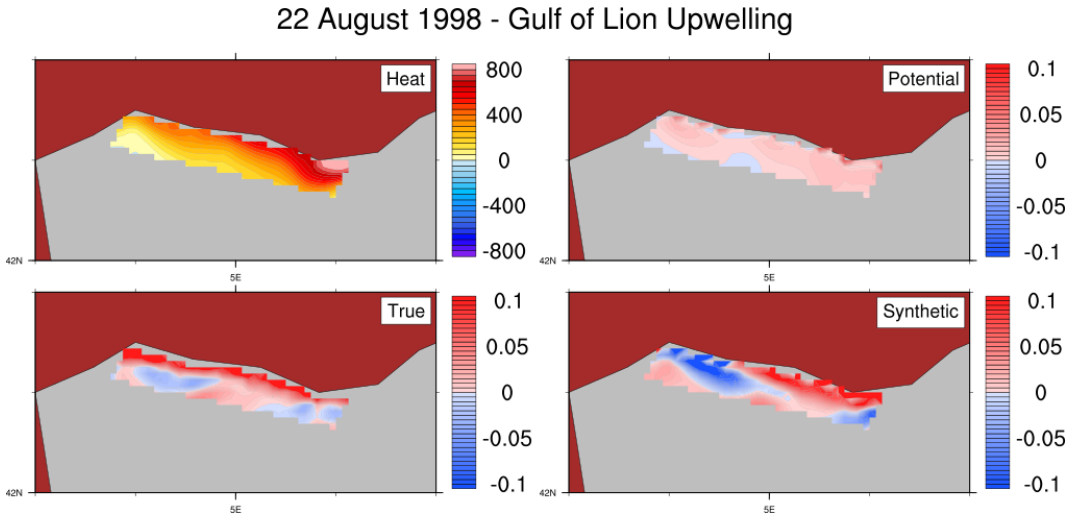

Figure 3.22: Comparison among the downward heat flux (W/m^2) and the vertical speeds (mm/s) on the Gulf of Lion coastal area during the heat flux maximum day in 1998; a "learning period" of 30 days has been set.

3.4.3 Aegean Sea Upwelling

The spatial distribution of heat flux maxima points in the Aegean Sea is concentrated along the Turkish coast (Figure 3.23); the major one is found during year 1998 close to the Gelibolu peninsula (Turkey, Northern Aegean Sea), but we choose to not use it because of its particular location. Instead, the 2001 maximum point has been selected, being located along the coastline of Chios island (Greece, Central Aegean Sea, Figure 3.24), in a good position to study Coastal Upwelling phenomenon and less sensible to model topography. The

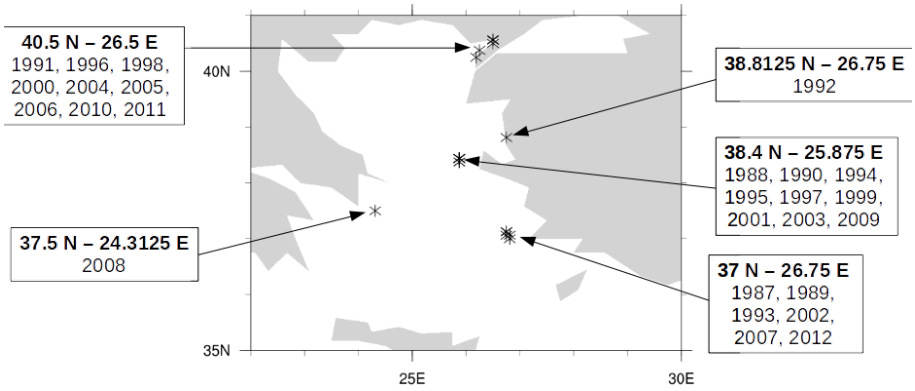

Figure 3.23: Spatial distribution of annual heat flux maxima in the Aegean Sea, during the MFS Reanalysis period (1987-2012).

maximum value of downward heat flux (801 W m^{-2}) is found on July, 31st.

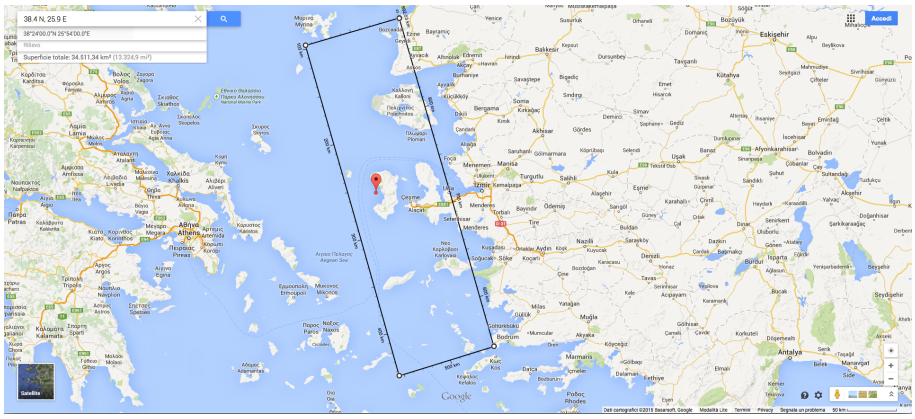

Figure 3.24: Google Maps screenshot on selected coastal box for Aegean Sea case.

Atmospheric Forcing. In Figure 3.25 heat and water fluxes are compared: in this case, trends show a correlation of 0.38. Looking at the heat flux peak width, this Coastal Upwelling event lasts for about 27 days and exhibits an e-folding time of 7 days from July, 31st. At the maximum heat flux point, it is estimated a net heat gain of 35.8 kW/m^2.

Density Structure. The 8-m depth density map in Figure 3.26 shows patterns which are strongly influenced by the complex coastal topography of the region More, the water inflow from the Black Sea creates an evident density discontinuity and separates the whole Aegean basin in two distinct part. Furthermore, the Coastal Upwelling process partecipates to accentuate this front, as we can see in Figure 3.27, where 1028 kg m^{-3} isoline outcrops and a 3.5 kg m^{-3} front is formed in the channel.

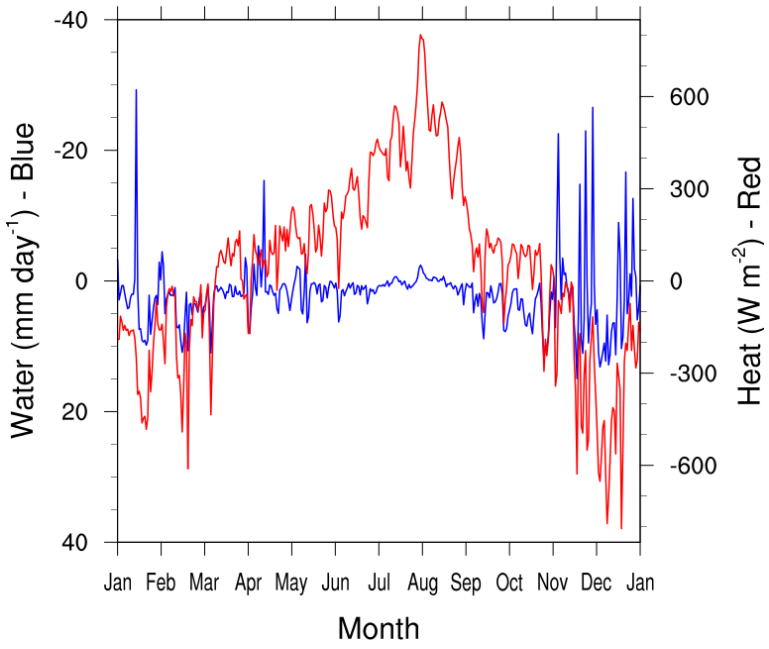

Figure 3.25: Heat (W/m^2, red line) and water (mm/day, blue line) fluxes trends in 2001, computed at the heat flux maximum point in the Aegean Sea area.

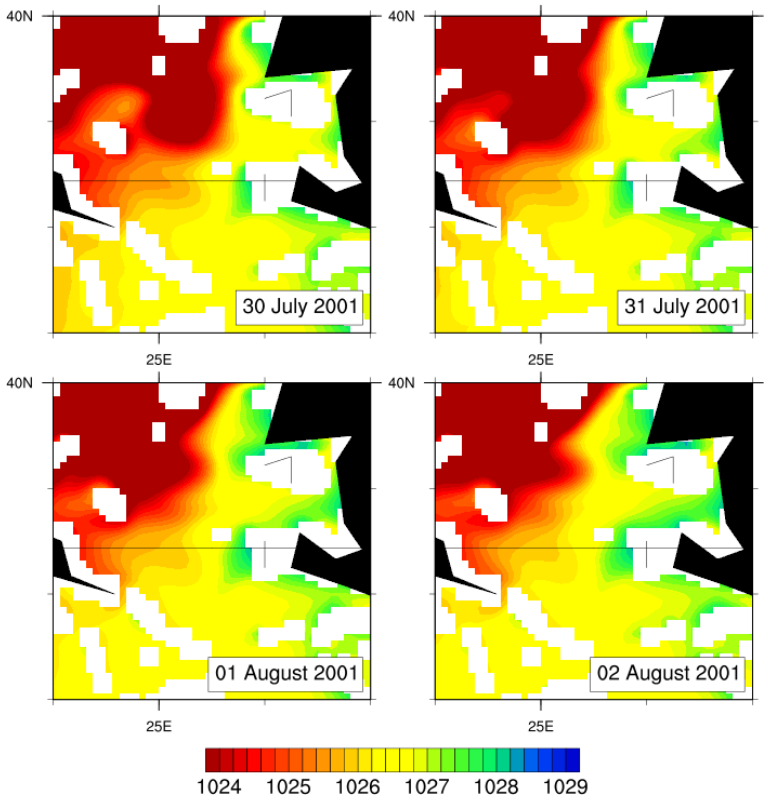

Figure 3.26: In-situ density (kg/m^3) at 8-m depth on the Aegean Sea area during the 2001 Summer upwelling event; black line shows slice location (Figure 3.27).

Sea Surface Height. Sea surface height (Figure 3.28) experienced the maxima negative values around the Lesvos island (close to the Turkey shore), and

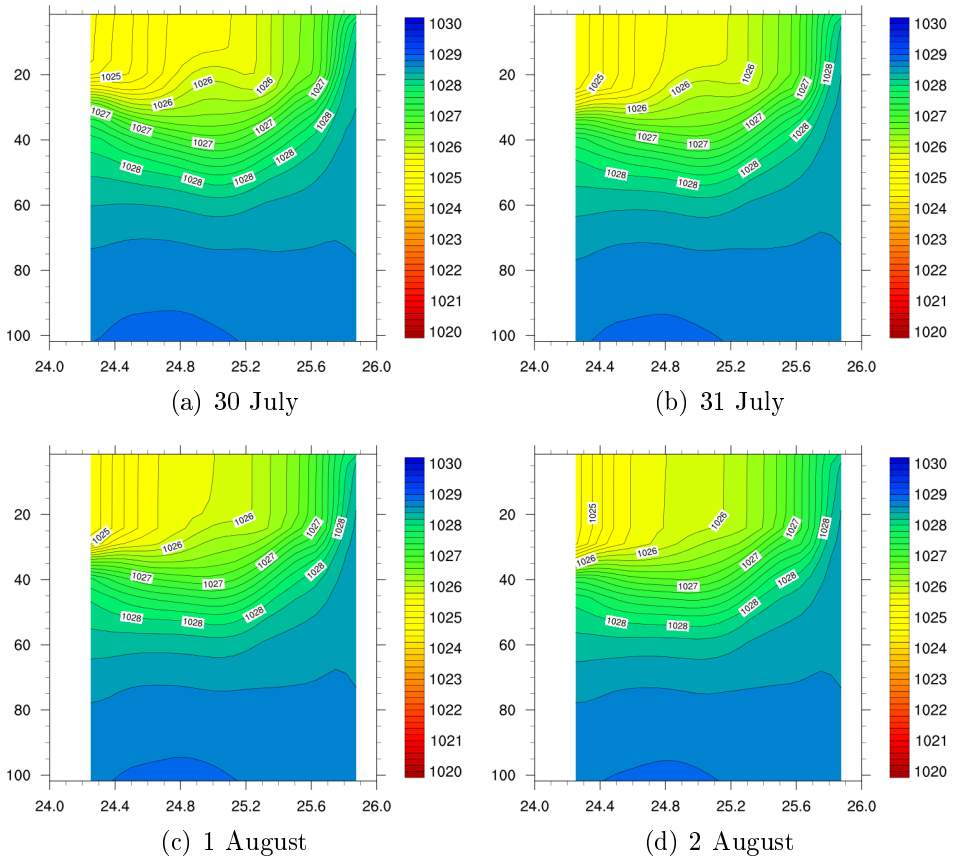

(a) 30 July (b) 31 July

(c) 1 August (d) 2 August

Figure 3.27: Longitudinal slice of in-situ density (kg/m^3) in the Aegean Sea coastal area during the 2001 Summer upwelling event, in the location showed in Figure 3.26.

seems to be more influenced by the coastal topography than by the upwelling process. Nevertheless, some SSH features can be related to surface current vectors in Figure 3.30.

Wind Stress Curl and Upwelling Speeds. Figure 3.29 shows that wind stress during this Summer upwelling event is near-parallel to the coast, subdividing the Aegean Sea in a positive wind stress curl (i.e. upward speed) region on the Turkish side, and a negative wind stress curl (i.e. downward speed) region on the Greek side. Surface current pattern is highly distorted by the coastal topography, making difficult to compare it with upwelling velocity (Figure 3.30); nevertheless, both Ekman and Continuity vertical speeds show a good mutual resemblance, positive on the Turkish side and negative on the Greek side of the Aegean basin.

Having imposed a large coastal box to account for the coastal topography (Figure 3.24), averaged Ekman Potential Speed shows very little values throughout the year; in our opinion, this is due to a near-complete compensation of pos-

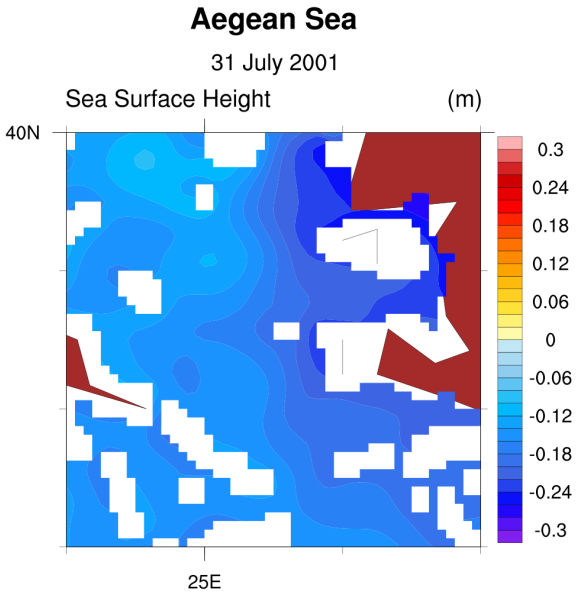

Figure 3.28: Sea surface height anomaly (m) on the Aegean Sea area during the heat flux maximum day in 2001.

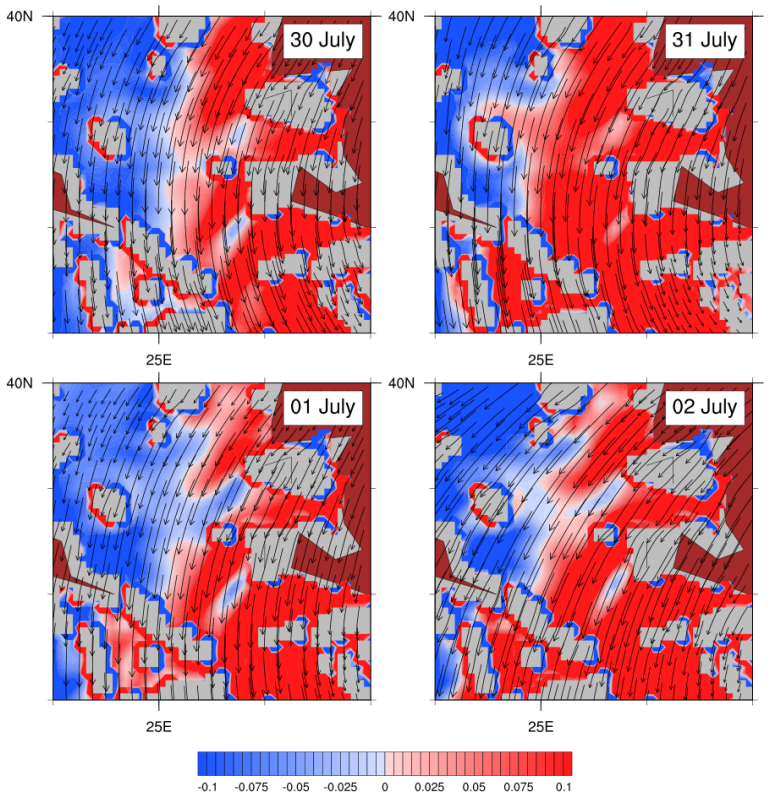

Figure 3.29: Comparison between the wind stress (N/m^2, vectors) and the vertical component of the wind stress curl ($10^{-5}N/m^3$, contours) on the Aegean Sea area during the 2001 Summer upwelling event.

itive and negative values in the averaging process. Instead, Continuity and Synthetic vertical speeds exhibit a correlation of 0.49, and seem to interpret

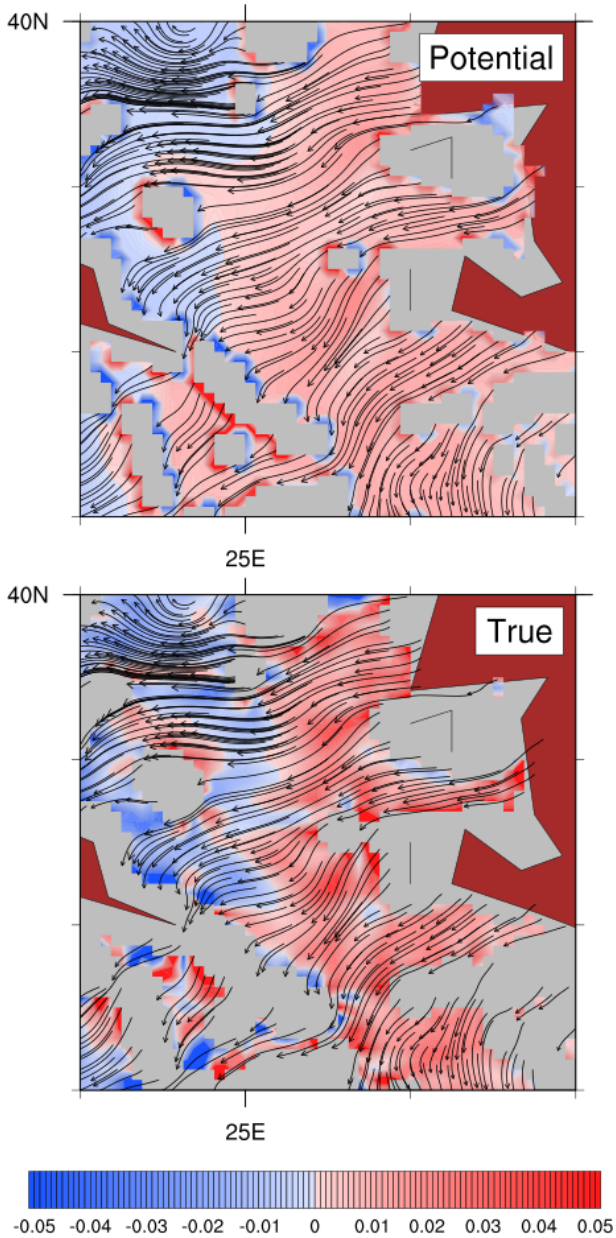

Figure 3.30: Comparison between the Ekman Potential Speed (mm/s, panel top) and the Continuity True Speed (mm/s, panel bottom), superimposed with the surface current vectors, on the Aegean Sea area.

well the upwelling event maximum (Figure 3.31), despite a three-factor difference. In Figure 3.32 we show the comparison among the downward heat flux and the vertical velocities: Ekman and Synthetic vertical speeds exhibit a high variability, due to the presence of complex coastal features.

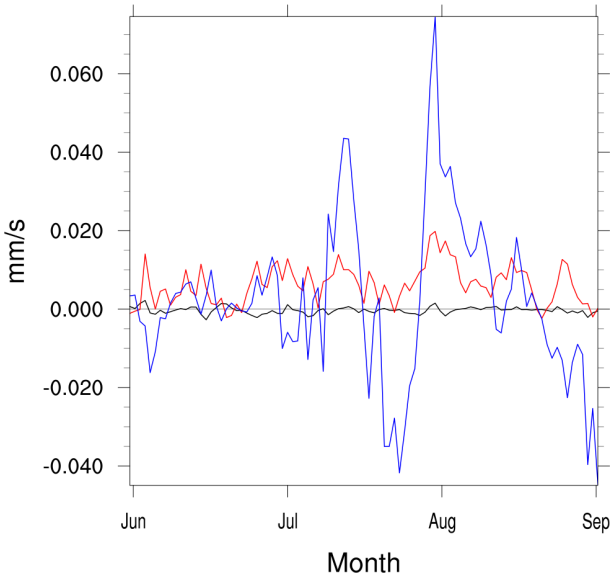

Figure 3.31: Comparison among the Ekman Potential Speed (mm/s, black line), the Continuity True Speed (mm/s, red line), and the Upwelling Synthetic Speed (mm/s, blue line) on the Aegean Sea coastal area during the Summer upwelling event.

3.5 Upwelling Predictions

The Upwelling Index introduced in Section 3.3 is used to predict the Coastal Upwelling events already described in Section 3.4. Setting a "learning period" preceding the start of the event, the Correlation Factor (3.10) is calculated and used to compute the Upwelling Synthetic Speed w_{syn} (Equation 3.9) for the next seven and fifteen days. This vertical speed is compared with the Continuity True Speed w_m (Equation 3.6) through a prediction error e, given by

$$e = \frac{std(w_m - w_{syn})}{std(w_m)}. \tag{3.14}$$

Three different learning periods have been tested, namely 30 days, 15 days, and 7 days, after the beginning of the upwelling event: August 20th for the Gulf of Lion case in 1998, July 27th for the Aegean Sea case in 2001, July 27th for the Sicily case in 2003.

Results are shown in Figure 3.33, Figure 3.34, and Figure 3.35. In the Gulf of Lion and Sicily cases, we can see that the 30-days learning period presents the higher values of prediction error, compared with the 15-days and 7-days periods; this is because the 30-days statistics comprise more unrelated features in the computation of F factor. Anyway, e values for all three periods remain under 4.0. Instead, in the Aegean Sea case all three learning periods exhibit a comparable error, ranging between 0.6 and 1.2.

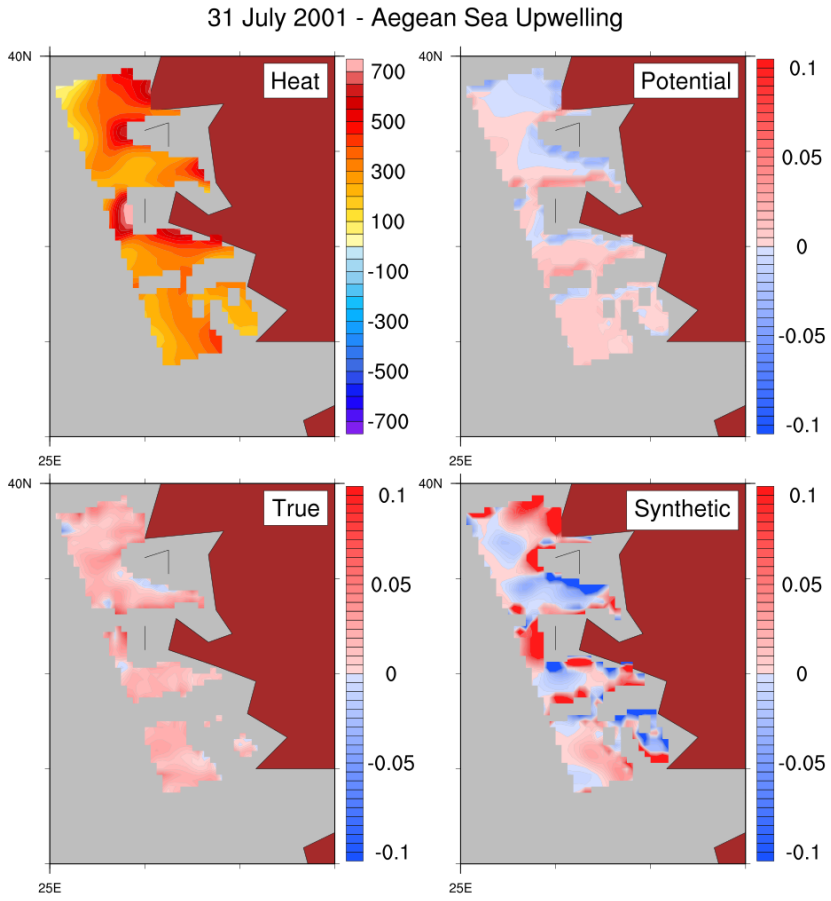

Figure 3.32: Comparison among the downward heat flux (W/m^2) and the vertical speeds (mm/s) on the Aegean Sea area during the heat flux maximum day in 2001; a "learning period" of 30 days has been set.

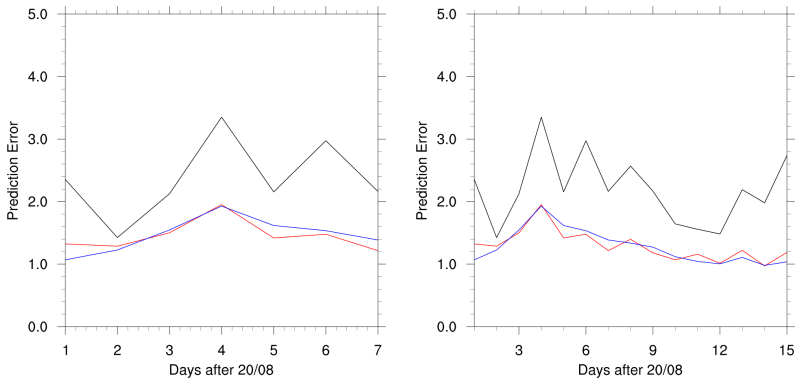

(a) 7 Days (b) 15 Days

Figure 3.33: Prediction error trends for the 1998 Gulf of Lion Coastal Upwelling event; black lines stand for a 30-days learning period, red lines for a 15-days learning period, and blue lines for a 7-days learing period.

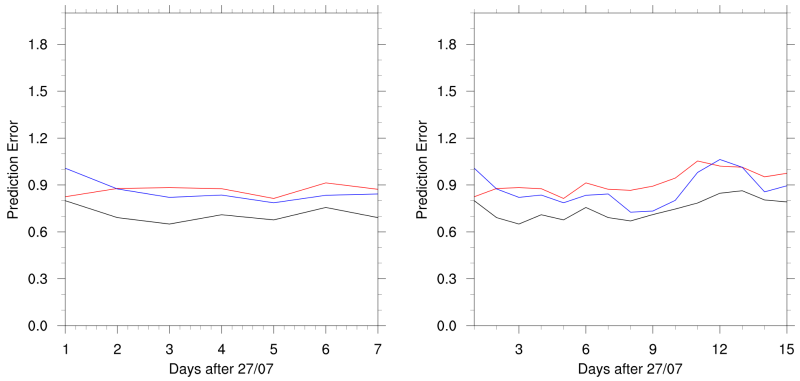

(a) 7 Days (b) 15 Days

Figure 3.34: Prediction error trends for the 2001 Aegean Sea Coastal Upwelling event; black lines stand for a 30-days learning period, red lines for a 15-days learning period, and blue lines for a 7-days learing period.

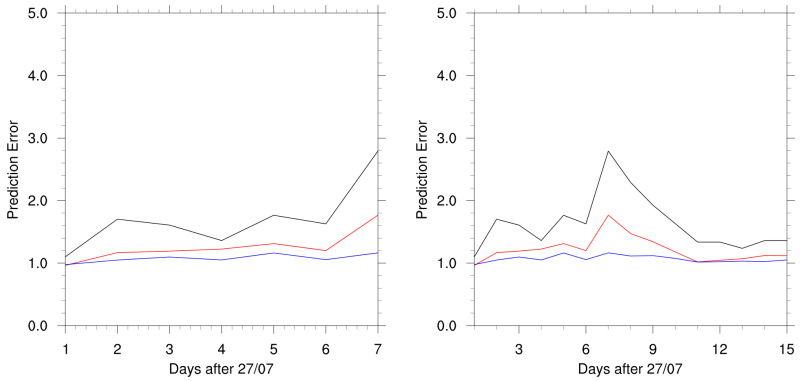

(a) 7 Days (b) 15 Days

Figure 3.35: Prediction error trends for the 2003 Sicily Coastal Upwelling event; black lines stand for a 30-days learning period, red lines for a 15-days learning period, and blue lines for a 7-days learing period.

3.6 Analysis of 2001 Aegean Sea Upwelling Event with Simulation

MFS Reanalysis database does not contain heat balance components, apart from shortwave radiation. In order to evaluate contributions from the other components on Coastal Upwelling process, a numerical simulation has been performed on Summer 2001 Aegean Sea event using the configuration of the model described in Oddo et al. (2009) and in Section 1.2.2. Figure 3.36 shows an overview of downward heat flux and its components. During Summer season, the main component in terms of contribution is the shortwave radiation one, but the other parts of the balance (the sensible heat flux, overall) seem to induce the maximum heat flux (up to 449 W m^{-2}) visible on early August.

Therefore, we can affirm that heat flux maximum during Coastal Upwelling event is primarly driven by the sensible heat flux.

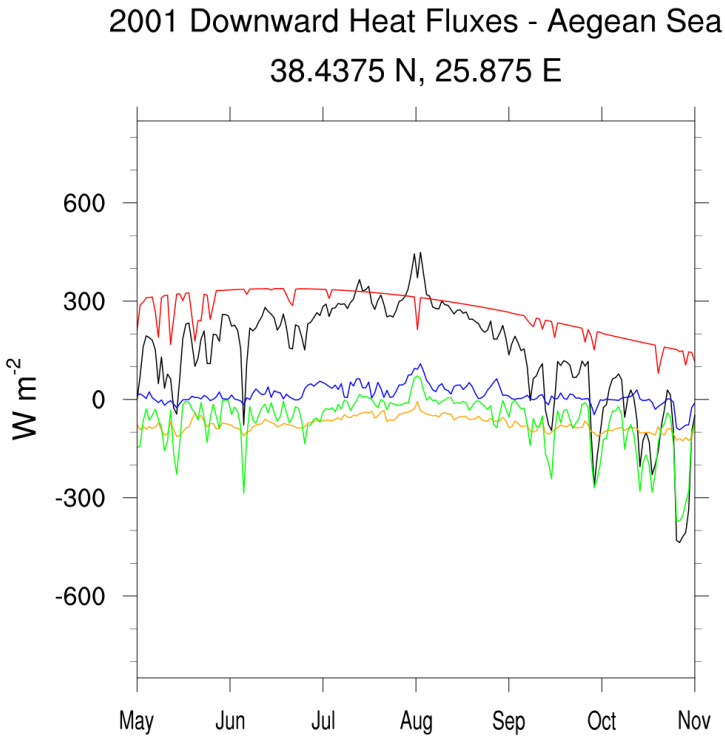

Figure 3.36: Downward heat flux (black line), with shortwave radiation (red line), longwave radiation (orange line), sensible heat flux (blue line), and latent heat flux (green line) simulated trends in 2001, computed on the heat flux maximum point in the Aegean Sea area.

Chapter 4

Conclusions and Outlooks

In this thesis, the MFS Reanalysis data have been used to characterize the Water Mass Formation and the Coastal Upwelling phenomena in the Mediterranean Sea. Numerical simulations have been performed to study some extreme episodes, involving large air-sea heat and momentum fluxes.

MFS Reanalysis database contains a realistic representation of the Water Mass Formation (WMF) processes, reproducing all the main characteristics of the phenomenon. WMF rates evaluated in Section 2.2 in the period 1987-2012 for the Gulf of Lion area correspond well to the major Water Mass Formation events found in the literature (e.g. Pinardi et al. (2013)). We considered the 2004/2005 and 2005/2006 WMF events, having comparable WMF rates (Figure 2.7), but being characterized by different atmospheric forcings (Figure 2.8, Figure 2.13) and different extension (Figure 2.9, Figure 2.14), both temporal and spatial. These events are well documented by measurements (e.g. Smith et al. (2008)), so we could validate our analysis. Density structures are consistent to what expected, in terms of eroded stratification and subsequent homogenization of the water column during the WMF event. ARGO float observations have been used to support our conjectures. Relying on Marshall and Schott (1999), we computed the dimensionless "Marshall Numbers" (introduced in Section 2.1.1) for both cases, confirming that open-ocean convection in the Gulf of Lion is a fully-turbulent, three-dimensional process.
For what concerns WMF simulations, two different configurations have been used: the first contains the usual model configuration (Section 1.2.2), whilst the second does not consider the surface latent heat flux forcing. It is clear to argue that the WMF rate (Figure 2.20), the density patterns (Figure 2.23, Figure 2.29), and the stratification (e.g. Figure 2.26, Figure 2.32) are driven by latent heat fluxes.

The characterization of Coastal Upwelling episodes shows that they corresponds to maximum positive surface heat gain in different well-known Coastal Upwelling areas (namely Sicily, Gulf of Lion, and Aegean Sea) in the Mediterranean Sea. The main properties of single events have been studied in terms of wind stress curl and vertical velocities. The important result of this study is the formulation of a new Upwelling Index based on the correlation between the surface heat flux and the vertical velocity, using Masina et al. (2001) approach (Section 3.3). This allows to diagnose a Coastal Upwelling event only knowing heat flux and wind stress forcing at the surface, easier quantities to compute than vertical velocity from the continuity equation. This index has been tested to predict known upwelling events, trying different "learning" and predicting periods (Section 3.5). From Coastal Upwelling simulations, it was shown that, apart from the shortwave component influence on summer heat exchange, the most important contribution to surface heat gain is the sensible heat flux.

Summarizing, our conclusions are:

1. WMF events are triggered by intense (at least 500 W/m^2) heat losses, occurring during the winter months, with air-sea latent heat flux as driving component;

2. nondimensional numbers from Marshall and Schott (1999) indicate that WMF processes in the Gulf of Lion have a three-dimensional structure, with flow characterized by a fully-turbulent regime;

3. Coastal Upwelling phenomena in the Mediterranean Sea exhibit a large variety of spatial and temporal extext, and are related to intense air-sea heat exchanges (up to 800 W/m^2) driven primarly by sensible heat flux;

4. it is possible to relate the surface heat gain with the vertical velocity intensity in the water column, thus estimating an upwelling index that could be used both to characterize and to predict upwelling events.

For what concerns the study of WMF process, next steps could be (1) the inclusion of heat balance components in the MFS Reanalysis database, and (2) the implementation of a local model in the Gulf of Lion at higher resolution, in order to capture the essential properties of the convective plumes. On the other hand, future efforts on Mediterranean Coastal Upwelling could be directed to the improvement of the new Upwelling Index, with a systematic application to other upwelling events and different areas.

Appendix A

MFS Model Density Function

As an indicator for occurring Water Mass Formation process and to analyze properties of Coastal Upwelling events, in-situ density has been computed from potential temperature θ, pressure p, and salinity S, taken from the MFS Reanalysis database. Several empirical density functions can be introduced. We chose to use the Mediterranean Forecasting System model density function, namely the Jackett and McDougall (1995) formula

$$\rho(S,T,p) = \frac{\rho(s,T,0)}{1 - p/K(S,T,p)}, \tag{A.1}$$

where $\rho(S,T,0)$ is a 15-term equation in powers of salinity S and in-situ temperature T (Table A.1), and $K(S,T,p)$ is a 26-term equation in powers of S, T, and pressure p (Table A.2).

Table A.1: Coefficients used in Equation (A.1) to compute $\rho(S,T,0)$. See also Millero and Poisson (1981) and Bigg (1967).

$\rho(S,T,0)$ terms	$\rho(S,T,0)$ coefficients
constant	9.998425×10^{2}
T	6.793952×10^{-2}
T^2	-9.095290×10^{-3}
T^3	1.001685×10^{-4}
T^4	-1.120083×10^{-6}
T^5	6.536336×10^{-9}
S	8.244930×10^{-1}
ST	-4.089900×10^{-3}
ST^2	7.643800×10^{-5}
ST^3	-8.246700×10^{-7}
ST^4	5.387500×10^{-9}
$S^{3/2}$	-5.724660×10^{-3}
$S^{3/2}T$	1.022270×10^{-4}
$S^{3/2}T^2$	-1.654600×10^{-6}
S^2	4.831400×10^{-4}

Table A.2: Coefficients used in Equation (A.1) to compute $K(S,T,p)$. See also Jackett and McDougall (1995).

$K(S,T,p)$ terms	$K(S,T,p)$ coefficients
constant	1.965221×10^{4}
T	1.484206×10^{2}
T^2	-2.327105×10^{0}
T^3	1.360477×10^{-2}
T^4	-5.155288×10^{-5}
S	5.46746×10^{1}
ST	-0.603459×10^{0}
ST^2	1.0987×10^{-2}
ST^3	-6.1670×10^{-5}
$S^{3/2}$	7.944×10^{-2}
$S^{3/2}T$	1.6483×10^{-2}
$S^{3/2}T^2$	-5.3009×10^{-4}
p	3.239908×10^{0}
pT	1.43713×10^{-3}
pT^2	1.16092×10^{-4}
pT^3	-5.77905×10^{-7}
pS	2.2838×10^{-3}
pST	-1.0981×10^{-5}
pST^2	-1.6078×10^{-6}
$pS^{3/2}$	1.91075×10^{-4}
p^2	8.50935×10^{-5}
p^2T	-6.12293×10^{-6}
p^2T^2	5.2787×10^{-8}
p^2S	-9.9348×10^{-7}
p^2ST	2.0816×10^{-8}
p^2ST^2	9.1697×10^{-10}

Bibliography

Adani, M., S. Dobricic, and N. Pinardi (2011). «Quality Assessment of a 1985–2007 Mediterranean Sea Reanalysis». In: *J. Atmos. Oceanic Technol.* 28, pp. 569–589. DOI: 10.1175/2010JTECHO798.1.

Anderson, D.L. and A.E. Gill (1975). «Spin-up of a stratified ocean, with applications to upwelling». In: *Deep Sea Research and Oceanographic Abstracts* 22.9, pp. 583–596.

Angstrom, A (1929). «On the variation of atmospheric radiation». In: *Beitrage zur Geophysik* 21, p. 145.

Artegiani, A. et al. (1997). «The Adriatic Sea General Circulation. Part I: Air–Sea Interactions and Water Mass Structure». In: *J. Phys. Oceanogr.* 27, pp. 1492–1514. DOI: 10.1175/1520-0485(1997)027<1492:TASGCP>2.0.CO;2.

Askari, F. (2001). «Multi-sensor remote sensing of eddy-induced upwelling in the southern coastal region of Sicily». In: *International Journal of Remote Sensing* 22.15, pp. 2899–2910.

Astraldi, M. et al. (1995). «Climatic fluctuations, current variability and marine species distribution - a case-study in the Ligurian sea (north-west Mediterranean)». In: *Oceanologica Acta* 18.2, pp. 139–149. URL: http://archimer.ifremer.fr/doc/00096/20768/.

Ayoub, N., P.Y. Le Traon, and P. De Mey (1998). «A description of the Mediterranean surface variable circulation from combined ERS-1 and TOPEX/POSEIDON altimetric data». In: *Journal of Marine Systems* 18.1, pp. 3–40.

Badan-Dangon, A., K.H. Brink, and R.L. Smith (1986). «On the dynamical structure of the midshelf water column off northwest Africa». In: *Continental Shelf Research* 5.6, pp. 629–644.

Bakun, A. (1996). *Patterns in the Ocean: Ocean Processes and Marine Population Dynamics*. University of California Sea Grant, San Diego (CA), USA, in cooperation with Centro de Investigaciones Biológicas de Noroeste, La Paz (Baja California Sur), Mexico.

Bakun, A. and V.N. Agostini (2001). «Seasonal Pettern of Wind-Induced Upwelling/Downwelling in the Mediterranean Sea». In: *Scientia Marina* 65.3, pp. 243–257.

Bang, N.D. (1973). «Characteristics of an intense ocean frontal system in the upwell regime west of Cape Town». In: *Tellus* 25, pp. 256–265.

Beranger, K. et al. (2004). «The dynamics of the Sicily Strait: a comprehensive study from observations and models». In: *Deep Sea Research Part II: Topical Studies in Oceanography* 51.4 (2004): 411-440.4, pp. 411–440.

Berliand, M.E. and T.G. Berliand (1952). «Determining the net longwave radiation of the earth with consideration of the effect of cloudiness». In: *Isv. Akad. Nauk. SSSR Ser. Geofis.* 1, pp. 64–78.

Bethoux, J.P. (1979). «Budgets of the Mediterranean Sea: their dependence on the local climate and on the characteristics of the Atlantic waters». In: *Ocean. Acta* 2, pp. 157–163.

Bethoux, J.P. et al. (2002). «Deep water in the western Mediterranean: peculiar 1999 and 2000 characteristics, shelf formation hypothesis, variability since 1970 and geochemical inferences». In: *Journal of Marine Systems* 33, pp. 117–131.

Bigg, P.H. (1967). «Density of water in SI units over the range 0-40 C». In: *British Journal of Applied Physics* 18.4, p. 521.

Bignami, F. et al. (1995). «Longwave radiation budget in the Mediterranean Sea». In: *J. Geophys. Res.* 100.C2, pp. 2501–2514.

Boubnov, B.M. and G.S. Golitsyn (1990). «Temperature and velocity field regimes of convective motions in a rotating plane fluid layer». In: *J. Fluid Mech.* 219, pp. 215–239.

Boukthir, M. and B. Barnier (2000). «Seasonal and inter-annual variations in the surface freshwater flux in the Mediterranean Sea from the ECMWF re-analysis project». In: *Journal of Marine Systems* 24.3, pp. 343–354.

Brink, K.H. (1983). «The Near-Surface Dynamics of Coastal Upwelling». In: *Progress in Oceanography* 12.3, pp. 223–257.

Brink, K.H., D. Halpern, and R.L. Smith (1980). «Circulation in the Peruvian upwelling system near 15°S». In: *J. Geophys. Res.* 85.C7, pp. 4036–4048. DOI: 10.1029/JC085iC07p04036.

Brink, K.H. et al. (1981). «Coastal Upwelling». In: ed. by F.A. Richards. American Geophysical Union, Washington DC, USA. Chap. Physical and Biological Structure and Variability in an Upwelling Center off Peru Near 15°S During March, 1977. DOI: 10.1029/CO001p0473.

Brunt, D. (1932). «Notes on radiation in the atmosphere». In: *Q.J.R. Meteorol. Soc.* 58, pp. 389–420. DOI: 10.1002/qj.49705824704.

Bryden, H.L., E. Brady, and R.D. Pillsbury (1989). «Flow through the Strait of Gibraltar». In: *Seminario sobre la Oceanografia Fisica del Estrecho de Gibraltar*. Ed. by J. Almazan et al., pp. 166–194.

Bryden, H.L., D. Halpern, and R.D. Pillsbury (1980). «Importance of eddy heat flux in a heat budget for Oregon coastal waters». In: *J. Geophys. Res.* 85.C11, pp. 6649–6653.

Budyko, M.I. (1963). *Atlas of Heat Balance*. 2nd Edition. Moscow Akad. Nauk. U.S.S.R.

Bunker, A.F. (1976). «Computations of surface energy flux and annual air-sea interaction cycles of the North Atlantic Ocean». In: *Mon. Wea. Rev.* 104, pp. 1122–1140.

Canals, M. et al. (2006). «Flushing submarine canyons». In: *Nature* 444, pp. 354–357.

Candela, J. (1991). «The Gibraltar Strait and its role in the dynamics of the Mediterranean Sea». In: *Dynamics of Atmospheres and Oceans* 15.3, pp. 267–299.

Castellari, S., N. Pinardi, and K. Leaman (1998). «A Model Study of Air-Sea Interactions in the Mediterranean Sea». In: *Journal of Marine Systems* 18, pp. 89–114.

— (2000). «Simulation of Water Mass Formation Processes in the Mediterranean Sea: influence of the time frequency of the atmospheric forcing». In: *Journal of Geophysical Research* 105, pp. 24157–24181.

Charney, J.G. (1955). «Generation of oceanic currents by wind». In: *J. Marine Res.* 14, pp. 477–498.

Coates, M.J. and G.N. Ivey (1997). «On convective turbulence and influence of rotation». In: *Dyn. Atmos. Oceans* 25, pp. 217–232.

Curtin, T.B. (1979). «Physical dynamics of the coastal upwelling frontal zone off Oregon». Ph.D. Dissertation. University of Miami.

Davey, M.K. and J.A. Whitehead (1981). «Rotating Rayleigh-Taylor instability as a model for sinking events in the ocean». In: *Geophys. Astrophys. Fluid Dyn.* 17, pp. 237–253.

Davis, R.E., R. DeSzoeke, and P. Niiler (1981). «Variability in the upper ocean during MILE. Part II: Modeling the mixed layer response». In: *Deep Sea Research Part A. Oceanographic Research Papers* 28.12, pp. 1453–1475.

Deardorff, J.W. (1968). «Dependence of air-sea transfer coefficients on bulk stability». In: *J. Geophys. Res.* 73, pp. 2549–2557.

Deardorff, J.W. (1985). «Mixed-layer entrainment: A review». In: *The Symposium in Turbulence and Diffusion*. Ed. by J.C. Weil, pp. 39–42.

Dee, D.P. et al. (2011). «The ERA-Interim reanalysis: configuration and performance of the data assimilation system». In: *Q.J.R. Meteorol. Soc., 137:* 137, pp. 553–597. DOI: 10.1002/qj.828.

Demirov, E. and N. Pinardi (2002). «Simulation of the Mediterranean Sea circulation from 1979 to 1993. Part I: The interannual variability». In: *Journal of Marine Systems* 33.34, pp. 23–50. URL: http://www.sciencedirect.com/science/article/pii/S0924796302000519.

Demirov, E.K. and N. Pinardi (2007). «On the Relationship between the Water Mass Pathways and Eddy Variability in the Western Mediterranean Sea». In: *Journal of Geophysical Research* 112.C2. DOI: 10.1029/2005JC003174.

Derber, J. and A. Rosati (1989). «A Global Oceanic Data Assimilation System». In: *J. Phys. Oceanogr.* 19, pp. 1333–1347. DOI: 10.1175/1520-0485(1989)019<1333:AGODAS>2.0.CO;2.

DeSzoeke, R.A. and J.G. Richman (1981). «The Role of Wind-Generated Mixing in Coastal Upwelling». In: *Journal of Physical Oceanography* 11.11, pp. 1534–1547.

Dewar, W.K. (1986). «Mixed layers in Gulf Stream rings». In: *Dynamics of atmospheres and oceans* 10.1, pp. 1–29.

Dillon, T.M. and D.R. Caldwell (1980). «The Batchelor spectrum and dissipation in the upper ocean». In: *J. Geophys. Res.* 85.C4, pp. 1910–1916. DOI: 10.1029/JC085iC04p01910.

Dobricic, S. and N. Pinardi (2008). «An oceanographic three-dimensional variational data assimilation scheme». In: *Ocean Modelling* 22.3, pp. 89–105.

Dobricic, S. et al. (2005). «Mediterranean Forecasting System: An improved assimilation scheme for sea-level anomaly and its validation». In: *Q.J.R. Meteorol. Soc.* 131, pp. 3627–3642. DOI: 10.1256/qj.05.100.

Dobricic, S. et al. (2006). «Daily oceanographic analyses by the Mediterranean basin scale assimilation system». In: *Ocean Science Discussions* 3.6, pp. 1977–1998.

Drévillon, M et al. (2008). «The GODAE/Mercator Ocean global ocean forecasting system: results, applications and prospects». In: *J. Operational Oceanogr.* 1.1, pp. 51–57.

Ekman, V.W. (1905). «On the influence of the earthś rotation on ocean currents». In: *Ark. Mat. Astron. Fys.* 2, pp. 1–53.

Emanuel, K. (1994). *Atmospheric Convection*. Oxford Univ. Press, New York (NY), USA.

Fekete, B.M., C.J. Vorosmarty, and W. Grabs (1999). *Global, composite runoff fields based on observed river discharge and simulated water balances*. URL: http://hdl.handle.net/10068/253915.

Fernando, H.J.S., R. Chen, and D.L. Boyer (1991). «Effects of rotation on convection turbulence». In: *J. Fluid. Mech.* 228, pp. 513–547.

Fuda, J.L. et al. (2000). «XBT monitoring of a meridian section across the western Mediterranean Sea». In: *Deep Sea Research Part I: Oceanographic Research Papers* 47.11, pp. 2191–2218.

Garrett, C., M. Bormans, and K. Thompson (1990). «Is the Exchange through the Strait of Gibraltar Maximal or Submaximal?» In: *The Physical Oceanography of Sea Straits*. Ed. by L.J. Pratt. Vol. 318. NATO ASI Series, pp. 271–294. DOI: 10.1007/978-94-009-0677-8_13.

Gertman, I.F., I.M. Ovchinnikov, and Y.I. Popov (1994). «Deep Convection in the Eastern Basin of the Mediterranean Sea». In: *Oceanology, 34:* 34, pp. 19–25.

Gill, A.E. and A.J. Clarke (1974). «Wind-induced upwelling, coastal currents and sea-level changes». In: *Deep Sea Research and Oceanographic Abstracts* 21.5, pp. 325–345.

Gleizon, P., G.C. Dhieres, and D. Renouard (1996). «Experimental study of the Alboran Sea gyres». In: *Oceanologica Acta* 19.5, pp. 499–511.

Gordon, A.L. (1982). «Weddell deep water variability». In: *J. Mar. Res.* 40, pp. 199–217.

Grilli, F. and N. Pinardi (1998). «The computation of Rossby radii of deformation for the Mediterranean Sea». In: *MTP news* 6.4.

GSP Group (1990). «Greenland Sea Project: A venture toward improved understanding of the oceans' role in climate». In: *EOS Transactions*.

Halpern, D. (1976). «Structure of a coastal upwelling event observed off Oregon during July 1973». In: *Deep Sea Research and Oceanographic Abstracts* 23.6, pp. 495–508.

— (1977). «Description of Wind and of Upper Ocean Current and Temperature Variations on the Continental Shelf off Northwest Africa during March and April 1974». In: *J. Phys. Oceanogr.* 7, pp. 422–430.

Hecht, A. (1992). «Abrupt changes in the characteristics of Atlantic and Levantine Intermediate Waters in the Southeastern Levantine Basin». In: *Oceanologica Acta* 15.1, pp. 25–42. URL: http://archimer.ifremer.fr/doc/00100/21158/.

Hecht, A., N. Pinardi, and A.R. Robinson (1988). «Currents, Water Masses, Eddies and Jets in the Mediterranean Levantine Basin». In: *J. Phys. Oceanogr.*

18, pp. 1320–1353. DOI: 10.1175/1520-0485(1988)018<1320:CWMEAJ>2.0.CO;2.

Hellerman, S. and M. Rosenstein (1983). «Normal Monthly Wind Stress over the World Ocean with Error Estimates». In: *Journal of Physical Oceanography* 13, pp. 1093–1104.

Herrmann, M. et al. (2010). «What induced the exceptional 2005 convection event in the northwestern mediterranean basin? Answers from a modeling study». In: *Journal of Geophysical Research* 115.C12. DOI: 10.1029/2010JC006162.

Hidaka, K. (1958). «Computation of the wind stresses over the oceans». In: *Rec. Oceanogr. Works Japan* 4.2, pp. 77–123.

Hogg, N. (1973). «The preconditioning phase of MEDOC 1969, II, Topographic effects». In: *Deep Sea Res.* 20, pp. 449–459.

Hoskins, B., M. McIntyre, and A. Robinson (1985). «On the use and significance of isentropic potential vorticity maps». In: *Q. J. R. Meteorol. Soc.* 111, pp. 877–946.

Howard, L.N. (1964). «Convection at high Reyleigh number». In: *Proc. Int. Congr. Appl. Mech., 11th*, pp. 405–432.

Jackett, D.R. and T.J. McDougall (1995). «Minimal Adjustment of Hydrographic Profiles to Achieve Static Stability». In: *J. Atmos. Oceanic Technol.* 12, pp. 381–389. DOI: 10.1175/1520-0426(1995)012<0381:MAOHPT>2.0.CO;2.

Jacobs, S.J. (1964). «The Taylor column problem». In: *Journal of Fluid Mechanics* 20.4, pp. 581–591.

Johns, B. et al. (1992). «On the wind-driven coastal upwelling in the Gulf of Lions». In: *Journal of Marine Systems* 3.4, pp. 309–320.

Jones, H. and J. Marshall (1993). «Convection with rotation in a neutral ocean: a study of open-ocean deep convection». In: *J. Phys. Oceanogr.* 23, pp. 1009–1039.

Kalnay, E. et al. (1996). «The NCEP/NCAR 40-Year Reanalysis Project». In: *Bull. Amer. Meteor. Soc.* 77, pp. 437–441. DOI: 10.1175/1520-0477(1996)077<0437:TNYRP>2.0.CO;2.

Kinder, T.H. and H.L. Bryden (1987). «The 1985-1986 Gibraltar Experiment: Data collection and preliminary results». In: *Eos Trans. AGU* 68.40, pp. 786–794. DOI: 10.1029/EO068i040p00786.

— (1990). «Aspiration of deep waters through straits». In: *The Physical Oceanography of Sea Straits*. Ed. by L.J. Pratt. Vol. 318. NATO ASI Series, pp. 295–319.

Klinger, B.A. and J. Marshall (1995). «Regimes and scaling laws for rotating deep convection in the ocean». In: *Dynamics of atmospheres and oceans* 21.4, pp. 227–256.

Kondo, J. (1975). «Air–sea bulk transfer coefficients in diabatic conditions». In: *Boundary-Layer Meteorol.* 9, pp. 91–112.

Korres, G., N. Pinardi, and A. Lascaratos (2000a). «The ocean response to low-frequency interannual atmospheric variability in the Mediterranean Sea. Part I: Sensitivity experiments and energy analysis». In: *Journal of Climate* 13.4, pp. 705–731. DOI: 10.1175/1520-0442(2000)013h0705:TORTLFi2.0.CO;2.

— (2000b). «The Ocean Response to Low-Frequency Interannual Atmospheric Variability in the Mediterranean Sea. Part II: Empirical Orthogonal Functions Analysis». In: *J. Climate, 13,* 13.4, pp. 732–745. DOI: 10.1175/1520-0442(2000)013<0732:TORTLF>2.0.CO;2.

Kostianoy, A.G. et al. (1998). «Variability of the Sicilian upwelling». In: *Oceanic fronts and related phenomena.* Konstantin Fedorov Memorial Symposium, Pushkin, Russia.

Kourafalou, V.H. and K. Barbopoulos (2003). «High resolution simulations on the North Aegean Sea seasonal circulation». In: *Annales Geophysicae* 21.1, pp. 251–265.

Krahmann, G. (1997). «Saisonale und zwischenjhrliche Variabiltim westlichen Mittelmeer - Analyse historicher Daten». Ph.D. Dissertation. Univ. Kiel, Kiel, Germany.

La Violette, P.E. (1990). «The Western Mediterranean Circulation Experiment (WMCE): Introduction». In: *J. Geophys. Res.* 95.C2, pp. 1511–1514. DOI: 10.1029/JC095iC02p01511.

LabSea Group (1998). «The Labrador Sea Deep Convection Experiment». In: *Bull. Amer. Meteor. Soc.* 79, pp. 2033–2058. DOI: 10.1175/1520-0477(1998)079<2033:TLSDCE>2.0.CO;2.

Lacombe, H., P. Tchernia, and L. Gamberoni (1985). «Variable bottom water in the western Mediterranean basin». In: *Progress in Oceanography* 14.

Large, W.G. and S.G. Yeager (2009). «The Global Climatology of an Interannual Varying Air-Sea Flux Data Set». In: *Climate Dynamics* 33, pp. 341–364. DOI: doi:10.1007/s00382-008-0441-3.

Larnicol, G., N. Ayoub, and P.Y. Le Traon (2002). «Major changes in Mediterranean Sea level variability from 7 years of TOPEX/Poseidon and ERS-1/2 data». In: *Journal of Marine Systems* 33, pp. 63–89.

Lascaratos, A., R.G. Williams, and E. Tragou (1993). «A mixed-layer study of the formation of Levantine intermediate water». In: *J. Geophys. Res.* 98.C8, pp. 14739–14749.

Leaman, F.A.S. and D. Kevin (1991). «Hydrographic structure of the convection regime in the gulf of lions: Winter 1987». In: *Journal of Physical Oceanography* 21, pp. 575–598.

Leaman, K.D. and F. Schott (1991). «Hydrographic structure of the convection regime in the Golfe du Lion». In: *J. Phys. Oceanogr.* 23, pp. 575–598.

Legg, S. and J.C. McWilliams (2001). «Convective Modifications of a Geostrophic Eddy Field». In: *J. Phys. Oceanogr.* 31, pp. 874–891. DOI: 10.1175/1520-0485(2001)031<0874:CMOAGE>2.0.CO;2.

Lentz, S.J. (1987). «A heat budget for the Northern California Shelf during CODE 2». In: *J. Geophys. Res.* 92.C13, pp. 14491–14509. DOI: 10.1029/JC092iC13p14491.

— (1992). «The Surface Boundary Layer in Coastal Upwelling Regions». In: *Journal of Physical Oceanography* 22, pp. 1517–1539.

Levitus, S. and T.P. Boyer (1994). *World Ocean Atlas 1994. Volume 4. Temperature*. National Environmental Satellite, Data, and Information Service, Washington DC, USA.

Levitus, S., R. Burgett, and T.P. Boyer (1994). *World Ocean Atlas 1994. Volume 3. Salinity*. National Environmental Satellite, Data, and Information Service, Washington DC, USA.

Levy, M., P. Klein, and A.M. Treguier (2001). «Impact of sub-mesoscale physics on production and subduction of phytoplankton in an oligotrophic regime». In: *Journal of Marine Research* 59, pp. 535–565.

List, R.J. (1958). *Smithsonian Meteorological Tables*. Smithsonian Institution, Washington DC, USA.

Lopez-Jurado, J.L., C. Gonzalez-Pola, and P. Velez-Belchi (2005). «Observation of an abrupt disruption of the long-term warming trend at the Balearic Sea, western Mediterranean Sea, in summer 2005». In: *Geophys. Res. Lett.* 32.L24606. DOI: 10.1029/2005GL024430.

Lumb, F.E. (1964). «The influence of cloud on hourly amount of total solar radiation at the sea surface». In: *Q. J. R. Meteorol. Soc.* 90, pp. 43–56.

Macdonald, A., J. Candela, and H.L. Bryden (1994). «Seasonal and Interannual Variability of the Western Mediterranean Sea». In: ed. by P.E. La Violette. American Geophysical Union, Washington DC, USA. Chap. An estimate of the net heat transport through the Strait of Gibraltar. DOI: 10.1029/CE046p0013.

Macdonald, A. and C. Wunsch (1996). «A global estimate of the ocean circulation and heat fluxes». In: *Nature* 382, pp. 436–439.

Madec, G. and the NEMO Team (2008). *NEMO ocean engine*. Vol. 27. Note du Pole de modelisation, Institut Pierre-Simon Laplace (IPSL), Paris, France.

Madec, G., P. Delecluse nad M. Imbard, and C. Levy (1998). *OPA8.1 Ocean general Circulation Model reference manual*. Note du Pole de modelisazion. Institut Pierre-Simon Laplace (IPSL), France.

Maillard, C. et al. (2007). «SeaDataNet: Development of a Pan-European Infrastructure for Ocean and Marine Data Management». In: *OCEANS 2007 - Europe*, pp. 1–6. DOI: 10.1109/OCEANSE.2007.4302435.

Manca, B.B. et al. (2006). «Ventilation of deep waters in the adriatic and ionian seas following changes in thermohaline circulation of the eastern mediterranean». In: *Climate Research* 31.2-3, pp. 239–256. URL: http://www.int-res.com/abstracts/cr/v31/n2-3/p239-256/.

Mariotti, A. et al. (2002). «The Hydrological Cycle in the Mediterranean Region and Implications for the Water Budget of the Mediterranean Sea». In: *J. Climate* 15, pp. 1674–1690. DOI: 10.1175/1520-0442(2002)015<1674:THCITM>2.0.CO;2.

Marshall, J. and F. Schott (1999). «Open-Ocean Convection: observations, theory and models». In: *Reviews of Geophysics* 37.1, pp. 1–64.

Marshall, J. et al. (1997). «Hydrostatic, quasi-hydrostatic, and nonhydrostatic ocean modeling». In: *J. Geophys. Res.* 102.C3, pp. 5733–5752. DOI: 10.1029/96JC02776.

Masina, S., N. Pinardi, and A. Navarra (2001). «A global ocean temperature and altimeter data assimilation system for studies of climate variability». In: *Climate Dynamics* 17.9, pp. 687–700.

Maxworthy, T. (1997). «Convection into domains with open boundaries». In: *Annual Review of Fluid Mechanics* 29.1, pp. 327–371.

MEDOC Group (1970). «Observation of formation of deep water in the Mediterranean Sea». In: *Nature* 227, pp. 1037–1040.

Mellor, G.L. and T. Ezer (1991). «A Gulf Stream model and an altimetry assimilation scheme». In: *J. Geophys. Res.* 96.C5, pp. 8779–8795. DOI: 10.1029/91JC00383.

Mey, P. De and M. Benkiran (2002). «Ocean Forecasting». In: ed. by N. Pinardi and J. Woods. Springer Berlin Heidelberg. Chap. A multivariate reduced-order optimal interpolation method and its application to the Mediterranean basin-scale circulation, pp. 281–305. DOI: 10.1007/978-3-662-22648-3_15.

Mikhaylov, B.A. and V.M. Zolotarev (1970). «Emissivity of liquid water». In: *Atmos. Oceanic. Phys.* 6, p. 52.

Millero, F.J. and A. Poisson (1981). «International one-atmosphere equation of state of seawater». In: *Deep Sea Research Part A. Oceanographic Research Papers* 28.6, pp. 625–629.

Millot, C. (1999). «Circulation in the Western Mediterranean Sea». In: *Journal of Marine Systems* 20, pp. 423–442.

Millot, C. and L. Wald (1981). «Coastal Upwelling». In: ed. by F.A. Richards. American Geophysical Union, Washington DC, USA. Chap. Upwelling in the Gulf of Lions. DOI: 10.1029/CO001p0160.

Molcard, A. et al. (2002). «Wind driven general circulation of the Mediterranean Sea simulated with a Spectral Element Ocean Model». In: *Dynamics of Atmospheres and Oceans* 35.2, pp. 97–130.

Mooers, C.N.K., C.A. Collins, and R.L. Smith (1976). «The Dynamic Structure of the Frontal Zone in the Coastal Upwelling Region off Oregon». In: *J. Phys. Oceanogr.* 6, pp. 3–21.

Niiler, P.P. (1975). «Deepening of wind-mixed layer». In: *Journal of Marine Research* 33.3, pp. 405–422.

Nittis, K. and A. Lascaratos (1998). «Diagnostic and prognostic numerical studies of LIW formation». In: *J. Mar. Syst.* 18, pp. 179–195.

Oddo, P. et al. (2009). «A nested Atlantic-Mediterranean Sea General Circulation Model for Operational Forecasting». In: *Ocean Science* 5, pp. 461–473.

Ooyama, K. (1969). «Numerical Simulation of the Life Cycle of Tropical Cyclones». In: *J. Atmos. Sci.* 26, pp. 3–40. URL: 10.1175/1520-0469(1969)026%3C0003:NSOTLC%3E2.0.CO;2.

Ovchinnikov, I.M. (1966). «Circulation in the surface and intermediate layers of the Mediterranean». In: *Oceanology* 6.1, pp. 48–58.

Ozsoy, E., A. Hecht, and U. Unluata (1989). «Circulation and hydrography of the Levantine Basin. Results of POEM coordinated experiments 1985–1986». In: *Progress in Oceanography* 22.2, pp. 125–170.

Pacanowski, R.C. and S.G.H. Philander (1981). «Parameterization of Vertical Mixing in Numerical Models of Tropical Oceans». In: *J. Phys. Oceanogr.* 11, pp. 1443–1451. DOI: 10.1175/1520-0485(1981)011<1443:POVMIN>2.0.CO;2.

Pacanowski, R.C., K. Dixon, and A. Rosati (1990). *README file for GFDL-MOM 1.0*. Geophysical Fluid Dynamics Laboratory. Princeton, NJ, USA. URL: http://www.gfdl.noaa.gov/mom-ocean-model.

Patara, L. et al. (2009). «Particle fluxes in the deep Eastern Mediterranean basins: the role of ocean vertical velocities». In: *Biogeosciences* 6, pp. 333–348. DOI: 10.5194/bg-6-333-2009.

Payne, R.E. (1971). «Albedo of the Sea Surface». PhD thesis. University of Rhode Island.

— (1972). «Albedo of the Sea Surface». In: *J. Atmos. Sci.* 29, pp. 959–970. DOI: 10.1175/1520-0469(1972)029<0959:AOTSS>2.0.CO;2.

Pedlosky, J. (1978). «A Nonlinear Model of the Onset of Upwelling». In: *J. Phys. Oceanogr.* 8, pp. 178–187. DOI: 10.1175/1520-0485(1978)008<0178:ANMOTO>2.0.CO;2.

— (1979). *Geophysical Fluid Dynamics*. Springer-Verlag, New York (NY), USA.

Peffley, M.B. and J.J. O'Brien (1976). «A Three-Dimensional Simulation of Coastal Upwelling off Oregon». In: *J. Phys. Oceanogr.* 6, pp. 164–180.

Peixoto, J. et al. (1982). «Atmospheric moisture transport and the water balance of the Mediterranean Sea». In: *Water Resour. Res.* 18, pp. 83–90.

Pettenuzzo, D., W.G. Large, and N. Pinardi (2010). «On the Corrections of ERA-40 Surface Flux Products consistent with the Mediterranean Heat and Water Budgets and the Connection between Basin Surface Total Heat Flux and NAO». In: *Journal of Geophysical Research* 115.C6. DOI: 10.1029/2009JC005631.

Philander, S.G.H. and R.C. Pacanowski (1981). «The oceanic response to cross-equatorial winds (with application to coastal upwelling in low latitudes)». In: *Tellus* 33, pp. 201–210. DOI: 10.1111/j.2153-3490.1981.tb01744.x.

Pinardi, N. and G. Coppini (2010). «Operational Oceanography in the Mediterranean Sea: the second stage of development». In: *Ocean Science* 6.263-267, pp. 263–267.

Pinardi, N., G. Coppini, and MFSTEP Partners (2006). «Mediterranean ocean Forecasting System: Toward Environmental Predictions-MFSTEP Executive Summary». Istituto Nazionale di Geofisica e Vulcanologia, Italy; European Commission. URL: http://hdl.handle.net/2122/2557.

Pinardi, N. and N. Flemming (1998). «The Mediterranean Forecasting System Science Plan». In: *EuroGOOS Publication No. 11*. Southampton Oceanography Center.

Pinardi, N. and E. Masetti (2000). «Variability of the Large Scale General Circulation of the Mediterranean Sea from observation and modeling: a re-

view». In: *Palaeogeography, Palaeoclimatology, Palaeoecology* 158, pp. 153–173.

Pinardi, N. and A. Navarra (1993). «Baroclinic Wind Adjustment in the Mediterranean Sea». In: *Deep Sea Research* 40.6, pp. 1299–1326.

Pinardi, N. et al. (1997). «Numerical simulation of the interannual variability of the Mediterranean Sea upper ocean circulation». In: *Geophys. Res. Lett.* 24, pp. 174–177.

Pinardi, N. et al. (2003). «The Mediterranean Ocean Forecasting System: first phase of implementation (1998-2001)». In: *Annales Geophysicae* 21.1, pp. 3–20.

Pinardi, N. et al. (2013). «Mediterranean Sea Large-Scale Low-Frequency Ocean Variability and Water Mass Formation Rates from 1987 to 2007: a retrospective analysis». In: *Progress in Oceanography*. DOI: 10.1016/j.pocean.2003.11.003.

POEM Group (1992). «General Circulation of the Eastern Mediterranean». In: *Earth Science Reviews* 32, pp. 285–309.

Pond, S. and G.L. Pickard (1983). *Introductory Dynamical Oceanography*. Gulf Professional Publishing.

Poulain, P.M., M. Menna, and E. Mauri (2012). «Surface Geostrophic Circulation of the Mediterranean Sea Derived from Drifter and Satellite Altimeter Data». In: *J. Phys. Oceanogr.* 42, pp. 973–990. DOI: 10.1175/JPO-D-11-0159.1.

Rahmstorf, S. (1991). «A zonal-averaged model of the ocean's response to climate change». In: *J. Geophys. Res.* 96.C4, pp. 6951–6963.

Raicich, F. (1996). «On the fresh balance of the Adriatic Sea». In: *Journal of Marine Systems* 9.3, pp. 305–319.

Reed, R.K. (1975). *An evaluation of formulas for estimating clear-sky insolation over the ocean*. Tech. rep. 26. NOAA Tech. Rep.

— (1976). *An evaluation of cloud factors for estimating insolation over the ocean*. Tech. rep. 8. NOAA Tech. Memo.

— (1977). «On estimating insolation over the ocean». In: *J. Phys. Oceanogr.* 17, pp. 854–871.

Richman, J.G. and A. Badan-Dangon (1983). «Mean heat and momentum budgets during upwelling for the coastal waters off northwest Africa». In: *J. Geophys. Res.* 88.C4, pp. 2626–2632. DOI: 10.1029/JC088iC04p02626.

Riehl, H. (1954). *Tropical meterology*. McGraw-Hill, New York (NY), USA.

Robinson, A.R. et al. (1991). «The eastern Mediterranean general circulation: features, structure and variability». In: *Dynamics of Atmospheres and Oceans* 15.3, pp. 215–240. DOI: 10.1016/0377-0265(91)90021-7.

Roether, W. and R. Schlitzer (1991). «Eastern Mediterranean Deep Water renewal on the basis of ChloroFluoroMethane and Tritium data». In: *Dyn. Atmos. Ocean* 15.3-5, pp. 333–354.

Roether, W. et al. (1996). «Recent changes in eastern mediterranean deep waters». In: *Science* 271.5247, pp. 333–335. DOI: 10.1126/science.271.5247.333.

Roll, H.U. (1965). *Physics of the Marine Atmosphere*. Vol. 7. International Geophysics Sciences. Academic Press, New York (NY), USA.

Rosati, A. and K. Miyakoda (1988). «A General Circulation Model for Upper Ocean Simulation». In: *J. Phys. Oceanogr.* 18, pp. 1601–1626. DOI: 10.1175/1520-0485(1988)018<1601:AGCMFU>2.0.CO;2.

Roussenov, V. et al. (1995). «A seasonal model of the Mediterranean Sea general circulation». In: *J. Geophys. Res.* 100.C7, pp. 13515–13538. DOI: 10.1029/95JC00233.

Rudnick, D.L. and R.E. Davis (1988). «Mass and heat budgets on the northern California continental shelf». In: *J. Geophys. Res.* 93.C11, pp. 14013–14024. DOI: 10.1029/JC093iC11p14013.

Rykaczewski, R.R. and D.M. Checkley (2008). «Influence of ocean winds on the pelagic ecosystem in upwelling regions». In: *Proceedings of the National Academy of Sciences* 105.6, pp. 1965–1970.

Savvidis, Y. et al. (2004). «Modeling of the upwelling hydrodynamics in the Aegean Sea». In: *Mediterranean Marine Science*. URL: http://www.medit-mar-sc.net/index.php/marine/article/view/205.

Schiano, M.E. et al. (1993). «Air–sea interaction measurements in the west Mediterranean Sea during the Tyrrhenian Eddy Multi-Platform Observation Experiment». In: *J. Geophys. Res.* 98, pp. 2461–2474.

Schlitzer, R. et al. (1991). «Chlorofluoromethane and oxygen in the Eastern Mediterranean». In: *Deep Sea Research Part A. Oceanographic Research Papers* 38.12, pp. 1531–1551.

Schott, F. and K.D. Leaman (1991). «Observations with moored acoustic Doppler current profilers in the convection regime in the Gulf of Lion». In: *J. Phys. Oceanogr.* 21, pp. 558–574.

Schott, F., M. Visbeck, and U. Send (1994). «Ocean Processes on Climate Dynamics». In: ed. by P. Malanotte-Rizzoli and A. Robinson. Kluwer, Nor-

well (MA), USA. Chap. Open-ocean deep convection, Mediterranean and Greenland Sea, pp. 203–225.

Schott, F. et al. (1996). «Observations of deep convection in the Gulf of Lions, Northern Mediterranean, during the winter of 1991/92». In: *Journal of Physical Oceanography* 26.4, pp. 505–524. DOI: 10.1175/1520-0485(1996)026<0505:OODCIT>2.0.CO;2.

Schroder, K. et al. (2006). «Deep and intermediate water in the western Mediterranean under the influence of the Eastern Mediterranean Transient». In: *Geophys. Res. Lett.* 33.L21607. DOI: 10.1029/2006GL027121.

Seckel, G.R. and F.H. Beaudry (1973). «The radiation from Sun and sky over the North Pacific Ocean (abstract)». In: *Trans. Amer. Geophys. Union* 54, p. 1114.

Send, U. and J. Marshall (1995). «Integral Effects of Deep Convection». In: *J. Phys. Oceanogr.* 25, pp. 855–872. DOI: 10.1175/1520-0485(1995)025<0855:IEODC>2.0.CO;2.

Smith, R.L. (1968). «Upwelling». In: *Oceanography Marine Biological Annual Review* 6, pp. 11–47.

— (1981). «Coastal Upwelling». In: ed. by F.A. Richards. American Geophysical Union, Washington DC, USA. Chap. A Comparison of the Structure and Variability of the Flow Field in three Coastal Upwelling Regions: Oregon, Northwest Africa, and Peru. DOI: 10.1029/CO001p0107.

Smith, R.O., H.L. Bryden, and K. Stansfield (2008). «Observations of New Western Mediterranean Deep Water Formation using Argo Floats 2004-2006». In: *Ocean Science* 4, pp. 133–149.

Smith, S.D. et al. (1996). «Air-sea fluxes: 25 years of progress». In: *Boundary-Layer Meteorology* 78.3-4, pp. 247–290.

Sparnocchia, S. et al. (1995). «Intermediate Water formation in the Ligurian Sea». In: *Oceanol. Acta* 18.2, pp. 151–162.

Speich, S., G. Madec, and M. Crépon (1996). «A strait outflow circulation process study: the case of the Alboran Sea». In: *Journal of physical oceanography* 26.3, pp. 320–340.

Stergiou, K.I. et al. (1997). «The Hellenic seas: physics, chemistry, biology and fisheries». In: *Oceanogr. Mar. Biol. Annu. Rev.* 35, pp. 415–538.

Sverdrup, H.U. (1938). «On the process of upwelling». In: *Journal of Marine Research* 1.2, pp. 155–164.

Swallow, J.C. and G.F. Caston (1973). «The preconditioning phase of MEDOC 1969, I, Observation». In: *Deep Sea Res.* 20, pp. 429–448.

Taylor, P.K. and WGASF Members (2000). «Intercomparison and Validation of Ocean-Atmosphere Energy Flux fields». In: *Final Report of the Joint WCRP/SCOR Working group on Air-Sea Fluxes*. Ed. by P.K. Taylor. WCRP-112, WMO/TD-No.1036. URL: http://www.soc.soton.ac.uk/JRD/MET/WGASF/.

Tonani, M. et al. (2008). «A High Resolution Free-Surface Model of the Mediterranean Sea». In: *Ocean Science* 4.1, pp. 1–14.

Turner, J.S. (1979). *Buoyancy effects in fluids*. Cambridge University Press.

Tziperman, E. and P. Malanotte-Rizzoli (1991). «The climatological seasonal circulation of the Mediterranean Sea». In: *Journal of Marine Research* 49.3, pp. 411–434.

Tziperman, E. and K. Speer (1994). «A study of water mass transformation in the Mediterranean Sea: analysis of climatological data and a simple three-box model». In: *Dyn. Atmos. Oceans* 21, pp. 53–82.

Unsworth, M. H. and J. L. Monteith (1972). «Aerosol and solar radiation in Britain». In: *Q.J.R. Meteorol. Soc.* 98, pp. 778–797. DOI: 10.1002/qj.49709841806.

Uppala, S. M. et al. (2005). «The ERA-40 Re-Analysis». In: *Q. J. R. Meteor. Soc.* 131, pp. 2961–3012. DOI: 10.1256/qj.04.176.

Vallis, G.K. (2006). *Atmospheric and oceanic fluid dynamics*. Cambridge University Press.

Voorhis, A.D. and D.C. Webb (1970). «Large vertical currents observed in a winter sinking region of the nortwestern Mediterranean». In: *Cah. Oceanogr.* 22, pp. 571–580.

Weare, B.C. (1989). «Uncertainties in estimates of surface heat fluxes derived from marine reports over the tropical and subtropical oceans». In: *Tellus* 41A, pp. 357–370. DOI: 10.1111/j.1600-0870.1989.tb00388.x.

Whitehead, J.A., J. Marshall, and G.E. Hufford (1996). «Localized convection in rotating stratified fluid». In: *J. Geophys. Res.* 101(C11),C11, pp. 25705–25721. DOI: 10.1029/96JC02322.

Williams, R.G. (1988). «Modification of ocean eddies by air-sea interaction». In: *J. Geophys. Res.* 93.C12, pp. 15523–15533. DOI: 10.1029/JC093iC12p15523.

Winant, C.D., R.C. Beardsley, and R.E. Davis (1987). «Moored wind, temperature, and current observations made during Coastal Ocean Dynamics Experiments 1 and 2 over the Northern California Continental Shelf and upper slope». In: *J. Geophys. Res.* 92.C2, pp. 1569–1604. DOI: 10.1029/JC092iC02p01569.

Wooster, W.S. and J.L. Reid (1963). «The Sea». In: ed. by M.N. Hill. Vol. 2. Inter Science, New York (NY), USA. Chap. Eastern boundary currents, pp. 253–280.

Wust, G. (1961). «On the Vertical Circulation of the Mediterranean Sea». In: *Journal of Geophysical Research* 66.10, pp. 3261–3271.

Wyrtki, K. (1981). «An Estimate of Equatorial Upwelling in the Pacific». In: *J. Phys. Oceanogr.* 11, pp. 1205–1214. DOI: 10.1175/1520-0485(1981)011<1205:AEOEUI>2.0.CO;2.

Xie, P. and P.A. Arkin (1997). «Global Precipitation: A 17-Year Monthly Analysis Based on Gauge Observations, Satellite Estimates, and Numerical Model Outputs». In: *Bull. Amer. Meteor. Soc.* 78, pp. 2539–2558. DOI: 10.1175/1520-0477(1997)078<2539:GPAYMA>2.0.CO;2.

Yoshida, K. (1967). «Circulation in the eastern tropical oceans with special reference to upwelling and undercurrents». In: *Japan. J. Geophys.* 4, pp. 1–75.